

中国科学技术大学

University of Science and Technology of China

# 博士学位论文



论文题目	Surface Modifications for Optical Applications Based on Natural and Synthetic Polymers to Enhance Antifogging and Antimicrobial Properties
作者姓名	Basheer Mansoor Awad Basheer
学科专业	Material Science and Engineering
导师姓名	Prof. Liangbin Li
完成时间	April 2022

University of Science and Technology of China

A dissertation for a doctor's degree



**Surface Modifications for Optical Applications Based on  
Natural and Synthetic Polymers to Enhance Antifogging  
and Antimicrobial Properties**

Author's Name: Basheer Mansoor Awad Basheer  
Specialty: Material Processing Engineering  
Supervisor: Prof. Liangbin Li

## 中国科学技术大学学位论文原创性声明

本人声明所呈交的学位论文,是本人在导师指导下进行研究工作所取得的成果。除已特别加以标注和致谢的地方外,论文中不包含任何他人已经发表或撰写过的研究成果。与我一同工作的同志对本研究所做的贡献均已在论文中作了明确的说明。

作者签名: Basheer

签字日期: 28/3/2022

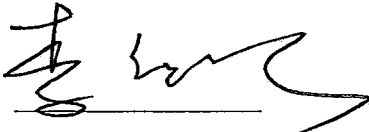
## 中国科学技术大学学位论文授权使用声明

作为申请学位的条件之一,学位论文著作权拥有者授权中国科学技术大学拥有学位论文的部分使用权,即:学校有权按有关规定向国家有关部门或机构送交论文的复印件和电子版,允许论文被查阅和借阅,可以将学位论文编入《中国学位论文全文数据库》等有关数据库进行检索,可以采用影印、缩印或扫描等复制手段保存、汇编学位论文。本人提交的电子文档的内容和纸质论文的内容相一致。

保密的学位论文在解密后也遵守此规定。

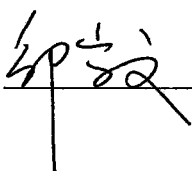
公开 保密 (\_\_\_\_年)


作者签名: Basheer

导师签名: 

签字日期: 28/3/2022

签字日期: 2022.3.28

评审专家签名: 

评审专家签名: 

## ABSTRACT

---

### ABSTRACT

Fogging is always a significant problem for agricultural films, where fog may reduce the light transmission resulting in an adverse effect on the yield and quality of crops. Many reports have been disclosed in the field of antifogging on the surfaces of plastic films. Nevertheless, these methods have drawbacks, such as the cumbersome preparation process, high-cost experimental components, and toxic reagents. In the present work, a simple and effective technique is adopted to develop a low-cost super-hydrophilic layer based on PVA for coating LDPE films with excellent fogging resistance properties and extraordinary light transmittance. Corona discharge treatment is applied to play a pivotal role in the stability of the coating layer by creating a fertile environment for solid chemical bonding on the surface of the LDPE film. By adding TBS buffer solution with surfactants, the overall hydrophilicity performance of the film becomes enhanced.

Further, adding silica nanoparticles in different concentrations to the mixture solution increases the wetting and coating stability. The time-domain NMR is employed to clarify the influence of surface free energy on the formation of silica aggregations. The results show that the increase in the bound water fraction promotes the formation of homogeneously distributed silica aggregates into particles dispersed on the surface. The described technique results in the homogeneous deposition of the antifogging coating layer on the surface of LDPE film, which becomes super-hydrophilic. Our findings indicate the film modified by an antifogging coating containing silica nanoparticles can stand fog-free for more than one month under the hot fog test according to the SEM images, ATR-FTIR chemical bonding, and contact angle after one month in the hot dripping test. Through this work, adding buffer solutions to non-ionic fillers and further filling them into the polymer matrix will open a new strategy for anti-fogging films relevant to greenhouse technology in agriculture.

The second work studied the coffee ring effect (CRE) phenomenon due to the inhomogeneous coating. When a colloidal droplet with hanging particles evaporates on a flat substrate, a ring-shaped structure develops around the droplet's edge. This phenomenon may be noticed in everyday life when liquid droplets containing suspended particles evaporate, such as ring stains left behind by spilled coffee drips. However, it is unsuitable for applications that need homogeneous particle deposition on surfaces, such as agricultural films and optical applications. In the present work, a simple and effective technique using solid-state low field NMR is adopted to demonstrate slowing down the evaporation rate induces the Marangoni flow and aids in decreasing CRE generation from evaporated colloidal droplets, even in the absence of the additives (surfactant or polymer). In addition, the  $T_2$  Carr-Purcell-Meiboom-Gill sequence (CPMG) approach was used to monitor nano-fluid droplets with different evaporation speeds and a variety of additive concentrations on the hydrophobic low-density polyethylene (LDPE) surface to explain the formation of the CRE and uniform distribution of silica



## ABSTRACT

---

nanoparticles on changes in water fractions during evaporation. Our findings revealed that reducing the evaporation rate with the presence of surfactant and polymer by regulating water fractions in colloidal solutions has a significant impact on the silica nanoparticles uniform distribution and prevention of CRE formation during the coating process, which is critical in the industrial sector and linked scientific research.

The third work focuses on coating glasses for super-hydrophilic and robust layers. Antifogging/antimicrobial dual-functional coatings can be applied to transparent substrates. However, few studies on such dual-functional layers have been published thus far. This study used a straightforward one-pot method to create an antifogging and antimicrobial composite coatings layer of chitosan/silica (Ch/SiO<sub>2</sub>). Using solid-state low field nuclear magnetic resonance (LF-NMR), the effect of introducing modified silica nanoparticles (*MSN*) to chitosan structure was investigated. Two states (solution-state and solid-state) were utilized to evaluate the antifogging/antimicrobial properties of the coating layers based on the mobility of the significant water fractions using the  $T_2$  Carr-Purcell-Meiboom-Gill (CPMG) sequence methodology. The hydrogen bonds and electrostatic attractions created by *MSN* (water molecules/hydronium ions) in the solution state result in a higher bound water ratio in the final layers after drying, improving the antifogging and antimicrobial properties with good mechanical performance. Therefore, based on the chitosan/silica layer, 95% is the minimum proportion of bound water necessary in the final layer structure compared to the other water fractions to restrict microbial activity and minimize the fogging concerns. The information gathered can be a quick, non-destructive, and non-invasive preliminary indication of antifogging/antimicrobial coating quality.

**Keywords:** agriculture film; greenhouses, coffee-ring effect (CRE),  $T_2$  Carr-Purcell-Meiboom-Gill sequence (CPMG), low-density polyethylene (LDPE).

**Abbreviations and Symbols**

<b>Symbol</b>	<b>Meaning</b>
PVA	Polyvinyl alcohol
LDPE	Low-density polyethylene
LLDPE	Linear low-density polyethylene
TBS	Tris-buffered saline
LF-NMR	Low field nuclear magnetic resonance
SEM	Scanning electron microscope
ATR-FTIR	Attenuated total reflection Fourier transform infrared
CRE	Coffee-ring effect
$T_2$	Spin-spin relaxation time
CPMG	Carr-Purcell-Meiboom-Gill sequence
SiO <sub>2</sub>	Silica nanoparticles
MSN	Modified silica nanoparticles
PETE	Polyethylene terephthalate
ILT	Inverse laplace transform
PVC	Polyvinyl chloride
PS	Polystyrene or Styrofoam
PP	Polypropylene
PE	Polyethylene
ICI	Imperial chemical industries
IR	Infrared radiation

### Abbreviations and Symbols

EVA	Ethylene-vinyl acetate
EBA	Ethylene butyl acrylate
EN	The European standard
$\gamma_{pW}$	The surface energy of the polymer-water interface
$\gamma_{pA}$	Surface energy at the polymer-air interface
$\gamma_{wA}$	Surface energy at the water-air interface
$\theta$	The contact angle at the equilibrium
SMS	Sorbitan monoacyl esters
STS	Sorbitan to fatty acids
SITES	Sorbitan triacyl esters
Al <sub>2</sub> O <sub>3</sub>	Aluminum oxide
Ch	Chitosan
pH	Potential of hydrogen
LbL	Layer by layer
TUR	Take-up ratio
BUR	Blow-up ratio
X-100	Octyl phenol ethylene oxide
T-20	Polyoxymethylene sorbitol ester
SDS	Sodium dodecyl sulfate
$\mu m$	Micrometer
W	Watt
OM	Optical microscopy
nm	Nanometer

### Abbreviations and Symbols

Wt%	Weight percentage
$J$	Evaporation rate
TB	Time spent on bound water during evaporation
$t_F$	The time scale of totally droplet evaporation
CR	The time scale for particles near the contact line (CL) to collide
CL	Contact line
SANS	Small-angle neutron scattering
CAH	Contact angle hysteresis
$v_t$	Take-up velocity
$v_e$	Extrusion velocity
S	The ratio of the area covered by silica after evaporation
$S_0$	The ratio of the area covered by silica before evaporation
$L_p$	Restricted distance
$\theta_{initial}$	The first stage of evaporation
$\theta_{receding}$	Receding contact angle,
$\theta_{final}$	Final contact angle
$\tau_{evap}$	The time scale for liquid droplet evaporation.
$\tau_{particle}$	Particle denotes the time scale for particles near the CL to collide.
$t_P$	The time for particle motion.
$t_{EI}$	Evaporation time of the residual droplet volume.
$t_{jL}$	The complete evaporation duration of a droplet when subjected to a laser.
EBA	Ethylene butyl acrylate
CuO	copper(II) oxide

Table of Contents

**Table of Contents**

ABSTRACT..... i

Abbreviations and Symbols..... iii

Table of Contents..... vi

List of Figures..... x

List of Table..... xiv

Chapter1 General Introduction ..... 15

    1.1 Background..... 15

    1.2 Low-density polyethylene (LDPE)..... 16

        1.2.1 LDPE uses in agriculture ..... 17

        1.2.2 Key properties of greenhouse covers ..... 18

            1.2.2.1 Film inherent parameters..... 19

            1.2.2.2 Environmental parameters ..... 19

    1.3 An overview of fogging problems ..... 20

        1.3.1 Fog formation principle on polyethylene films..... 20

        1.3.2 Anti-fog agents' mechanism..... 21

        1.3.3 Antifogging film preparation in the current industrial field..... 23

        1.3.4 Antifogging performance evaluation ..... 23

            1.3.4.1 Hot fog test..... 24

            1.3.4.2 Cold fog test..... 24

    1.4 Corona discharge ..... 25

        1.4.1 Type of corona discharge ..... 25

    1.5 Coatings ..... 26

        1.5.1 Coating processes..... 27

        1.5.2 Physical coating processes ..... 27

        1.5.3 Coating materials ..... 27

            1.5.3.1 Silica nanoparticles. .... 27

            1.5.3.2 Surfactant ..... 27

            1.5.3.3 Polymer coatings..... 28

Chapter2 Experiments and Methodology ..... 30

## Table of Contents

2.1 Materials .....	31
2.2 Processing of LDPE film and antifogging layer .....	31
2.2.1 Preparation of LDPE Film .....	31
2.2.2 Preparation of PVA anti-fog solutions .....	32
2.2.3 Anti-fogging coating processes .....	32
2.3 Surface modification of silica nanoparticles .....	34
2.4 Controlling the evaporation rate .....	35
2.5 Nanoparticles deposits formation .....	35
2.6 Preparation of the hybrid chitosan coating film .....	36
2.7 Characterization .....	37
2.7.1 Contact angle measurement .....	37
2.7.2 Optical microscopy .....	38
2.7.3 Optical properties .....	38
2.7.4 Antifogging test .....	38
2.7.5 Scanning electron microscope (SEM) measurements .....	39
2.7.6 Fourier transform infrared .....	40
2.7.7 Solid-state low-field <sup>1</sup> H NMR spectroscopy .....	40
2.7.8 Coatings mechanical properties .....	41
2.7.9 Antimicrobial test (Disk diffusion assay Antibacterial) .....	42
Chapter 3 Polyvinyl Alcohol (PVA) Based Super-Hydrophilic Anti-Fogging Layer Assisted by Plasma Spraying for Low-Density Polyethylene (LDPE) Greenhouse Films .....	59
3.1. Introduction .....	59
3.2 Results and discussion .....	61
3.2.1 Surface wettability .....	61
3.2.2 Chemical composition .....	62
3.2.3 Surface morphology .....	66
3.2.4 Anti-fogging agent .....	68
3.2.4.1 Accelerated dripping test .....	68
3.2.4.1.1 First and ten drops time .....	68
3.2.4.1.2 Shelf-life test .....	69



## Table of Contents

3.2.5 Coatings mechanical properties .....	72
3.3 Conclusion .....	72
Chapter 4 Nanoparticle Deposition Pattern During Colloidal Droplet Evaporation as <i>in-situ</i> Investigated by Low-Field NMR: The Critical Role of Bound Water .....	43
4.1 Introduction .....	43
4.2 Results and discussions .....	45
4.2.1 Surface modification of silica nanoparticles .....	45
4.2.2 Influence of evaporation rate on CRE .....	46
4.2.3 Surface morphology .....	47
4.2.4 Wettability .....	50
4.2.5 Evolution of three-state water .....	52
4.2.5.1 Solution state .....	52
4.2.5.2 <i>In-situ</i> NMR tracking .....	53
4.3 Conclusion .....	58
Chapter 5 Dual-Functional Antifogging/Antimicrobial Based Natural Polymer Coating for Glass Applications as Investigated by Low Field NMR .....	74
5.1 Introduction .....	74
5.2 Results and discussions .....	76
5.2.1 Chemical composition .....	76
5.2.2 Surface wettability .....	77
5.2.3 Transmittance and haze .....	78
5.2.4 Surface morphology .....	79
5.2.5 Antimicrobial activity .....	80
5.2.6 Antifogging properties .....	81
5.2.6.1 Cold-warm fogging test .....	81
5.2.6.2 Hot-vapor fogging test .....	82
5.2.7 Mechanical properties .....	82
5.2.8 NMR investigations .....	83
5.3 Conclusion .....	86
Chapter 6 Summary and Outlook .....	88

## Table of Contents

---

Acknowledgements.....	92
List of Publications .....	93
References.....	94

## List of Figures

<b>Fig 1. 1.</b> The increasing volume of global plastic manufacturing [5].....	16
<b>Fig 1. 2.</b> Plastic production by region 2019 [10].....	17
<b>Fig 1. 3.</b> PE Structure types (a) HDPE, (b) LLDPE, (c) LDPE [10].....	17
<b>Fig. 1. 4.</b> Application of the LDPE in daily life [14,15].....	18
<b>Fig. 1. 5.</b> Agricultural surface covered with plastic film (greenhouses and walk-in high tunnels) [16].	19
<b>Fig. 1. 6.</b> As-installed greenhouse coverings (a) after two years of use (b).	20
<b>Fig. 1. 7.</b> Parameters of Young's equation for a water droplet on a plastic film.	21
<b>Fig. 1. 8.</b> Chemical structures of classes of antifogging.	22
<b>Fig. 1. 9.</b> The diagram clarifies producing LDPE film followed by the plasma treatment and coating process applied in industries.	23
<b>Fig. 1. 10.</b> Testing films for fog properties: (a) hot fog test and (b) cold fog test schemat	25
<b>Fig. 1. 11.</b> A diagram showing the many types of corona discharges.	26
<b>Fig. 1. 12.</b> Surfactant categorization based on head composition: 1. nonionic, 2. anionic, 3. cationic, and 4. amphoteric.....	28
<b>Fig. 1. 13.</b> The overall research idea.....	30
<b>Fig. 2. 1.</b> (a) Contact angle test for difference methods, (b) Transmittance and haze.	33
<b>Fig. 2. 2.</b> Schematic illustration of coating of anti-fogging layer on the LDPE substrate.....	33
<b>Fig. 2. 3.</b> Schematic illustration (1) clarifies the steps of preparing hybrid chitosan coating solutions, (2) shows the steps for the dip-coating method for a glass substrate, (a) plasma treatment, (b) dip coating, (c) drying, (d) the final product.	36
<b>Fig 2. 4.</b> Synthesis of Ch/SiO <sub>2</sub> hybrid film coating.	37
<b>Fig. 2. 5.</b> Optical microscope images for spreading silica on the LDPE surface according to the different plasma power. (a) untreated, (b) 300W, (c) 500W, (d) 700W, (e) 900W.	38
<b>Fig. 2. 6.</b> The diagram shows a one-month shelf-life antifogging test for five modified films.....	39
<b>Fig. 2. 7.</b> CPMG obtained the fitting process for $T_2$ . (a) CPMG echo trains together with triple exponential decay function, (b) relaxation time distribution derived after Inverse Laplace Transform (ILT), and (c) proportion of water fractions during evaporation.	40
<b>Fig. 2. 8.</b> a) The principle of sandpaper test, applied for unmodified and modified glass 10 cycles for each sample, b) optical microscopy pictures after the mechanical test.....	42

## List of Figures

<b>Fig. 3. 1.</b> Schematic illustration of surface modification of silica nanoparticles.....	45
<b>Fig. 3. 2.</b> Weight loss according to evaporation rate $J$ , (a) NMR experiment setup, (c) weight loss of solutions droplet for the system without caps at the ambient environment in the $J = 4.3 \sim 7.6 \times 10^{-2}$ mg/min, (b) system with a cap hole size of 1mm, $J = 5.5 \sim 7.1 \times 10^{-3}$ mg/min, (d) system with a cap hole size of 0.5mm, $J = 2.7 \sim 3.1 \times 10^{-4}$ mg/min, All the above experiments were conducted at the same temperature (23 °C) and humidity (75 %).	46
<b>Fig. 3. 3.</b> Optical microscopy images clarify suppression of the CRE. (a) Evaporation rate $J = 4.3 \sim 7.6 \times 10^{-2}$ mg/min, (b) $J = 5.5 \sim 7.1 \times 10^{-3}$ mg/min, (c) $J = 2.7 \sim 3.1 \times 10^{-4}$ mg/min. (a1, a2, a3, a4), (b1, b2, b3, b4), (c1, c2, c3, c4) the distribution of silica nanoparticles on hydrophobic LDPE surface in different surfactant concentration (0%, 0.1%, 0.5%, 1%) with different $J$ (a, b, c) respectively. (a5, b5, c5) the addition of (0.25%) PVA polymer to (Si+Su3) sample in different $J$ (a, b, c) respectively. ....	48
<b>Fig. 3. 4.</b> Effect of evaporation rate $J$ on final silica distribution on LDPE surface in the presence of surfactant and polymer. ....	49
<b>Fig. 3. 5.</b> (a) ring size, (b) existence of a limited distance $L_p$ , between the original pinning point and the coffee-ring border.....	50
<b>Fig. 3. 6.</b> Contact angle for varying evaporation rate $J$ as a function of surfactant concentration and polymer in (a) ambient environment in the $J = 4.3 \sim 7.6 \times 10^{-2}$ mg/min. (b) open system-1mm, $J = 5.5 \sim 7.1 \times 10^{-3}$ mg/min, (c) open system-0.5mm, $J = 2.7 \sim 3.1 \times 10^{-4}$ mg/min. Sketches of particle migration (left) and contact angle images (right) during sessile pure silica drop drying at (d) open system-ambient environment, (e) open system-1mm, (f) open system-0.5mm. All contact angle pictures taken at 1 mm scale. ....	51
<b>Fig. 3. 7.</b> Relaxation time distributions in the presence of other additions. (a) $T_2$ CPMG after ILT where three different distinct $T_2$ are observed, together with enlarged pictures for (b) free water, (c) bound water, and (d) trapped water, respectively. (e) the proportion of different water fractions under various additions.....	52
<b>Fig. 3. 8.</b> The relaxation time distribution of different water fractions over time in the presence of surfactant and polymer concentrations. (a) & (b) $T_2$ CPMG for pure silica and (Si+Su3+PVA) solution droplet respectively, at the same evaporation speed $5.5 \sim 7.1 \times 10^{-3}$ mg/min. (a1, b1) $T_2$ CPMG original signals for amplitude droplets decreasing with time, (a2, b2) ILT and, (a3, b3) proportion of water fractions during evaporation for pure silica droplet and (Si+Su3+PVA) solution droplets respectively.....	54
<b>Fig. 3. 9.</b> Relaxation time distributions investigated the changes in water fractions over time in the presence of surfactant and polymer concentrations. (a) & (b) $T_2$ CPMG for pure silica and (Si+Su3+PVA) solution droplet respectively at the same $J = 2.7 \sim 3.1 \times 10^{-4}$ mg/min. (a1, b1) $T_2$ CPMG original signals for decreasing droplets	

## List of Figures

with time, (a2, b2) the corresponding $T_2$ distribution after ILT and (a3, b3) proportion of water fractions during evaporation for pure silica droplet and (Si+Su3+PVA) solution droplets, respectively. ....	55
<b>Fig. 3. 10.</b> The time spent on bound water fraction during the colloidal droplets' evaporation is normalized by the time of all fractions for fully evaporation $t_B/t_F$ as a function of the area covered by silica distribution $S/S_0$ . ....	56
<b>Fig. 4. 1.</b> (a) Contact angle of LDPE film after treatment by plasma with different powers. (b) the dynamics of water contact angle for LDPE film modified by plasma at a speed of 15 mm/s selected from (a). (c) shelf-life results of surface tension with storage. ....	61
<b>Fig. 4. 2.</b> SEM test for samples after corona treatment (a) Untreated, (b) 300W, (c) 500W, (d) 700W, (e) 900W. ....	62
<b>Fig. 4. 3.</b> FT-IR spectra of LDPE films with an anti-fogging agent (a) before one month and (b) after one month. ....	63
<b>Fig. 4. 4.</b> (a) Schematic illustration of the NMR experiment for tracking the evaporation process in-situ. (b) different kinds of water on the surfaces of modified LDPE with different surface wettability. (c, d, and e) the evolution of different kinds of water as reflected by the $T_2$ relaxometry after inverse Laplace transform. ....	64
<b>Fig. 4. 5.</b> (a) The contact angle of different anti-fogging layers was measured together with (b) transmittance and haze, and (c) the contact angle was measured after one month. ....	65
<b>Fig. 4. 6.</b> Optical microscopy images on the left side (a, b, c, d, e) and SEM on the right side (a*, b*, c*, d*, e*) for the anti-fogging films (a, a*) untreated LDPE (b, b*) L-(P/X), (c, c*) L-(P/X/T), (d, d*) L-(P/X/T/Si1), and (e, e*) L-(P/X/T/Si3). ....	67
<b>Fig. 4. 7.</b> Optical microscopy images (e, f, g, and h) and SEM images (e*, f*, g* and h*) for the anti-fogging films after one month (e, e*) L-(P/X), (f, f*) L-(P/X/T), (g, g*) L-(P/X/T/Si1), and (h, h*) L-(P/X/T/Si3). ....	68
<b>Fig. 4. 8.</b> (a) Diagram shows the method for detecting the time for the formation of the first and ten drops, (b) experimental results of different anti-fogging layers. ....	69
<b>Fig. 4. 9.</b> Original samples images before hot fog rest (a1) untreated, (a2) plasma treatment (900W), and (a3) coated by pure PVA. Hot fogging test images on LDPE film surface in less than 5 seconds (b1) untreated, (b2) plasma treatment (900W), (b3) coated by pure PVA. Long-time fogging test for different antifogging films after (c) 30 minutes, (d) 7 days, and (e) 30 days. ....	70
<b>Fig. 4. 10.</b> SEM images of modified LDPE cross-sections. (a) L-(P/X) before one month, (b) L-(P/X) 13 days, (d) L-(P/X/T/Si3) before one month, (c) L-(P/X/T/Si3) after one month. ....	71
<b>Fig. 4. 11.</b> Optical microscope images after sandpaper abrasion test a) unmodified, (b) L-(P/X), (c) L-(P/X/T), (d) L-(P/X/T/Si1), (e) L-(P/X/T/Si3). ....	72

## List of Figures

<b>Fig. 5. 1.</b> FT-IR spectra of composite chitosan coating layers a) <i>Ch</i> , b) <i>Ch/SiO<sub>2</sub></i> (1), c) <i>Ch/SiO<sub>2</sub></i> (2), d) <i>Ch/SiO<sub>2</sub></i> (3).....	76
<b>Fig. 5. 2.</b> The contact angle ( $\theta$ ) for different antifogging coatings layers is based on silica concentration. ....	77
<b>Fig. 5. 3.</b> Transmittance and haze after-coated glass, -cold-warm test, and -hot-vapor test. ....	78
<b>Fig. 5. 4.</b> Scanning electron microscopy of composite chitosan coating layers, a) <i>Ch</i> , b) <i>Ch/SiO<sub>2</sub></i> (1), c) <i>Ch/SiO<sub>2</sub></i> (2), d) <i>Ch/SiO<sub>2</sub></i> (3). (a1, b1, c1, d1) zoom in.....	79
<b>Fig. 5. 5.</b> SEM cross-section for antifogging coating layer, e) chitosan film, f) <i>Ch/SiO<sub>2</sub></i> (3). <i>Ch/SiO<sub>2</sub></i> (3) film. .	80
<b>Fig. 5. 6.</b> Antimicrobial adhesion tests using <i>E. coli</i> . Colonial morphologies are revealed by images corresponding to (a) uncoated glass, b) <i>Ch</i> , c) <i>Ch/SiO<sub>2</sub></i> (1), d) <i>Ch/SiO<sub>2</sub></i> (2), e) <i>Ch/SiO<sub>2</sub></i> (3).....	81
<b>Fig. 5. 7.</b> Optical microscopy and photograph pictures of composite chitosan coating layers (a, b, c, d, e) after coating (f, g, h, I, j) after the antifogging cold test. The photographic pictures in the optical images were taken after each test. ....	81
<b>Fig. 5. 8.</b> a) Diagram shows the antifogging test principle for untreated and four modified glass, b) Optical pictures after 1h antifogging hot test. ....	82
<b>Fig. 5. 9.</b> Water fraction in (a) solution state, (b) solid state, (c) the proportion of water fraction in the solution state, and (d) the proportion of water fraction after drying.....	84
<b>Fig. 5. 10.</b> a) Optical picture for un-coated glass, b) the size and amount of condensation droplets. ....	85
<b>Fig. 5. 11.</b> The effect of bound water for preventing the fogging and microbial problems .....	86
<b>Fig. 6. 1.</b> Show the super-hydrophilic layers based on PVA and surfactant on the LDPE for greenhouses applications. ....	88
<b>Fig. 6. 2.</b> Show the differences between capillary and Marangoni flow and its effect on the silica nanoparticles distribution during evaporation.....	89
<b>Fig. 6. 3.</b> Show the effect of chitosan/silica nanoparticles coating on preventing microbial and fogging problems.....	91



List of Table

---

**List of Table**

<b>Table 1. 1.</b> Antifog performance ratings based on appearance. ....	24
<b>Table 2. 1.</b> The general characteristics of surfactants used in current work. ....	31
<b>Table 2. 2.</b> Chemical compositions of solutions used for preparing the anti-fogging layer .....	32
<b>Table 2. 3.</b> Showing the symbolic abbreviations for each method. ....	34
<b>Table 2. 4.</b> Chemical composition for different solutions.....	35
<b>Table. 2. 5.</b> Solutions chemical composition. ....	36
<b>Table 3. 1.</b> The comparison of key parameters between our work and other previous reports. ....	57
<b>Table 4. 1.</b> Accelerated dripping properties of antifogging coating films .....	71

## Chapter1 General Introduction

### 1.1 Background

Polymer is any family of natural or synthetic compounds comprised of massive molecules, known as macromolecules, multiples of smaller chemical units known as monomers [1]. Furthermore, they typically span from a well-known conventional polymer like polystyrene to natural biopolymers like DNA and proteins, which are necessary for biological structure and functional capabilities. Natural and artificial polymers serve crucial and extensive roles in everyday life due to their various features a wide variety of traits [2]. Plastics applications have gained popularity in industrial and residential due to several benefits such as ease of processing, enhanced thermodynamic, mechanical qualities, recyclability, and low cost [3,4]. Therefore, becoming the fastest-growing group of materials used to make customized items used in this context to package a variety of commodities, including electronics, health care, agriculture, construction industry, sport, transportation, and leisure sector [5].

The great majority of these polymers are made up of carbon atom chains with or without the addition of oxygen, nitrogen, or sulfur atoms. On the other hand, various molecular groups known as side chains are hung from the backbone before joining the polymer chain; (The backbone is the chain section that connects many repetition units and is on the main path). Therefore these side chains' structure influences the properties of the polymer, which is used to classify plastics [6]. Acrylics, polyesters, silicones, polyurethanes, and halogenated polymers are some instances of significant groupings that have been organized in this way. Furthermore, plastics are categorized according to the chemical process, such as condensation, polyaddition, and cross-linking [7]. Physical parameters like hardness, density, tensile strength, heat resistance, and glass transition temperature can also classify them. In addition, it can also be characterized based on its resistance to certain chemicals and processes, such as exposure to organic solvents, oxidation, and ionizing radiation. Other plastic groups focus on specialized manufacturing or product design qualities; thermoplastics, thermosets, conductive polymers, biodegradable plastics, engineered plastics, and elastomers are employed. [8]. Given the current worldwide plastic output of approximately 400 million tons (Mt) per year (Fig. 1. 1), with a massive rise, notably in developing markets defined by rapid industrialization, with a large number of spent plastics (already exceeding 150 Mt per year) [9], which Asia has produced half of the world production (Fig. 1. 2) [10]. Today, dozens of different types of plastics are manufactured, including commodity plastics (standard) and engineering plastics such as polyethylene (high-density (HDPE), polyvinyl chloride (PVC), polypropylene (PP), low-density (LDPE), linear low-density (LLDPE), polystyrene (PS), terephthalate (PETE or PET) and miscellaneous plastics (nylon polylactide, polycarbonate, etc.) [11].

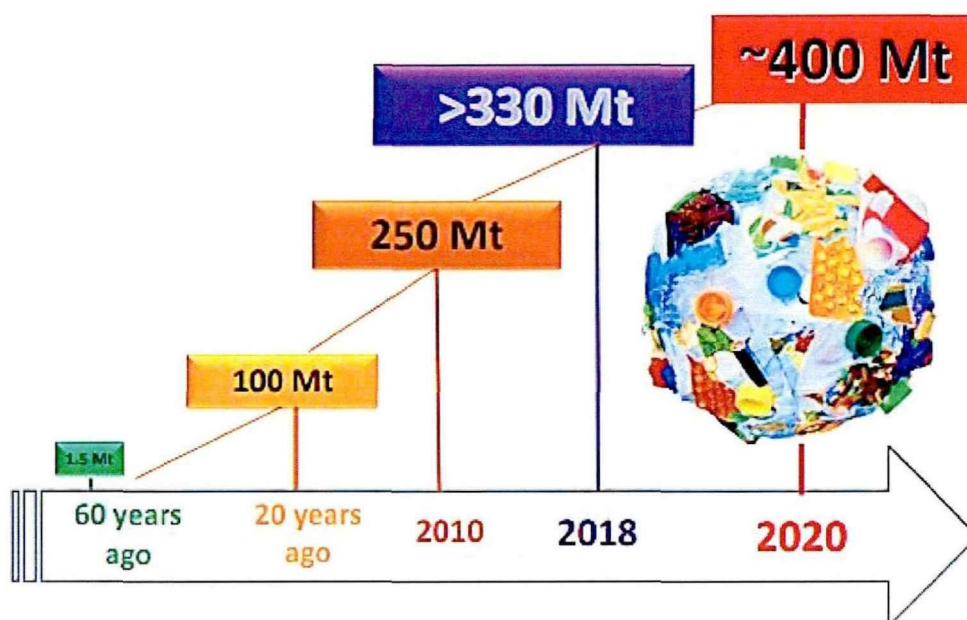


Fig 1. 1. The increasing volume of global plastic manufacturing [5].

## 1.2 Low-density polyethylene (LDPE)

The thermoplastic low-density polyethylene (LDPE) is generated from the ethylene monomer. Using a high-pressure free radical polymerization technique, Imperial Chemical Industries (ICI) created the first grade of polyethylene in 1933 [12], and it is still manufactured in the same manner. Despite competition from more sophisticated polymers, LDPE remains the most significant plastic grade, whereas, in 2013, the global LDPE market was worth around US\$33 billion. Polyethylene's are divided into three types Fig 1. 3: high-density (HDPE) with a density of  $0.941\text{-}0.967\text{ g/cm}^3$ [13], linear low-density (LLDPE) with a density of  $0.910\text{-}0.920\text{ g/cm}^3$  (Fig 1.3b), and low-density (LDPE) with a density of  $0.910\text{-}0.940\text{ g/cm}^3$  [11]. At room temperature, LDPE is not reactive, and it can resist temperatures of up to  $65\text{ }^\circ\text{C}$  ( $149\text{ }^\circ\text{F}$ ) continuously and up to  $90\text{ }^\circ\text{C}$  ( $194\text{ }^\circ\text{F}$ ) for a short time; however, some solvents cause it to swell. Furthermore, it is extremely flexible, durable, transparent, and opaque. LDPE is commonly used in manufacturing containers, dispensing bottles, wash bottles, tubing, computer components, agricultural applications, and different molded laboratory equipment. (Fig 1. 4).



Fig 1. 2. Plastic production by region 2019 [10].

### 1.2.1 LDPE uses in agriculture

Covering greenhouses (Fig. 1. 5a) and high tunnels (Fig. 1. 5b) are the most common application for LDPE films in the agriculture section [15]. Greenhouses are constructed to preserve plants from severe conditions and offer warmth all year. Furthermore, they aid in the conservation of water in water-stressed areas. Crops require a steady and adequate environment to produce a sufficient yield. These conditions are not usually provided because most are subject to weather extremes.

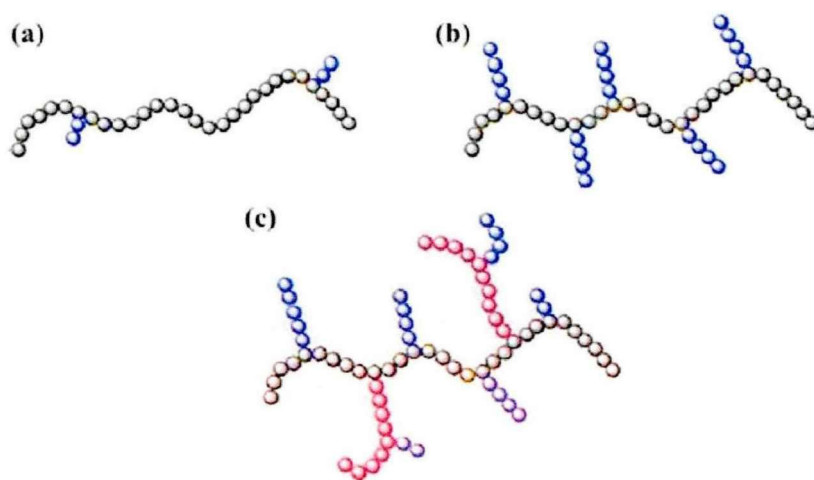


Fig 1. 3. PE Structure types (a) HDPE, (b) LLDPE, (c) LDPE [10].



Fig. 1. 4. Application of the LDPE in daily life [14,15].

As a result, studying these plastic films is an important problem in developing technical recommendations for a dependable greenhouse design and covering, creating more effective use of the film, and obtaining a longer usable lifetime of LDPE films [15]. Nowadays, their lifespan ranges from 6 to 45 months, depending on the photo stabilizers employed, geographic region, pesticide use, and other factors [16]. The European standard EN 13206:2001, which covers thermoplastic films in agriculture and horticulture, was published, and it includes guidelines for determining the lifespan, size, mechanical and optical characteristics, and IR opacity [17]. However, there is no data on condensation behavior (anti-drip and anti-fog impact) or pesticide effects on weather. Greenhouses are primarily located in two geographic regions: The far east (particularly China, Japan, and Korea), which accounts for over 80% of the world's greenhouse-covered land, as well as the Mediterranean basin, which contributes to around 15% of the total. The area covered by greenhouses has gradually risen at a rate of 20% per year during the previous decade Fig. 1. 6. Europe's development is sluggish, but Africa and the middle east are rising at 15–20 % each year [18]. The example of China is fascinating since it has increased in size from 4200 hectares in 1981 to 1,250,000 hectares in 2002 (30% / year). As a result, the amount of plastic film used for this application would be around 1,000,000 tons/year.

### 1.2.2 Key properties of greenhouse covers

Some parameters are essential while using plastic films in agriculture, especially in greenhouses, such as durability, optical properties, infrared transmission, and anti-dripping or anti-fog effect. Greenhouse coverings are subjected to solar, thermal, and chemical deterioration (Fig. 1. 7a). As mentioned, greenhouse films have a

life span ranging from 6 to 45 months (Fig. 1. 7b). Recently, the provider in developed nations guaranteed a minimum lifetime of 1 to 4 farming seasons. The most significant criteria influencing the usable life span of greenhouse films to fall into two essential categories, as shown below [19–27]:

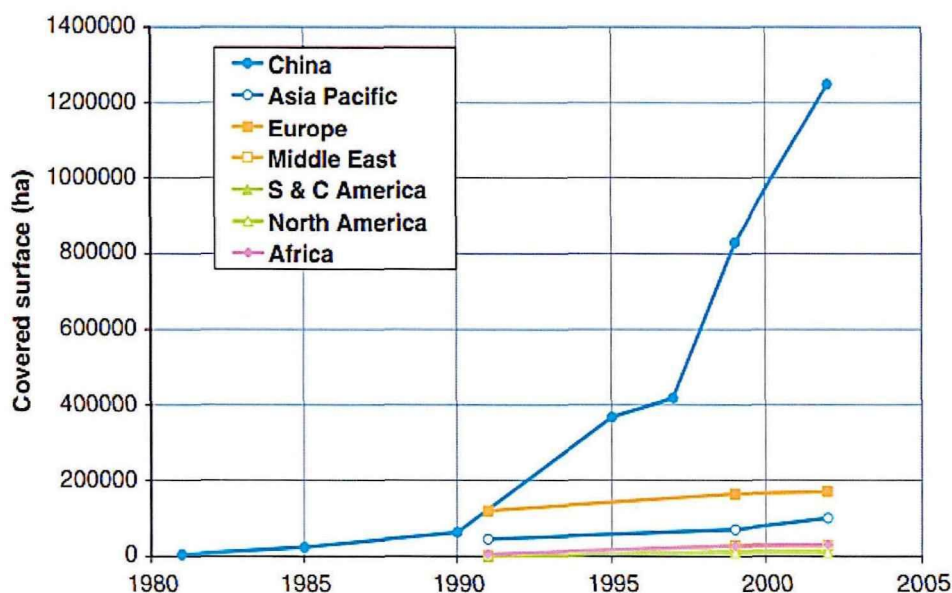


Fig. 1. 5. Agricultural surface covered with plastic film (greenhouses and walk-in high tunnels) [16].

### 1.2.2.1 Film inherent parameters

The kind of polymer (LDPE, EVA, EBA, LLDPE, and others) [28], film type (multilayer or monolayer) [29], additives for stability [30], other additives (colors, mineral fillers, etc.) [31], film thickness [32], and film manufacturing [33].

### 1.2.2.2 Environmental parameters

Structured content (galvanized iron, wood, etc.) [34], greenhouse architecture (ventilation, height, film attachment, etc.) [35], geographical and climatic characteristics (temperature, solar irradiation, rain, altitude, etc.) [36], and agrochemicals (composition of the chemicals, frequency of application, method of application, etc.) [37].





Fig. 1. 6. As-installed greenhouse coverings (a) after two years of use (b).

### 1.3 An overview of fogging problems

Fogging is a natural phenomenon when water vapor condenses on a solid surface with a temperature lower than the dew point of the surrounding air-water vapor mixture. In polymeric films, antifog chemicals are employed to guarantee that moisture condensation occurs as an undetectable water layer rather than a series of single droplets, which is unsightly and potentially dangerous [38]. When the difference in temperature between the atmosphere and the relative humidity is less than 2.5 °C, fog occurs. The dew point is when the quantity of water vapor in the atmosphere must be lowered to achieve saturation (relative humidity of 100 %) [39]. It is especially noticeable and essential in food packaging applications, where a lack of visibility creates visual and functional difficulties, eventually leading to product quality loss. This issue is also significant in agricultural films, especially the greenhouses, where fog may limit light transmission and affect crop production and quality.

#### 1.3.1 Fog formation principle on polyethylene films

Polyethylene (PE) is a hydrophobic polymer with around 30 dyne/cm [40]. Due to differences in surface tension between the liquid and the film. When a higher surface energy liquid, such as water (about 70 dyne/cm), comes into contact with a polyethylene film (30 dyne/cm). Young's formula [41] surface tensions of various interfaces, which in our instance, water on PE film exposed to air, may be represented as:

$$\gamma_{PA} - \gamma_{PW} - \gamma_{WA} \cos \theta = 0 \quad \dots\dots\dots (1)$$

Where  $\gamma_{PA}$  signifies the polymer-air interface's surface energy,  $\theta$  is the contact angle at equilibrium and represents the surface energy of the water-air interface, and  $\gamma_{PW}$  signifies the surface energy of the polymer-water interface shown in Fig. 1. 8.

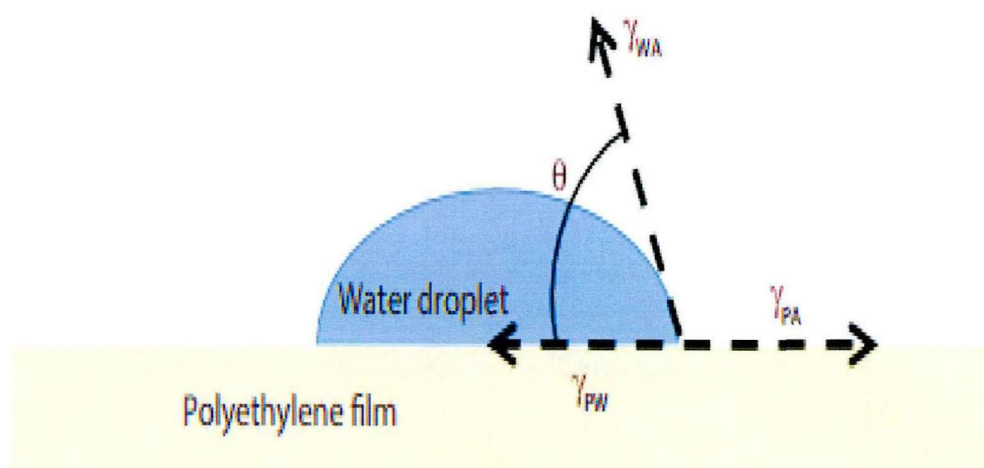


Fig. 1. 7. Parameters of Young's equation for a water droplet on a plastic film.

### 1.3.2 Anti-fog agents' mechanism

Water's surface tension can be regularly reduced by adding a small quantity of surfactant. The presence of anti-fog on the surface lowers the surface. The polymer interface becomes much more polar because of the difference in surface tension, and the contact angle between the droplet and the surface reaches zero [42]. The polymer's surface tension is now about equivalent to the surface tension of water. Several things must be considered when choosing an anti-fog film for greenhouses application, such as; The type of the polymer, the shape of the film, the temperature within the film, the product's lifetime, process factors, the kind of downstream processes, and the regulatory standards of the end uses are the primary considerations [43]. In packaging and agricultural films, internal migratory chemicals or exterior topical coatings were anti-fogging agents. Internal additives are mobile by nature and will exhibit some incompatibility with the polymer matrix, causing them to migrate to the polymer film's surface and lower the surface tension of condensed water droplets. After that, the depleted ingredient will be refilled regularly by a new migrating antifog from the film's inside [44]. Internal antifogs' effectiveness is highly dependent on their capacity to move at the proper rate over time.

In some situations, adding a compatibilizer, such as linear low-density polyethylene (LLDPE) grafted with maleic anhydride or sorbitan monoester in low-density polyethylene (LDPE) film, has been demonstrated to considerably minimize antifog migration, which may result in a more prolonged antifogging effect in the film [45]. Dip-coating and roller processes or spray applications apply for external coatings [46]. Externally applied coatings will behave similarly to migrating solutions; they both serve the same purpose, to increase the polymer's wetting characteristics and to have water condense as a thin continuous layer. External coatings can

be highly efficient, but they have some significant drawbacks. They are frequently inefficient in the long run because they lack a reservoir of additives to draw from when a thinly coated layer is depleted. External coatings sometimes need an additional processing step, which raises the overall cost of the procedure [47]. Therefore, internal additives are the preferred and most commonly utilized for PE films. Antifog emulsifiers reduce the contact resistance between the polymer surface and the liquid. It is a molecule that contains both non-polar and polar elements. Fatty acid esters are often employed because their polar hydroxyl groups hydrogen binds with water, decreasing the polymer-water interfacial tension. The nonpolar part is usually between 12 and 18 carbon atoms long. The hydrocarbon chain regulates the rate of additive migration through the polymer matrix. Efficient antifog is sufficiently hydrophilic to change surface tension at the polymer-water interface while also having the precise molecular weight to regulate migration for both short- and long-term efficient performance. Most antifog chemistries contain edible oils or fatty acids, polyvalent alcohols like glycerol or sorbitol, and organic acids. Glycerol mono-oleate, for example, is a distilled monoglyceride is a prominent antifogging agent.

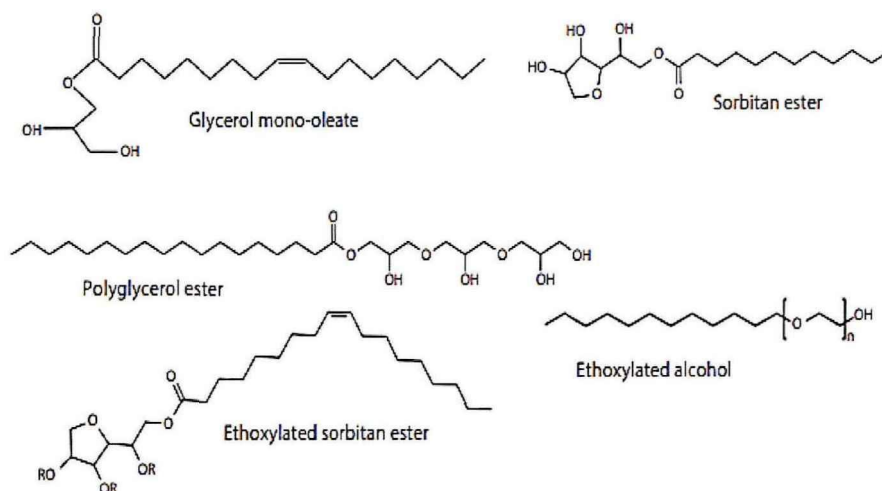


Fig. 1. 8. Chemical structures of classes of antifogging.

Interest verification of fats or oils with glycerol results in monoglyceride. This process is known as glycerolysis. Distilled monoglyceride is produced using molecular distillation by extracting monoglycerol from di- and triacylglycerols. This product comprises at least 90% monoacylglycerol, with the remainder being diacylglycerols and trace quantities of triacylglycerols [48]. Polymerized glycerol is esterified with fatty acids such as palmitic or stearic acid to form a polyglycerol ester combination. This mixture is then molecularly distilled to provide hydrophilic, nonionic emulsifiers suitable for antifog applications. Dehydrating sorbitol yields sorbitan, which may be esterified with fatty acids. Based on the sorbitan to the fatty acid molar ratio (STES), the end product will mostly consist of sorbitan monoacyl esters (SMS) or sorbitan triacyl esters (STE). Ethoxylated sorbitan esters and ethoxylated alcohol are two more antifog chemicals. Fig. 1. 9. depicts the

molecular structure of the most widely utilized types of antifog. The best antifog depends on economic, technological, and regulatory considerations.

### 1.3.3 Antifogging film preparation in the current industrial field

The primary material for producing the antifogging film is polyethylene (PE), frequently used in film blowing processes in various sectors, including mulching films, greenhouse films, carrier bags, and packaging applications. Fig. 1. 10. Showing a similar approach for creating an external antifogging layer on polyethylene films manufactured in the industrial field. The synthesizing of the layer starts with the production of the film substrate by a film blowing machine. The process then proceeds directly via the plasma treatment phase to produce carboxyl groups on the surface, increasing the hydrophilicity of the film. Then it passes through a box containing a hydrophilic solution to create the best wettability results. The last stage is drying to allow the solvent to dissipate. Therefore the thickness of the substrate, applying corona discharge, coating process, and drying are essential parameters needed to synthesize the greenhouses film, which is reflected in the final applications [49].

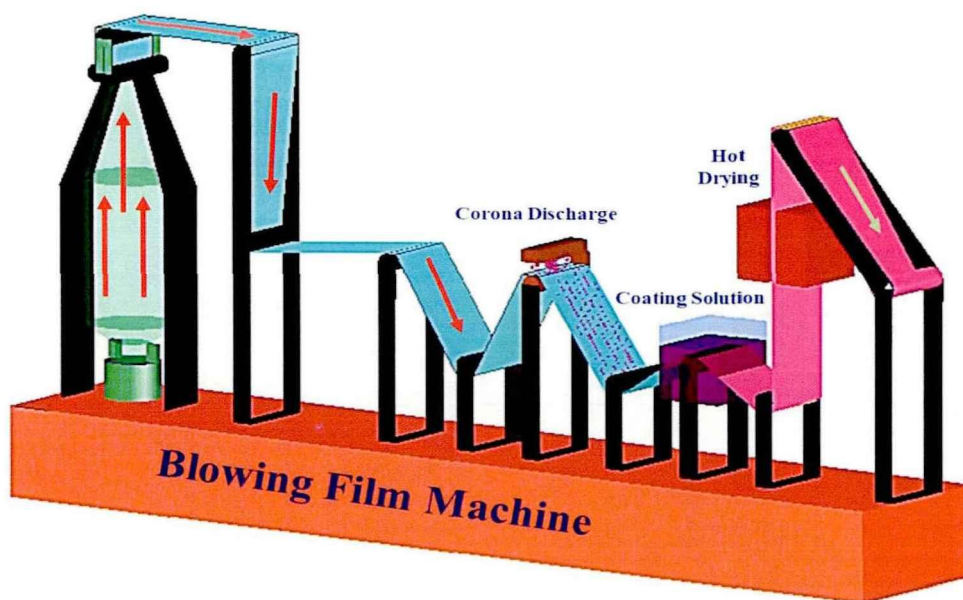


**Fig. 1. 9.** The diagram clarifies producing LDPE film followed by the plasma treatment and coating process applied in industries.

### 1.3.4 Antifogging performance evaluation

Antifogging performance is often a visual assessment of film clarity to ensure that as maximum light as possible enters the enclosure, keep huge drops from landing on young plants causing harm and sickness, and prevent plant "burning" induced by significant drop lens action [49]. The antifog property is graded through,

ranging from zero visibility (water droplets on the film) to transparent (water distributed as a thin continuous layer over the polymer surface). Table 1.1 contains the rating scale. This test is often performed on food packaging in two stages: cold fog (5°C) and hot fog (60°C). Greenhouse films are examined similarly, except that the test arrangement will typically provide a small-scale greenhouse that may be seen in a laboratory [50].

#### 1.3.4.1 Hot fog test

The hot fog test is carried out the same way as the cold fog test. Half-fill a 250 mL beaker with tap water and place it in a 60 °C water bath. (Fig. 1. 11a). The observations are made over three hours, and the test may be repeated at various intervals after extrusion to calculate the anticipated antifog lifespan.

**Table 1. 1.** Antifog performance ratings based on appearance.

Rating	Performance	Description
a	very poor	An opaque layer of small water droplets
b	poor	An opaque or transparent layer of large droplets
c	poor	A complete layer of large transparent drops
d	acceptable	Some drops randomly scattered
e	excellent	A transparent film displaying no visible water

#### 1.3.4.2 Cold fog test

Two-thirds of a 250 mL beaker is filled with tap water. The glass is wrapped in test film and placed in the refrigerator for three hours (5 °C), as shown in Fig. 1. 11b. Throughout the test period, the condensation of water on the film is examined and graded using the scale in Table 1.1.



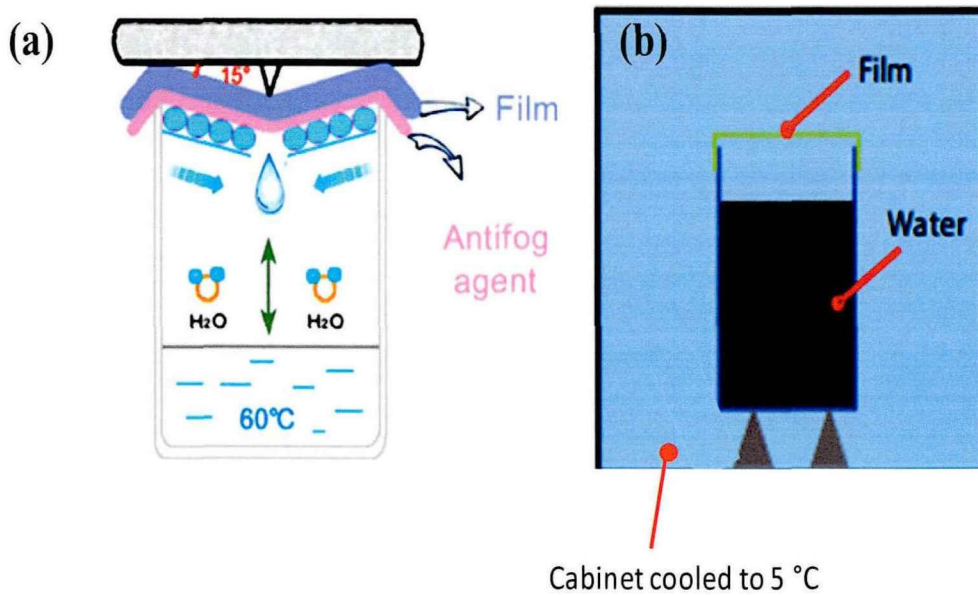


**Fig. 1. 10.** Testing films for fog properties: (a) hot fog test and (b) cold fog test schemat [46].

#### 1.4 Corona discharge

Corona discharge techniques have been used for almost a century, dating back to Lodge's first electrostatic precipitator [51]. Since then, the corona has been widely employed in various commercial applications and is gaining popularity in other areas. Corona process applications highlight one of two features of the discharge: the ions produced or the vital electrons that create plasma. The polarity of the release and the features of the gas mixture, particularly the electron attaching species, dictate the identities of ions. The electron energies are determined by the properties of the gas and the technology used to generate the corona [50]. The corona-induced plasma zone will generally take up a small portion of the entire process volume in an ion-based application. The plasma will take up most of the space in an electron-based process.

##### 1.4.1 Type of corona discharge

Corona discharges vary in form and size based on the field's polarity and the electrodes' location. In the needle-plate electrode design, when the applied voltage for positive corona rises, discharges go from bursting pulse corona to streamer corona, glow corona, and spark discharge (Fig. 1. 12). The first type of negative corona is the same as the supplied load increase, the shape becomes Trichel pulse corona, followed by pulseless corona and sparking discharge [50].



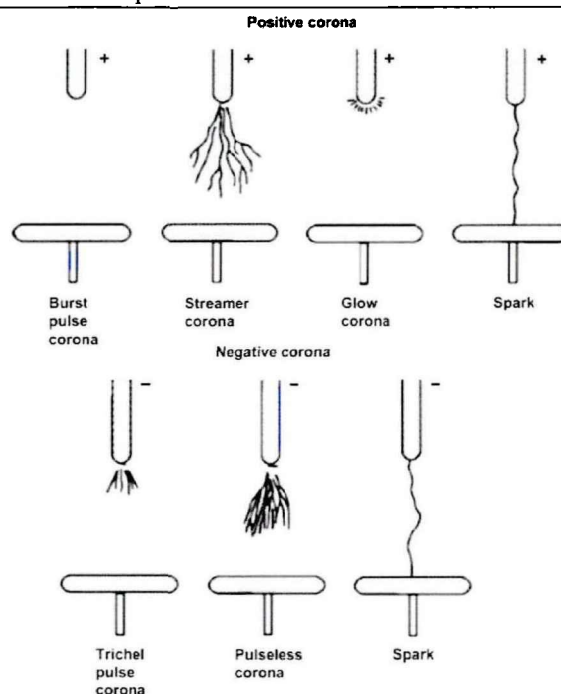


Fig. 1. 11. A diagram showing the many types of corona discharges.

When the input power increases, the Trichel pulse corona will be the first negative corona in the same geometry, followed by pulseless corona and spark discharge. Corona generated at a positive wire electrode in a wire-pipe, or wire-plate electrode design can take the shape of a tight sheath encircling the electrode or a streamer traveling away from the electrode. Corona produced by negative electrodes might take the form of a diffuse, fast-moving glow, or it can be focused into small active areas known as "tufts" or "beads" [50].

### 1.5 Coatings

The coating is a layer of material applied to the substrate's surface. The coating may be aesthetic, functional, or for both purposes [52]. Paints and lacquers are coatings with the dual purpose of protecting the substrate and being decorative. However, paint on large industrial pipes is for corrosion prevention and identification, e.g., blue for process water, red for fire-fighting control, etc. Functional coatings can modify the surface characteristics, such as adhesion, wettability, corrosion resistance, or wear resistance [53].

On the other hand, such as semiconductor device production (when the substrate is a wafer), A new property, like a magnetic response or electrical conductivity, is introduced by the coating. It becomes a vital component of the completed product. Layers can have various properties, including corrosion/wear resistance, enhanced surface hardness, altered surface roughness, thermal/electrical insulation, improved wettability, hydrophobicity, and so on [51].

### 1.5.1 Coating processes

Coating processes can be divided into the following categories: Chemical and electrochemical techniques [50], Vapor deposition [50], Spraying [51], Roll-to-roll coating processes [52], Physical coating processes [53].

### 1.5.2 Physical coating processes

Three methods in this technique include Langmuir Blodgett [54], spin coating [55], and dip coating [56].

### 1.5.3 Coating materials

#### 1.5.3.1 Silica nanoparticles.

A nanoparticle is a pretty small particle that ranges from 1 to 100 *nm*. Incomprehensible to the naked eye, Nanoparticles can have radically different physical and chemical characteristics than their bigger material counterparts. They are used in various medical, electronics, optics, communications, energy, and the environment [57 - 58]. Many of these applications need the connection of nanoparticles with macromolecules such as proteins, polymers, and surfactants to get functional objects [60 - 62]. The qualities of both nanoparticles (size, shape, surface roughness, charge density, etc.) and macromolecules (size, shape, surface roughness, charge density, etc.) impact the interaction of two components, nanoparticles and macromolecules (type, charge, shape, solution conditions, etc.) [63 - 67]. A variety of variables contribute to the interaction of macromolecules on the surface of nanoparticles, including electrostatic force, covalent bonding, hydrogen bonding, nonpolar contacts, hydrophobic interactions, and so on [68,69]. Depending on the system situation, these interactions can result in various structures [70,71]. The charge state of the macromolecule can alter the degree of interaction between nanoparticles and macromolecules, and hence the structures that follow [62][67].

#### 1.5.3.2 Surfactant

Surfactants reduce surface tension (interfacial tension) between two liquids or between a liquid and a solid. Surfactants include detergents, wetting agents, emulsifying agents, and dispersants. "surfactant" refers to a surface-active substance and a solvent mixture. [68]. The majority of surfactant "tails" are similar, consisting of a branching, linear, or aromatic hydrocarbon chain. Fluorocarbon chains are present in fluor surfactants, whereas siloxane chains are found in siloxane surfactants. In several vital surfactants, a polyether chain terminates in a highly polar anionic group. Polyether groups are usually composed of ethylated (polyethylene oxide-like) sequences to enhance a surfactant's hydrophilicity.

On the other hand, polypropylene oxides can enhance the lipophilicity of a surfactant. Surfactants are frequently classified using the polar head group. A non-ionic surfactant's head contains no charged groups anionic surfactant's head is either net positive or net negative in charge. If the amount is negative, the surfactant is anionic; if the charge is positive, the surfactant is cationic. If a surfactant possesses zwitterion, it has a head

with oppositely charged groups. Suppose a surfactant has two oppositely charged groups in its head. Surfactants of each commonly encountered kind include sulfate, phosphate, Anionic, carboxylate derivatives (Fig. 1. 13).

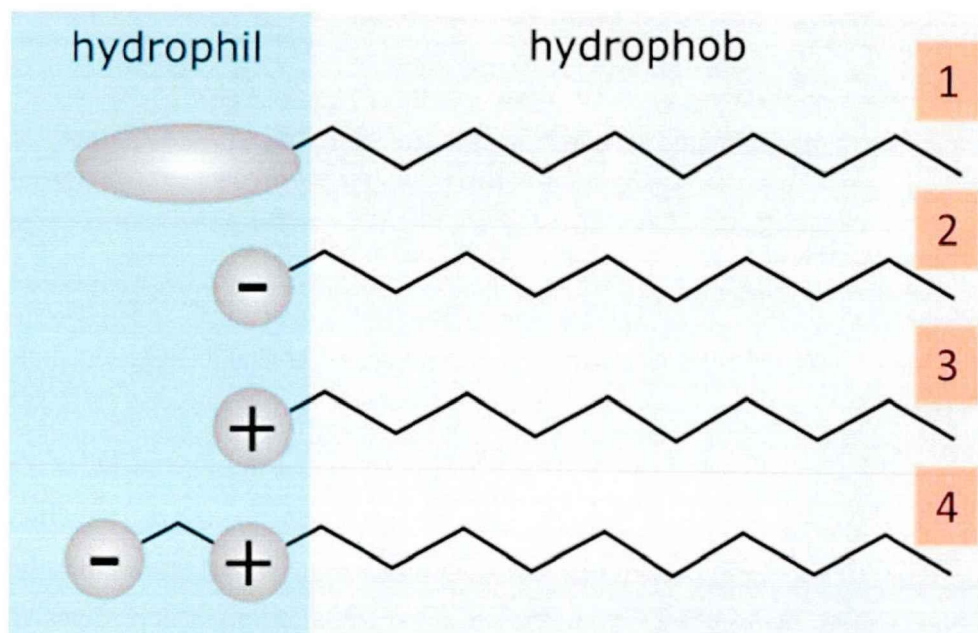


**Fig. 1. 12.** Surfactant categorization based on head composition: 1. nonionic, 2. anionic, 3. cationic, and 4. amphoteric.

### 1.5.3.3 Polymer coatings

Polymer coating refers to the top polymer layer applied to any substance (typically the substrate) for specific purposes [69]. The coating process involves covering a substrate with polymers and then allowing them to settle on the substrate's surface. The resin may cure or polymerize following coat application, depending on the polymer utilized for coating. Epoxy, polyurethane, polytetrafluoroethylene, acrylics, cellulose, biopolymers, and other polymers have been employed as coatings in various technical applications. Polymer, polymeric composite, and nanocomposite coatings are being used in an increasing number of applications and industries, aeronautical and automotive parts for corrosion resistance, thermal stability, and strength, as well as maritime constructions, kitchen goods, biomedical gadgets, cosmetic reasons, and energy devices [75,76]. Many coating processes have effectively covered substrate surfaces, such as spin, dip, doctor blading, solution casting, extrusion/dispersion, spray, gravure, and printing. These are only a few examples of coating techniques [77,78]. Others coating techniques are often chosen based on their ease of fabrication, cheap cost, and high-volume manufacturing. Conducting polymers have been utilized to create innovative coatings to protect metals against corrosion. Dopants have also been used to regulate or prevent corrosion in conducting polymers [74].

Antimicrobial compounds in coatings have been investigated as an appealing alternative for protecting materials against microorganisms and environmental impacts in the packaging sector. For future applications [75], the barrier, mechanical, and physical characteristics of such coated packing sheets have been studied. As a result, polymer coatings with enhanced wear resistance, tissue engineering, mechanical strength, Antimicrobial surfaces, medication delivery, orthopaedic materials, resistance to corrosion, cardiovascular stents, and electrical conductivity have all found use as biosensors [81,82]. A coating is a covering applied to a surface, also known as the substrate, using functional or aesthetic purposes [78]. Polymers and resins are used to create organic coatings [84,85]. The polymer can be either natural or synthetic, and it is typically produced as a liquid to form a thin surface coating. The material is coated onto a supporting substrate during the polymeric coating process. Metal, ceramic, and synthetic substrates can all benefit from polymer coatings. Polymeric coatings can give excellent adhesion, protection, and desired properties to the surface underneath. Polymer coatings can be applied to metal, ceramic, and synthetic substrates. Polymeric coatings may provide excellent adhesion, protection, and desirable characteristics to the surface underneath. Poly(vinyl chloride) (PVC), phenolics, acrylics, epoxy, silicone, and polyurethane are examples of natural and synthetic rubber, and other polymeric coatings are only a few examples [81]. Polymeric coatings may be applied to several substrates utilizing various methods, with finely adhered to the substrate to not detach or deteriorate due to heat, moisture, or other chemicals [82]. The usage of conductive polymer coatings has proven effective in metal corrosion prevention [83]. In this sense, polyaniline has been proven to be effective. Similarly, chemical oxidative polymerization created polyaniline/clay Nanocomposite coatings that provide excellent barrier preservation and corrosion resistance [84]. The nanocomposite coating outperformed the pristine coating in terms of performance. Polypyrene has also been shown to improve steel protection. Several approaches for polymer coatings with diameters ranging from a few millimeters to tens of nanometers (nm) have been developed, some of which are addressed in this section. Basic solution, dip coating, and spin coating technologies are examples of polymer coating methods. The polymer solution coating method was created to coat a polymer solution on a substrate easily and evaporate at the correct temperature [85].

Fig. 1. 13 presented the overall ideas of the three works completed in this thesis in the field of surface modification for specialized purposes such as agriculture and medicine. The first study, named " Nanoparticle Deposition Pattern During Colloidal Droplet Evaporation as in-situ Investigated by Low-Field NMR: The Critical Role of Bound Water", solves one of the serious coating problems (inhomogeneity) by employing a novel strategy and investigation, utilizing low field NMR. Following the solution to the coating issue, the high-efficiency hydrophilic layer was applied to the LDPE film using in agriculture, particularly in greenhouse applications, which entitled " Polyvinyl Alcohol (PVA) Based Super-Hydrophilic Anti-Fogging Layer Assisted

by Plasma Spraying for Low-Density Polyethylene (LDPE) Greenhouse Films". Our research was then expanded to glass applications, where we successfully produced new antifogging and antibacterial coatings with better mechanical properties " Dual-Functional Antifogging/Antimicrobial Based Natural Polymer Coating for Glass Applications as Investigated by Low Field NMR".

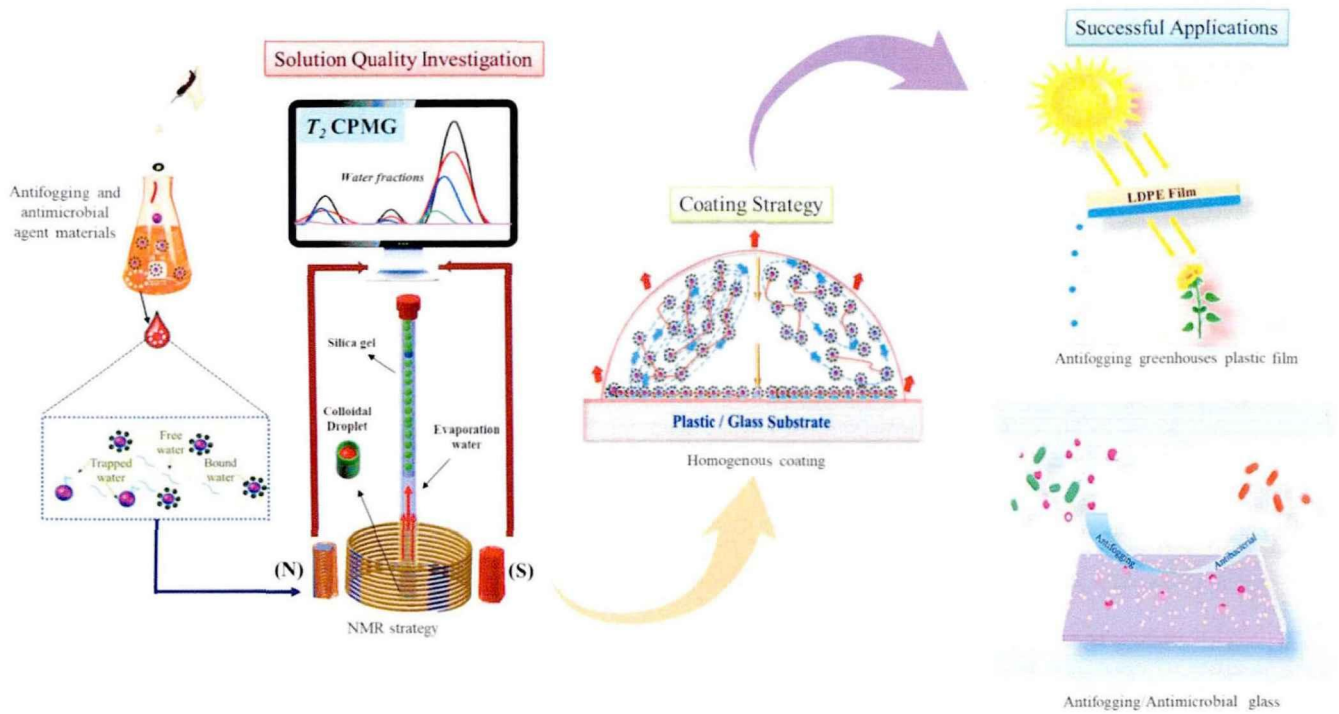


Fig. 1. 13. The overall research idea.

## Chapter2 Experiments and Methodology

### 2.1 Materials

Low-density polyethylene (LDPE) (Ethylene-octene Copolymer, XUS61530) was provided by Dow. Polyvinyl alcohol (PVA) with a polymerization degree of 1700 was supplied by Anhui Wanwei High-Tech Material Industry Co., Ltd, China. Silica nanoparticles of (SiO<sub>2</sub>, AEROSIL 200 with a diameter of 12 nm) were obtained from Evonik, Degussa. Tris-buffered saline (TBS) consists of (NaCl,  $M_w = 58.44$ ), and Tris base (Reagent grade  $\geq 99\%$ ) was purchased from Biosharp, Hefei, and Sigma-Aldrich, respectively. Solarbio Beijing Solarbio Science & Technology Co., Ltd supplied two types of surfactants, Polyoxymethylene sorbitol ester (T-20) and Octyl phenol ethylene oxide (Triton x-100) (Table 2. 1). Sodium dodecylsulfate (SDS) Solarbio Science & Technology Co., Ltd. Beijing, China. The Corona discharge was received from China's Ruian Zhi Lin Technology Co., Ltd. The polysaccharide polymer chitosan is provided by Shanghai Macklin Biochemical Co., Ltd., Shanghai, China. Glycerol is supplied from Saan Chemical Technology, Shanghai Co., Ltd. in China. Acetic acid is supplied from Shanghai Wokai Biotechnology Co., Ltd. in China. Shanghai Xingtal Industrial Glass Products Co., Ltd. provided the glass substrate in China. All materials were used as received.

**Table 2. 1.** The general characteristics of surfactants used in current work.

Name	Trade Name	Chemical Formula	Molecular Weight ( $M_w$ )	Type of Surfactant
Sodium dodecyl sulfate	(SDS)	$\text{NaC}_{12}\text{H}_{25}\text{SO}_4$	288.3	An-ionic
Polyoxymethylene sorbitol ester	(T-20)	$\text{C}_{58}\text{H}_{114}\text{O}_{26}$	1227.7	Non-ionic
Octyl phenol ethylene oxide	(Triton x-100)	$\text{C}_{34}\text{H}_{62}\text{O}_{11}$	647	Non-ionic

### 2.2 Processing of LDPE film and antifogging layer

#### 2.2.1 Preparation of LDPE Film

The LDPE film was prepared through a laboratory-made blown film machine. A detailed description of the film-blowing apparatus setup is referred to in our previously published work [86], whereas only key processing parameters are provided here. The bubble was controlled with a diameter of 60 mm. Extrusion

velocity  $v_e$  was 2.39 mm/s, while take-up velocity  $v_t$  was 57.26 mm/s, with a corresponding take-up ratio ( $TUR = v_t/v_e$ ) of 24, and the blow-up ratio (BUR) for high optical performance is 2 [87]. The thickness of the obtained film was 80  $\mu\text{m}$ .

### 2.2.2 Preparation of PVA anti-fog solutions

1 g of PVA was dissolved in 100 mL deionized water and whirled for 1 h at 95°C until thoroughly dissolved. After then, The solution was chilled until it reached room temperature. Three different surfactants were prepared separately as a solution (10 wt.%) at room temperature. TBS buffer (10 wt.%) was prepared by mixing 8.8 g of NaCl with 2.4 g of tris-base and magnetically stirring at room temperature for 1 hour. The addition of surfactants, TBS, and silica nanoparticles to the PVA solution by weight is presented in Table 2.2.

**Table 2. 2.** Chemical compositions of solutions used for preparing the anti-fogging layer

Coating Materials on LDPE Film	PVA (1%) (g)	X-100 (10%) (g)	T-20 (10%) (g)	SDS (10%) (g)	TBS (10%) (g)	SiO <sub>2</sub> (g)	Sample Name of Coated LDPE Film
LDPE	—	—	—	—	—	—	LDPE
LDPE– (PVA/X-100)	20	0.1	—	—	—	—	L-(P/X)
LDPE– (PVA/T-20)	20	—	0.1	—	—	—	L-(P/T)
LDPE– (PVA/SDS)	20	—	—	0.1	—	—	L-(P/S)
LDPE– (PVA/ X-100/TBS)	20	0.1	—	—	0.1	—	L-(P/X/T)
LDPE– (PVA/T-20/TBS)	20	—	0.1	—	0.1	—	L-(P/T/T)
LDPE– (PVA/X-100/TBS/SiO <sub>2</sub> )	20	0.1	—	—	0.1	0.05	L-(P/X/T/Si1)
LDPE– (PVA/X-100/TBS/SiO <sub>2</sub> )	20	0.1	—	—	0.1	0.1	L-(P/X/T/Si2)
LDPE– (PVA/X-100/TBS/SiO <sub>2</sub> )	20	0.1	—	—	0.1	0.15	L-(P/X/T/Si3)

### 2.2.3 Anti-fogging coating processes

Several primary coating techniques are applied to select the efficient method for an excellent anti-fogging film with high wettability, transparency, and haze performance. Fig. 2. 1 Shows the variety of coating

techniques applied for the LDPE surface, and Table 2. 3 shows the symbolic abbreviations for each method. The anti-fogging coating was prepared in Fig. 2. 2. corona treatment was performed in a corona discharge (Ruian Zhi Lin Technology Co, Ltd, China). With a fixed distance of 5 mm between substrates and corona electrodes, the operating parameters such as power and rolling speed were optimized to 300-900W and 15-115 mm/s, respectively. For homogeneous coating layers, the samples were kept at 50 °C on the coating machine for 30 minutes to let the coating agent fully react with the activated surface and evaporate the free water. Afterward, it was exposed to hot air at a temperature of 95 °C by a homemade dryer. Later, the coating of a super-hydrophilic layer on treated LDPE films was done using a coating machine (Xiamen xinkerui Machinery Technology Co. Ltd, Haicang, Xiamen China). The coating speed was fixed at 30 mm/s, the setting thickness was 5 $\mu$ m, and the coating temperature was set as 50 °C (ambient temperature 23 °C and 75% humidity). According to the contact angle results for power and speed, 900W and 15 mm/s, respectively, were selected as optimum treatment parameters for all subsequent coating experiments, with variable airspeed 1.5 ~ 2.5 m/s for 10 min to ensure complete evaporation of the solvent.

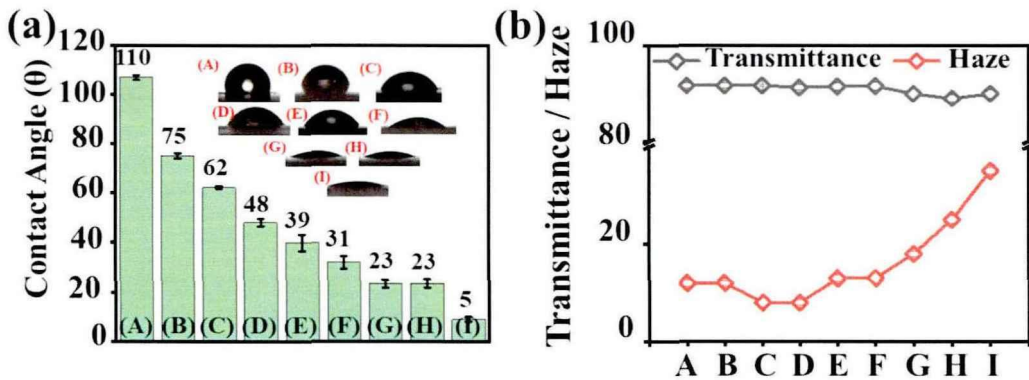


Fig. 2. 1. (a) Contact angle test for difference methods, (b) Transmittance and haze.

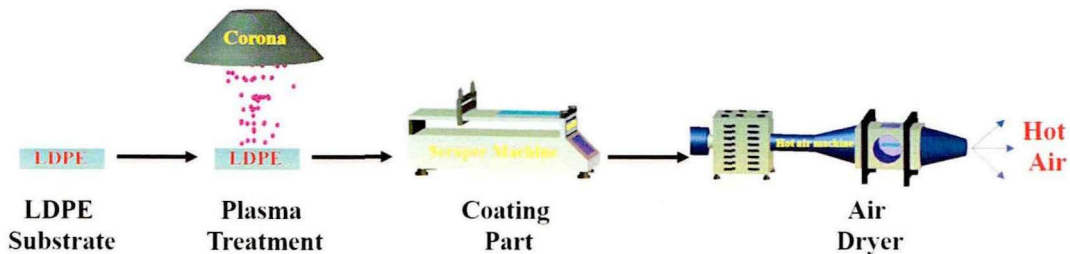


Fig. 2. 2. Schematic illustration of coating of anti-fogging layer on the LDPE substrate.



**Table 2. 3.** Showing the symbolic abbreviations for each method.

	<b>Steps</b>	<b>Abbreviation</b>
<b>A</b>	Pure LDPE	<b>LDPE</b>
<b>B</b>	LDPE + Corona (300 W)	<b>C/LDPE</b>
<b>C</b>	Corona(900 W) - PVA (Dip Coating) – drying (room temp -30 min) – (hot air 80°C - 10 min)	<b>C/DP</b>
<b>D</b>	Corona (900 W) – Layer of PVA (5µm - thickness) - Corona (700 W)	<b>C/LP/C</b>
<b>E</b>	Corona (900 W) – Layer of (PVA/SiO <sub>2</sub> ) (5µm-thickness) - drying (room temp - 30 min) – (hot air 80°C - 10 min)	<b>C/L(PVA/SiO<sub>2</sub>)</b>
<b>F</b>	Corona (900 W) – (PVA/SiO <sub>2</sub> ) Dip coating - Corona (900 W) - drying (room temp - 30 min) – (hot air 80°C - 10 min) - Corona (900 W)	<b>C/D(PVA/SiO<sub>2</sub>)/C</b>
<b>G</b>	Corona (900 W) - Layer of PVA (5µm) - Corona (900 W) - Layer of SiO <sub>2</sub> (0.01 mm thickness)	<b>C/LP/C/LS</b>
<b>H</b>	Corona (900 W) - Layer of PVA (5µm) - Corona (900 W) - SiO <sub>2</sub> Dip coating	<b>C/LP/C/DS</b>
<b>I</b>	Corona (900 W) – PVA Dip coating- Wash (distilled water - 5 minutes) - SiO <sub>2</sub> Dip coating	<b>C/DP/W/DS</b>

### 2.3 Surface modification of silica nanoparticles

The addition of silica, surfactant, and polymer to distilled water is shown in Table 2. 4. Colloidal solutions comprising silica nanoparticles and surfactant were mixed for 5 min with distilled water at room temperature, then heated to 60 °C for 3 h during magnetic stirring, and then cooled to room temperature before

further use. The solution included PVA polymer; first, the polymer was stirred in distilled water at 80 °C for 2 h until fully dissolved. Then, the temperature was reduced to 60 °C with the addition of silica nanoparticles for 3 hours magnetically stirring, then dropped to room temperature. All solutions are prepared with a pH of 7.5.

**Table 2. 4.** Chemical composition for different solutions.

Sample	SiO <sub>2</sub> (%)	Surfactant (%)	PVA (%)	Abbreviation name
1	0.5	-	-	Pure silica
2	0.5	0.1	-	Si+Su <sub>1</sub>
3	0.5	0.5	-	Si+Su <sub>2</sub>
4	0.5	1	-	Si+Su <sub>3</sub>
5	0.5	1	0.25	Si+Su <sub>3</sub> +PVA

#### 2.4 Controlling the evaporation rate

For colloidal droplets, three open systems are used to determine the effect of Evaporation Rate  $J$  on particle dispersion. The open system experiments on a piece of LDPE substrate were carried out at an ambient atmosphere with  $J = 4.3 \sim 7.6 \times 10^{-2} \text{ mg/min}$ , and two controlling tubes with  $J$  between  $5.5 \sim 7.1 \times 10^{-3} \text{ mg/min}$  and  $2.7 \sim 3.1 \times 10^{-4} \text{ mg/min}$  respectively. The reducing weight recorded the evaporation process. To gain the controlling evaporation rate  $J$  as mentioned above, a tube constructed of Teflon materials was designed to be used inside the NMR glass tube, with a diameter of 8 mm and 178 mm, as shown in Fig. 4 .2a. The tube was divided into two parts, sample- and cap-carrier, to improve the accuracy. Two holes of 1mm and 0.5mm diameter were punctured in the cover's center for control  $J$ . A piece of hydrophobic LDPE film with a diameter of 8 mm was placed on the sample carrier, then one drop of each solution (1  $\mu\text{m}$ ) was placed in the middle of the LDPE substrate. Afterward, the actual  $J$  was calculated under controlled humidity and temperature, 75% and 23 °C, respectively.

#### 2.5 Nanoparticles deposits formation

The known silica nanoparticle size (12 nm), various Sodium dodecylsulfate (SDS) surfactant concentrations, and polymer addition as colloidal solutions were placed separately as droplets in 1  $\mu\text{L}$  volume

over the hydrophobic LDPE film surface. Then three different evaporation rates ( $J$ ) were employed to deposit nanoparticles at controlled humidity and temperature (75% and 23 °C).

### 2.6 Preparation of the hybrid chitosan coating film

Following our previous work, the surface of silica nanoparticles was modified based on Sodium dodecylsulfate (SDS) surfactant [88] for better wettability and dismissed aggregation. In brief, as shown in Fig. 2. 3(a), a colloidal solution containing (MSN) and surfactant was mixed in distilled water for 5 min at room temperature, then heated to 60 °C for 3 h while stirring magnetically, afterward cooled to room temperature.

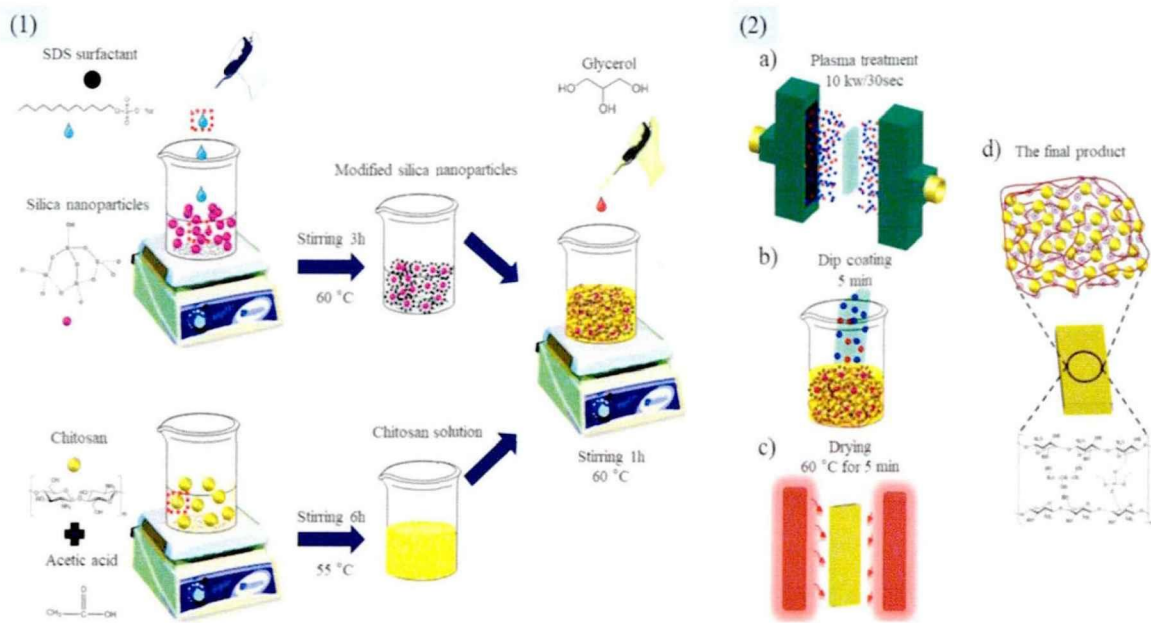


**Fig. 2. 3.** Schematic illustration (1) clarifies the steps of preparing hybrid chitosan coating solutions, (2) shows the steps for the dip-coating method for a glass substrate, (a) plasma treatment, (b) dip coating, (c) drying, (d) the final product.

**Table. 2. 5.** Solutions chemical composition.

Solution	Ch (%)	SDS/SiO <sub>2</sub> (%)	Glycerol (%)
Ch	1	-	0.5
Ch/SiO <sub>2</sub> (1)	1	$1.25 \times 10^{-3}$	0.5
Ch/SiO <sub>2</sub> (2)	1	$6.25 \times 10^{-3}$	0.5
Ch/SiO <sub>2</sub> (3)	1	$12.5 \times 10^{-3}$	0.5

Chitosan solution is produced by dissolving 1g of chitosan in 1% acetic acid solution. The mixture was then rapidly stirred for 6 h at 55 °C. Subsequently, 0.5 g of glycerol were added to the mixture solutions (Ch/SiO<sub>2</sub>) as a cross-linking at 60 °C, with continuous stirring for 1 h, later 30 min ultrasonic applied at the same temperature for bubbles free. The different mixture solutions containing MSN, chitosan, and cross-linking were obtained in Table 2. 5. Furthermore, the glass substrates were treated with plasma to enhance the carboxyl groups and increase the surface wettability for better adhesion, as shown in Fig. 2. 3(b1). The power of each glass was adjusted to 10 kW for the 30s on both sides Fig. 2. 3(b2). Afterward, the dip-coating procedure was done at room temperature for 5 min Fig. 2. 3(b3), followed by 24 h oven drying at 45 °C Fig. 2. 3(b4). The possible final structure was presented in Fig. 2. 4.

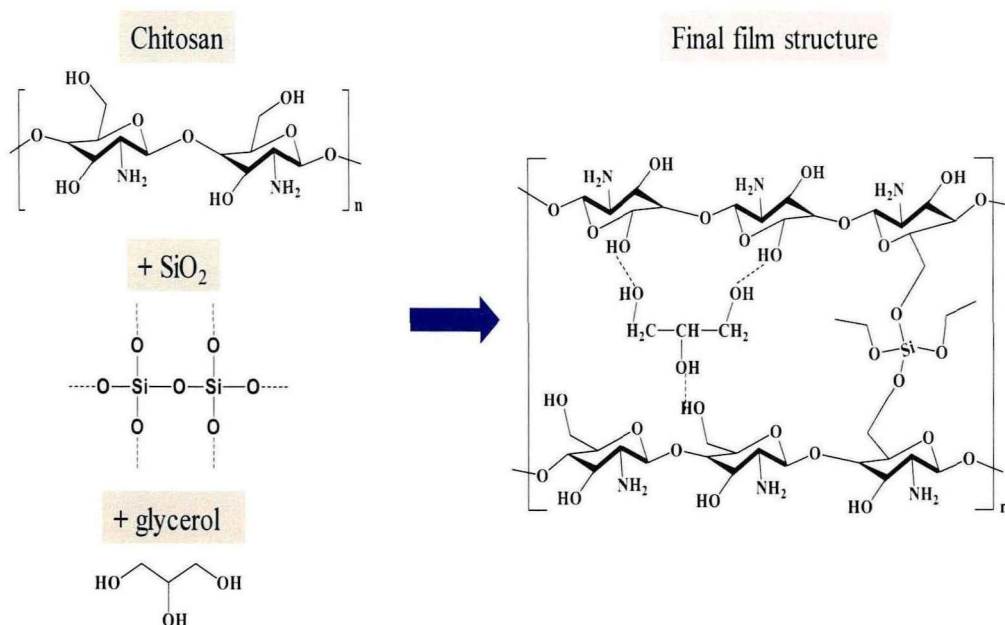


Fig 2. 4. Synthesis of Ch/SiO<sub>2</sub> hybrid film coating.

## 2.7 Characterization

### 2.7.1 Contact angle measurement

The contact angle was measured by an optical contact angle machine (model sdc-350, Dongguan city, China), including a high-performance digitizing adaptor and a CCD camera of high resolution. The 'LR-SDC-350 Automatic Tilt Contact Angle Measuring software precisely determined the contact angle. The static contact angle ( $\theta$ , degrees) of water in the air was measured by the drop method by gently dropping  $2.0 \pm 0.5 \mu\text{L}$  of distilled water droplets onto the substrate. Temperature and humidity were controlled at  $23 \pm 1^\circ\text{C}$  and  $75 \pm 2\%$ , respectively. The static contact angle was measured immediately after the first drop. At least three positions were tested to obtain an average value, and the angle between the droplet and tangent baseline at the droplet

boundary was taken as deposition. For the coffee ring effect part, the static contact angle was recorded after 4s for the open system-ambient environment and continuously detecting the volume decreasing every minute until the complete evaporation. For the open system-1mm and 0.5mm, the pictures were taken every 40 min.

### 2.7.2 Optical microscopy

The surface morphology was captured by optical microscopy (OM) (BX51TRF - Olympus Corporation, Tokyo, Japan). All samples were cut into ( $30 \times 10 \text{ mm}^2$ ) on rectangular glass for the anti-fogging films. Image capture was performed using NIS-Element software (Nikon Instruments, Sesto Fiorentino, Italy). For the spreading test,  $20 \mu\text{L}$  of  $\text{SiO}_2$  (5wt.%) were dropped on the surface of original and plasma-treated LDPE films and subsequently dried at room temperature for 1 hour. An optical microscope then directly checked the layer surface (Fig. 2. 5).

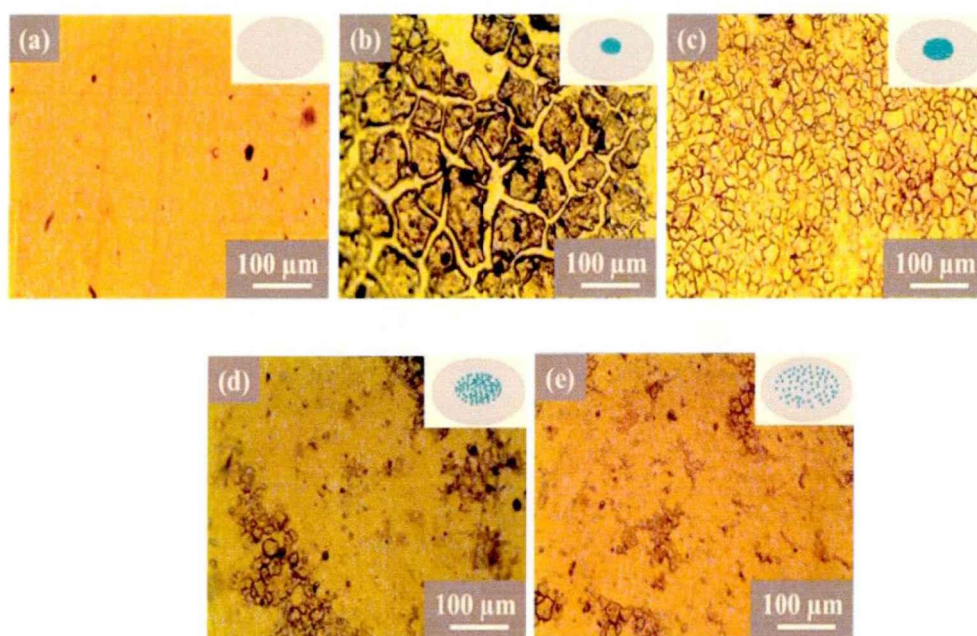


**Fig. 2. 5.** Optical microscope images for spreading silica on the LDPE surface according to the different plasma power. (a) untreated, (b) 300W, (c) 500W, (d) 700W, (e) 900W.

### 2.7.3 Optical properties

The optical properties of untreated and modified films were employed by a light transmittance/haze meter (SGW-820) dependent on GB/T2410-2008 standard test. For accuracy in the results, testing was repeated three times for each film.

### 2.7.4 Antifogging test

Two anti-fogging testing protocols were used to evaluate the performance of modified LDPE films. The first and ten drops time techniques reflect initial and continuous anti-fogging performance [89]. All tests were

performed according to QB/T 4475-2013 in a water bath (Gongyi City Yuhua Instrument Co. Ltd). The distance between the water surface and the film was fixed at 15 cm. The pressure hammer adjusted the anti-fogging film until its surface, and horizontal angle became  $15^\circ$ . A camera (Mimacro Machine Vision and Microscope Camera, China) was installed to track the water dropping process. The time elapsed between the start of the measurement and the first drop of water is the first drop time. The ten-drops time was calculated by taking the time necessary for 10 droplets of water to drop [90]. Long-life test, five samples were installed on a six-holder water bath (Changzhou Jintan Kexing Instrument Factory). Five types of modified LDPE films were placed on the instrument tube with a diameter of 80 mm and adjusted the distance between the water surface and film to 15 cm. The water bath was kept at  $60^\circ\text{C}$  lasting one month [91]. However, it was deemed to have lost its effectiveness when the condensation area of the film reached  $1/3$  [46]. The principle for the long-life test is shown in Fig. 2. 6. Also, the hot-vapor and cold-warm tests evaluated the Ch/SiO<sub>2</sub> layers against fogging characterizations. Both modified and unmodified glass were kept over a hot water bath at  $60^\circ\text{C}$  using the hot-vapor approach, then were photographed after 30 min. Therefore, the cold-warm test was obtained by freezing the samples in a refrigerator at  $-20^\circ\text{C}$  for 30 min and then directly exposed to the surrounding environment ( $25^\circ\text{C}$  and 75% humidity) [92].

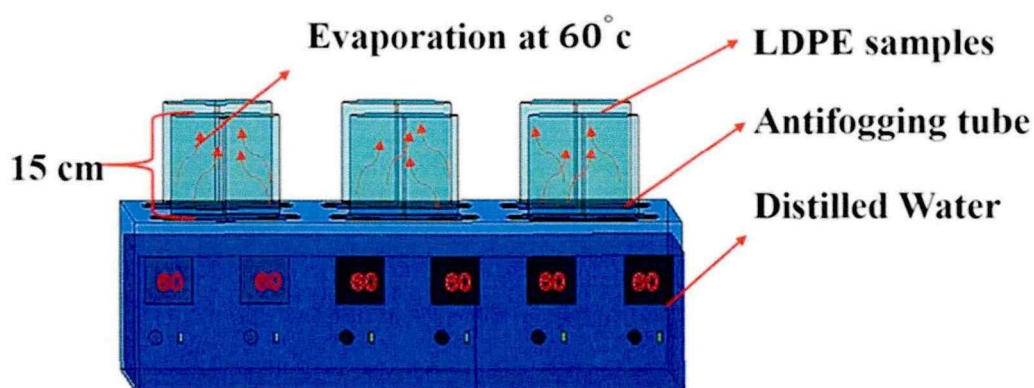


**Fig. 2. 6.** The diagram shows a one-month shelf-life antifogging test for five modified films.

### 2.7.5 Scanning electron microscope (SEM) measurements

SEM (scanning electron microscopy) with field emission (Gemini-SEM 500) was used to analyze changed films' surface morphologies and cross-sections. All samples were sputtered with a gold ion beam for 18 s before measurement.



### 2.7.6 Fourier transform infrared

Spectra of Attenuated Total Reflection Fourier Transform Infrared (ATR-FTIR) (Bruker Tensor 27, Germany). The photographs were obtained using a 4  $\text{cm}^{-1}$  camera in the 400–4000  $\text{cm}^{-1}$  spectral region.

### 2.7.7 Solid-state low-field $^1\text{H}$ NMR spectroscopy

Water's spin-spin relaxation time  $T_2$  was calculated using the CPMG technique [93,94]. On the Bruker minispec mq 20, a Larmor frequency of 19.95 MHz was used. The spectrometer's  $90^\circ$  pulse length was 2.78  $\mu\text{s}$ , The sluggish time for the receiver was 8.6  $\mu\text{s}$ . The film was split into little pieces 6 mm in diameter and flattened tightly on a homemade design before inserting into the NMR tube bottom. To decrease water evaporation during measurement, a quantity of desiccant silica gel filled in a PTFE tube with a diameter of 7 mm and a height of 100 mm was used. A water droplet of 10  $\mu\text{L}$  was laid on the center of the samples, and then the film was inserted carefully into the NMR glass tube. Totally 128 points were accumulated with the recycle delay time of 18 s. Secondly, the *in-situ* measurements were adopted to track the effect of additives (surfactant and polymer) on the change of droplet water fractions and the impact of different  $J$ . The scans and recycle delay time for *in-situ* measurements were 128 and 20s, respectively. The echo spacing was set to 1 ms, and the number of echoes was set to 3000, which corresponds to the point at which the NMR signal approaches the noise floor. All experiments were conducted at room temperature (23°C) and constant humidity (75 %). As shown in Fig. 2. 7, a sample containing silica nanoparticles modified by surfactant and enhanced by PVA polymer was used as an example for the fitting procedure to understand better how to identify the proportion of water fractions for solution states *in-situ* tracking.

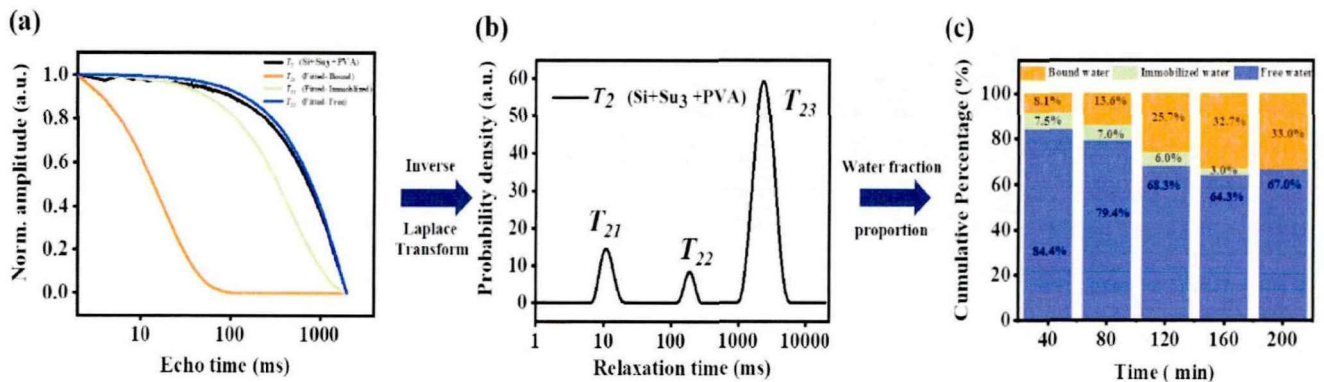


**Fig. 2. 7.** CPMG obtained the fitting process for  $T_2$ . (a) CPMG echo trains together with triple exponential decay function, (b) relaxation time distribution derived after Inverse Laplace Transform (ILT), and (c) proportion of water fractions during evaporation.

In Fig. 2. 7a, after acquiring the CPMG echo trains, the proportion of water fractions was calculated. The Inverse Laplace Transform (ILT) was utilized to quantify fractions of different water fractions ( $T_{21}$ ,  $T_{22}$ ,  $T_{23}$ )

(Fig. 2. 7b). Then the fractions in the solution state and during evaporation can then be calculated (Fig. 2. 7c). Here, these three peaks are assigned to  $T_{21}$  (1–10 *ms*) (Bound water),  $T_{22}$  (200–300 *ms*) (trapped water), and  $T_{23}$  (300–10000 *ms*) (Free water) [37,38,39].  $T_{21}$  is water that binds tightly to the nanoparticle.  $T_{22}$  is a cytoplasmic water binding, and  $T_{23}$  is free water in a bulk state. The Inverse Laplace Transform was adopted directly to obtain the  $T_2$  distribution of different water fractions. It can also help estimate time constants for following exponential decay function fitting. The distributed exponential curve fitting is performed by following multiple exponential decay functions;

$$y = A_1 \cdot \exp(-t/T_{12}) + A_2 \cdot \exp(-t/T_{22}) + A_3 \cdot \exp(-t/T_{23}) + y_0 \quad (1)$$

Where  $y$  is the residual magnetization at a specific relaxation time  $t$  after applying the first radio frequency pulse,  $A_1$ ,  $A_2$ ,  $A_3$  are the spin-spin relaxation amplitude.  $T_{12}$ ,  $T_{22}$ ,  $T_{23}$  represent the time scale in different time ranges such as;  $T_{12}$  means the shortest relaxation time (1-10 *ms*), which is related to the bound water,  $T_{22}$  is the time that represents the medium relaxation time of the trapped water (200–300 *ms*). And  $T_{23}$  is the longest relaxation time (300–10000 *ms*) related to free water, and  $y_0$  is the residual error [98–100]. Also, low field NMR was used to investigate adding *MSN* to chitosan structure in solution and solid states. Then, the relationship between water fractions proportion in the final layer (after drying) and their impact on preventing antimicrobial activity and antifogging formation was studied. For both states (solution and solid), the pulse lengths at 90° and 180° were 2.9 and 5.5 s, respectively. The number of scans was limited to 16, and the recycle time was set at 20 seconds. The echo spacing was adjusted at 1 *ms*, and the number of echoes was set to 3000, which corresponds to the point where the NMR signal approaches the noise floor. All trials were carried out at room temperature (23 °C) and constant humidity (75%). Following our previous work (216), the proportion of water fractions was estimated after applying the fitting process for the CPMG echo trains' data. Then Inverse Laplace Transform (ILT) was used to calculate the various water fractions ( $T_{21}$ ,  $T_{22}$ ,  $T_{23}$ ). The  $T_{21}$  (0.01-1 *ms*) time range described the fast relaxation rime related to the bound water.  $T_{22}$  (10–100 *ms*) is the medium relaxation time attributed to the immobilized water, and the longest relaxation time,  $T_{23}$  (300–10000 *ms*), describes the free water fraction (165).

### 2.7.8 Coatings' mechanical properties

An adhesion test was performed to check the robustness of the interaction between the substrate and the coating layer. After films exposure to the hot fog test for one day, the sandpaper abrasion test was carried out. A 35g weight was fixed above a ruler made of cork, the samples with the coated side were placed on the side facing the sandpaper, and then the ruler with the fixed samples was moved 10 cm along the sandpaper five times continuously [91]. The principle of the sandpaper test is obtained in (Fig. 2. 8a).



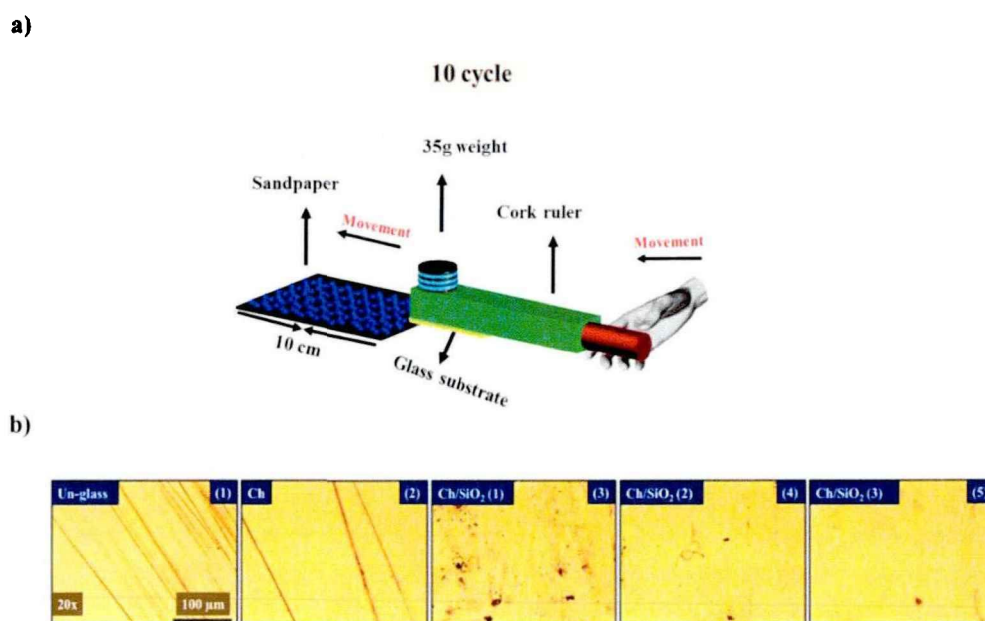


**Fig. 2. 8.** a) The principle of sandpaper test, applied for unmodified and modified glass 10 cycles for each sample, b) optical microscopy pictures after the mechanical test.

In addition, the scratch test was performed to evaluate the toughness of the coating  $Ch/SiO_2$  layer. After exposure to the hot-vapor test for one day, the sandpaper abrasion test was performed. The samples with the coated side were positioned facing the sandpaper (Fig. 2. 8b). The fixed pieces' ruler was continually moved 10 cm along the sandpaper ten times [91].

### 2.7.9 Antimicrobial test (Disk diffusion assay Antibacterial)

The antimicrobial efficacy of chitosan films augmented with *MSN* against *Escherichia coli* (*E. coli*) was investigated using a disk diffusion experiment, as previously described [101]. *MSN* ( $1.25 \times 10^{-3}$ ,  $6.25 \times 10^{-3}$ ,  $12.5 \times 10^{-3}$  %) was added to the chitosan structure and coated the glass substrates, were sterilized with UV radiation, and cut into a disk shape ( $2 \text{ cm}^2$ ), then placed onto the surface of LB agar plates, which had been streaked with 100 L of 106 *E. coli* CFU. The plates were incubated for 24 h at 37 °C. Finally, the prevention was assessed using the inhibitory zones and the microbial area covered

## **Chapter 3 Nanoparticle Deposition Pattern During Colloidal Droplet Evaporation as *in-situ* Investigated by Low-Field NMR: The Critical Role of Bound Water**

The coating film sector, particularly in agriculture and optical applications, demands homogeneous deposits after drying solutions of diverse compositions on various substrates regularly. This is one of the most serious issues confronting the coating department division in the industrial sector, as inhomogeneous coating results in undesirable attributes and low product quality. As a result, this chapter explored one of the most well-known phenomena, the coffee ring effect, which studied the causes, types, and solutions. The evaporation speed and adding additives to the suspended particles were revealed to substantially impact deposition morphology, which is crucial for future coating technology.

### **3.1 Introduction**

The coating of nanoparticles on solid surfaces derives from its extensive usage in the industry, such as anti-reflective and conductive coatings [102]. Nano-particle layers are made utilizing several techniques, including the evaporation of colloidal droplets [103], dip coating [104], sedimentation [105], electrostatic assembly [106], and convective deposition [107]. Drop evaporation is a valuable method for depositing micro- and nano-particles due to reducing used fluids. The suspended particles within the liquid droplet form a ring as it dries on a solid surface, known as the coffee-ring effect (CRE) [7,8,9]. Coffee-ring formations can be helpful in applications where well-ordered nanopattern pictures are needed, such as jet ink printing [111]. However, it is unsuitable for other applications that require homogeneous distribution of particles on surfaces, such as agricultural films and optical applications [112]. For instance, for greenhouse film (usually low-density polyethylene, LDPE), the nano-particle coating is frequently adopted to increase the wettability of the hydrophobic LDPE surface, where the CRE causes several optical problems due to the aggregation of the nanoparticle. This reduces the hydrophilicity of greenhouse film, resulting in fogging problems that are reflected plainly in crop production [49]. Therefore, understanding the fundamental mechanism of CRE is of great importance for improving coating applications.

Because the liquid evaporation rate  $J$  is quicker near the droplet's edge, the liquid from the droplet's bulk flows outward. It indirectly drags the particles, creating a particle ring along the drop's edge [113]. The mechanism that replenishes the liquid inside the droplet edge is called capillary flow [114]. To suppress CRE, the following three physical strategies are usually adopted: 1) preventing the contact line from pinning, 2)

interrupting the capillary flow towards the contact line, and 3) preventing the capillary flow from delivering particles to droplet edge [115]. The above strategies are developed based on progressing understanding of CRE. For instance, Xiaoying Shen et al. [9] reported that when  $CR > 1$ , the evaporation period is insufficient to create a coffee ring. Nanoparticles are scattered over the surface; when  $CR \leq 1$ , The nanoparticles have enough time to migrate to the contact line and form a monolayer, permitting the creation of a coffee-ring structure. Whereas  $CR = \tau_{particle} / \tau_{evap}$  ( $\tau_{particle}$  shows the time scale for particles near the contact line (CL) to collide, which is crucial for the creation of the first monolayer, and  $\tau_{evap}$  is the time scale for liquid droplet evaporation). Maryam Parsa et al. [116] studied the coffee-ring formation for evaporating copper(II) oxide (CuO) nanoparticles in water droplets on the substrate at different temperatures. They discovered that temperature gradients at the air-fluid interface drive the radial Marangoni flow, inhibiting the deposition of nanoparticles at the edge. In addition, when the substrate temperature rises, the Marangoni thermal number grows. Yuch-Feng Li et al [117] discovered that the evaporation stain pattern, consisting of concentrated stain, a ring-like deposit, and a combined structure, varies depending on solution surface activities and substrate contact angle hysteresis (CAH). The deposition pattern's evolution has also been extensively studied [118,119]. The gradient of surface tension (which typically leads to the Marangoni flow), the J, and the temperature are studied. Despite numerous attempts to clarify the origin of CRE, the molecular level understanding of CRE, especially the interaction between nanoparticle and bulk solvent, or the dynamics gradient on the nanoparticle surface, is still required.

Recently TD NMR has been around for several decades for its multiple uses, such as assessing changes in water state and fractions mobility throughout processing [120]. Also, it could be utilized for other materials such as muscular tissue [121] and food like fruits [122], grains, and vegetables [123]. It is a rapid, non-destructive, and non-invasive method that distinguishes water mobility with minimal pretreatments. Generally, using NMR, water can be classified into three categories based on mobility at atmospheric conditions: bound water, immobilized water, and free water [124][120]. Above three different kinds of water can be detected by the spin-spin relaxation ( $T_2$ ) time through both the  $T_2$  value and its distribution. These three categories were based on  $^1H$  NMR spectra of water, which will be discussed in further depth in the following sections.

Nanoparticles have received tremendous interest because of their excellent chemical and physical characteristics. Silica nanoparticles are flexible materials used in many applications, such as coating [25] and pigmenting [125]. The hydroxyl group ( $-OH$ ) on the silica surface adsorbs moisture and promotes nanoparticle aggregation [126]. The agglomerations lead to an insufficient distribution in the solution state. Such accumulation of silica nanoparticles could result in an inhomogeneous colloidal fluid, which plays a critical role in coffee-ring formation [127]. Several surface modification techniques were developed for silica nanoparticles [29,30,31]. These techniques include modifying the surface of nanoparticles, such as employing polymers or

ionic surfactants to improve electrostatic repulsion between nanoparticles [32,33]. Sugam Kumar et al. [133] studied the effect of the three kinds of surfactants with silica nanoparticles of different sizes using small-angle neutron scattering (SANS). It was discovered that anionic silica nanoparticles interact with nonionic, cationic, and anionic silica nanoparticles. And anionic surfactants are highly diverse, resulting in distinct microstructures in each situation. Therefore, to assist in suppressing the CRE during evaporation in a colloidal droplet of silica nanoparticles, a rapid and straightforward technique for understanding how to prevent the process of their accumulation under predetermined conditions is required.

In this work, we carefully investigated the effect of  $J$  on preventing the formation of the CRE and the critical contribution and essential function of water fractions in understanding the mechanism of this phenomenon. When surfactant and polymer are added to nanoparticles with decreasing  $J$ , the obtained findings indicate the efficient function of bound water forming the highest consistency coating, opening the way for upcoming research in this field.

### 3.2 Results and discussions

#### 3.2.1 Surface modification of silica nanoparticles

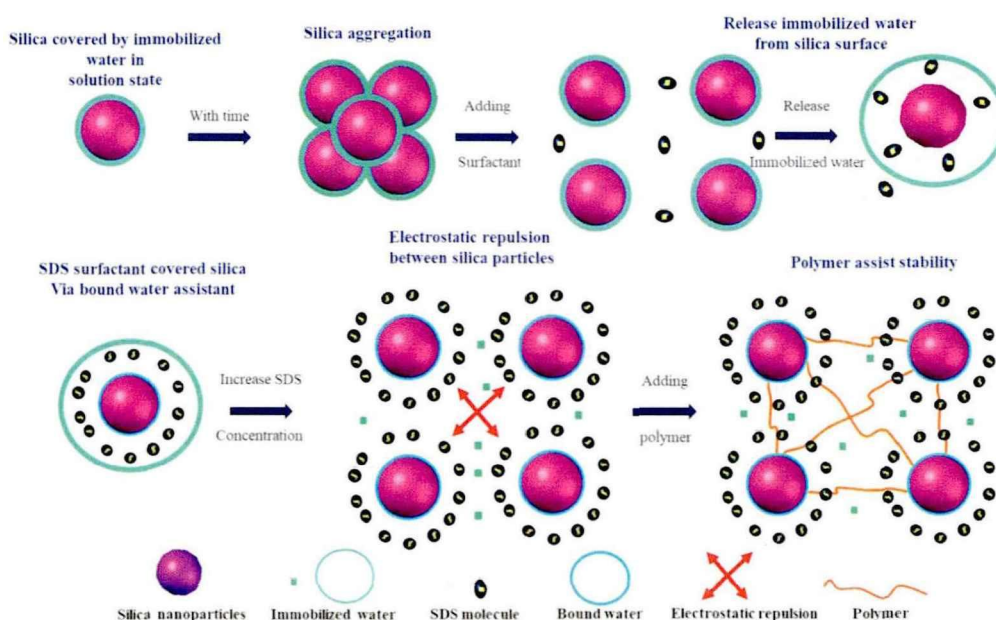


**Fig. 3. 1.** Schematic illustration of surface modification of silica nanoparticles.

The formation of hydrogen bonds between silica nanoparticles causes accumulation when pure silica nanoparticles are added to pure water [134]. To inhibit such aggregation, the surfactant is typically added (i.e., Sodium dodecylsulfate (SDS) with hydrophilic groups (heads) and extended lipophilic hydrocarbon groups

(tails)), where the surface tension of the solution is reduced. This is attributed to the amphiphilic feature of surfactant, as shown in Fig. 3. 1. The hydrophobic tail attaches to the silica surface, whereas the charged hydrophilic one surrounds it [135]. In addition, the presence of Sodium dodecylsulfate (SDS) surfactant in a colloidal solution assists in the homogeneous distribution of silica nanoparticles due to the repulsion force of the charged hydrophilic tail [42,43]. The water-soluble polyvinyl alcohol (PVA) is added to stabilize such distribution further. The addition of PVA significantly increases the viscosity of the solution, which slow down the precipitation process of silica nanoparticle.

### 3.2.2 Influence of evaporation rate on CRE

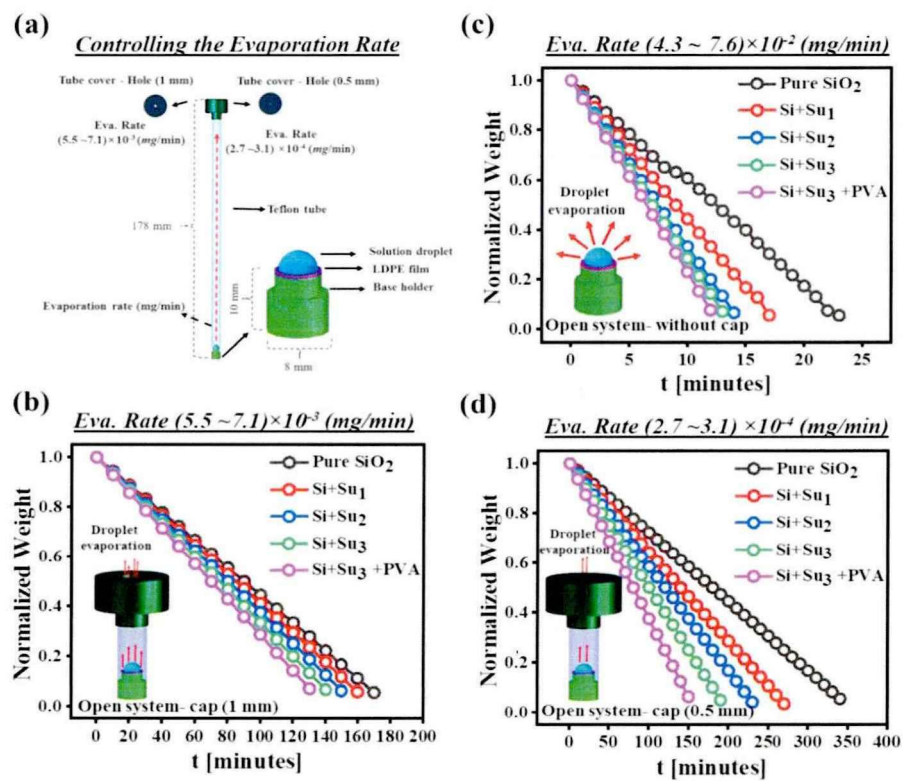


**Fig. 3. 2.** Weight loss according to evaporation rate  $J$ , (a) NMR experiment setup, (c) weight loss of solutions droplet for the system without caps at the ambient environment in the  $J = 4.3 \sim 7.6 \times 10^{-2}$  mg/min, (b) system with a cap hole size of 1mm,  $J = 5.5 \sim 7.1 \times 10^{-3}$  mg/min, (d) system with a cap hole size of 0.5mm,  $J = 2.7 \sim 3.1 \times 10^{-4}$  mg/min, All the above experiments were conducted at the same temperature (23 °C) and humidity (75 %).

The droplets with the addition of surfactant or polymer are inadequate to produce a uniform distribution of silica nanoparticles and avoidance of the coffee-ring formation on the LDPE film surface in the ambient environment. As a result, more tests for regulating evaporation rate  $J$  were conducted to investigate the

influence of the  $J$  on CRE formation. Here, three experiments were adopted, where  $J$  is controlled by combining the addition of surfactant /PVA and the hole size in the cap. Then a droplet of solution with a volume size of  $1 \mu\text{L}$  is laid on the LDPE surface, whose weight is used to monitor the  $J$  as shown in Fig. 3. 2a. All experiments were performed in the same environmental conditions (temperature  $23 \text{ }^\circ\text{C}$ , humidity 75%). For a system without a cap, the experiments took less than 25 min for all samples to evaporate entirely, with the  $J$  of  $4.3 \sim 7.6 \times 10^{-2} \text{ mg/min}$  depending on surfactant concentrations and polymer additives (Fig. 3. 2c). It's worth noting that the  $J$  of samples with the highest concentration of surfactant and PVA is the highest. For systems with caps, samples were placed in Teflon tubes (1mm and 0.5mm cap holes, respectively). The rate of evaporation  $J$  was detected between  $5.5 \sim 7.1 \times 10^{-3} \text{ mg/min}$ , requiring more than 200 min for all samples to evaporate completely (Fig. 3. 2b), and less than 350 min when  $J$  is reduced to  $2.7 \sim 3.1 \times 10^{-4} \text{ mg/min}$  (Fig. 3. 2d).

### 3.2.3 Surface morphology

The effects of evaporation speed on the final distribution of silica nanoparticles have been detected using optical microscopy (OM). When a colloidal droplet of silica nanoparticles is placed on a hydrophobic LDPE surface in a system without a cap, the formation of the coffee ring is evident, as shown in Fig. 3. 3(a1). During evaporation, the nanoparticles firstly deposit and aggregate at the edges due to the capillary flow [108]. The CRE is significantly suppressed with the increasing surfactant addition and PVA (Fig. 3. 3(a2, a3, a4, and a5)). The silica begins to form a multi-layer and gradually decreases in the direction of the droplet center, with a scattered distribution rather than accumulating at the contact line (Fig. 3. 3(a3)). This refers to the disturbance in capillary flow when Sodium dodecylsulfate (SDS) surfactant is added. Such disruption is proportional to surfactant concentration and reduces agglomeration layers to monolayers (Fig. 3. 3(a4)). In addition, the completely receding of the coffee ring with scatter aggregations was done when PVA was introduced (Fig. 3. 3(a5)). For more homogeneous distributions,  $J$  was reduced to the range of  $5.5 \sim 7.1 \times 10^{-3} \text{ mg/min}$ . In the case of pure silica droplets, the appearance of CRE was decreased, with a bit of dispersion (Fig. 3. 3(b1)). The formation of nanoparticle multi-layers is significantly reduced when the dose of Sodium dodecylsulfate (SDS) surfactant is raised from 0.5 to 1%. Following that, due to reductions in contact angle and silica separation from each other, a silica monolayer continues to form extensively (Fig. 3. 3(b1, b2, b3, and b4)), and after adding PVA (Fig. 3. 3(b5)). When  $J$  is lowered to  $2.7 \sim 3.1 \times 10^{-4} \text{ mg/min}$ , the pure silica droplet shows obvious retreating of the coffee ring with aggregation toward the droplet center (Fig. 3. 3(c1)). From the first presence of Sodium dodecylsulfate (SDS) surfactant, this buildup tends to diminish, and the region of uniform dispersion rises (Fig 3. 3(c2)). The homogeneity distribution steadily increased with surfactant concentration (Fig. 3. 3(c3



& c4)). When the PVA polymer was added, the area attained maximum distribution, limiting the number of voids that the silica didn't reach and covering the largest possible area (Fig. 3. 3(c5)).

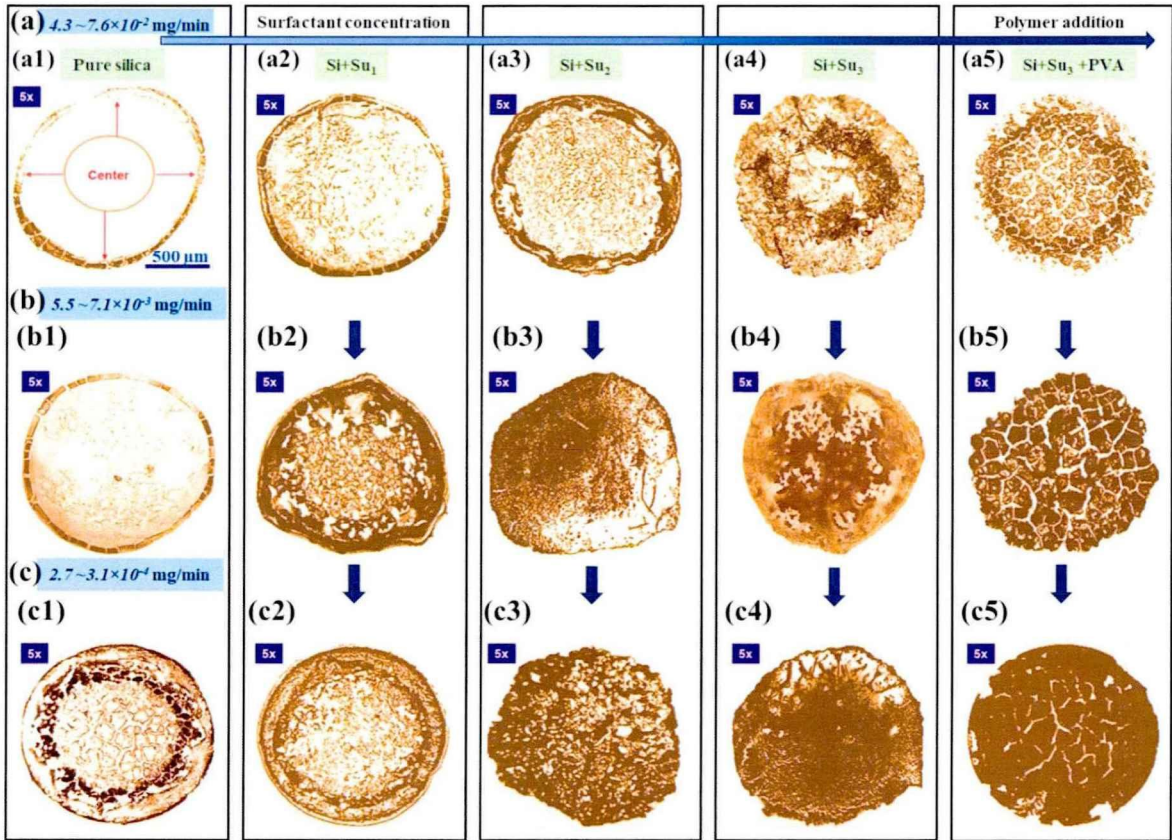


**Fig. 3. 3.** Optical microscopy images clarify suppression of the CRE. (a) Evaporation rate  $J = 4.3 \sim 7.6 \times 10^{-2}$  mg/min, (b)  $J = 5.5 \sim 7.1 \times 10^{-3}$  mg/min, (c)  $J = 2.7 \sim 3.1 \times 10^{-4}$  mg/min. (a1, a2, a3, a4), (b1, b2, b3, b4), (c1, c2, c3, c4) the distribution of silica nanoparticles on hydrophobic LDPE surface in different surfactant concentration (0%, 0.1%, 0.5%, 1%) with different  $J$  (a, b, c) respectively. (a5, b5, c5) the addition of (0.25%) PVA polymer to (Si+Su3) sample in different  $J$  (a, b, c) respectively.

For quantifying CRE, the ratio of the area covered by silica after evaporation  $S$  and that of original droplet  $S_0$  ( $S/S_0$ ) is calculated as shown in Fig. 3. 4. The ratio  $S/S_0$  is 21% for the pure silica droplet in the system without caps in an ambient environment. With decreasing the evaporation rate  $J$  to  $5.5 \sim 7.1 \times 10^{-3}$  mg/min, the recorded covered area was 37%, till it reached 55% at the lowest evaporation rate. Taking the  $J = 2.7 \sim 3.1 \times 10^{-4}$  mg/min as an example, the area covered by silica distribution increased from 55% to 83% when Sodium dodecylsulfate (SDS) concentration raised from 0.1% to 1%, respectively. After adding (0.25%) PVA polymer, the area reached the maximum distribution of 95%. The area region for uniform silica distribution in

the case of low evaporation speed demonstrates the evident necessity of controlling evaporation conditions during the coating process, which primarily influences CRE suppression. The experiment findings indicated that the covered area ( $S/S_0$ )  $\leq 60\%$  indicates a high probability of accumulations in the droplet edge of varying sizes. The ring size in Fig. 3. 5a and the finite distance in Fig. 43. 5b show additional information about the effect of the critical additives and evaporation rate ( $J$ ).

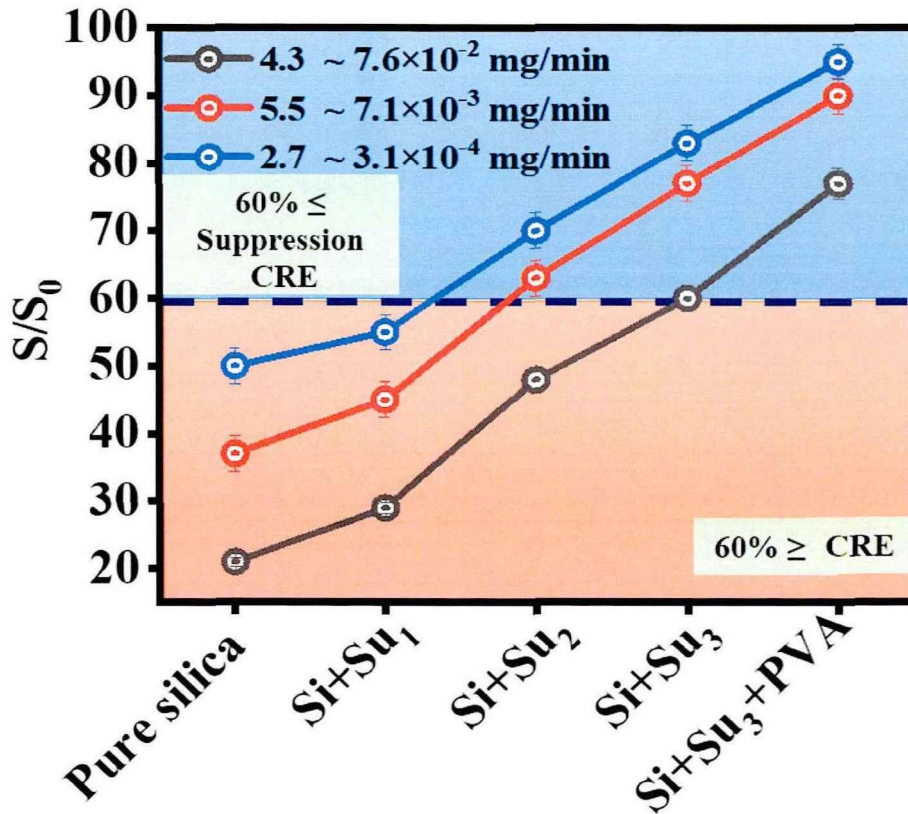


**Fig. 3. 4.** Effect of evaporation rate  $J$  on final silica distribution on LDPE surface in the presence of surfactant and polymer.

The diameter of the coffee ring steadily decreases when PVA and surfactant concentrations are introduced with a lowering Eva. Rate until it approaches a diameter near-zero (Fig. 3. 5a). This is because the particles have ample time to settle on the surface without migrating to the edge, inhibiting capillary flow and allowing more significant silica dispersion during evaporation.

A restricted distance ( $L_p$ ), on a few micrometres, was also found between the original contact line and the ring structure boundary (Fig. 3. 5b), which was dubbed finite distance [137]. We used the prior work



approach to calculate limited distances and investigate the influence of  $J$  on the pinning contact line [115]. Depending on the contact angle, eq.2 described the method.

$$L_p = r / \tan(\theta/2) \tag{2}$$

where  $r$  is the radius of the nanoparticles and  $\theta$  is the three-phase CL's local contact angle.

The finite distance for all samples was recorded between 0.5 to 0  $\mu\text{m}$ , which revealed that evaporation speed significantly impacts the finite distance. When  $J$  decreases, the finite distance reduces even for pure silica droplets, suggesting that the depositing of silica nanoparticles as monolayers starting from the contact line and Droplet evaporation is quicker than spreading towards the center. As the surfactant concentration grew, so did the dispersion of silica nanoparticles from the contact line to the center. The distance limit diminishes completely when the slowest evaporation speed is employed in the presence of surfactant and polymer.

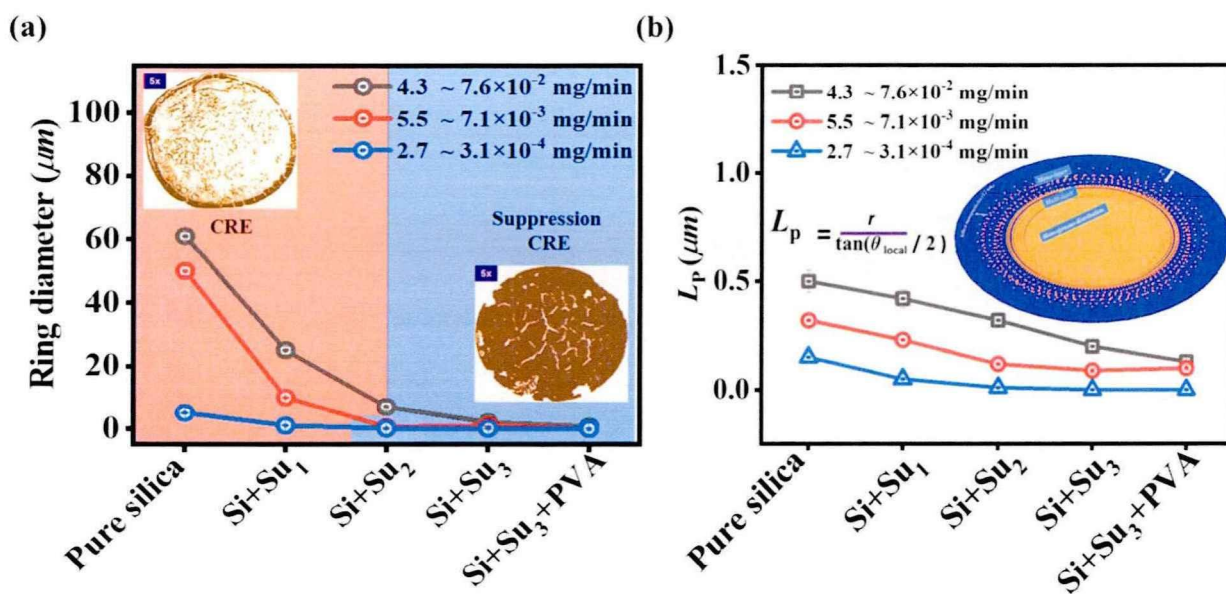
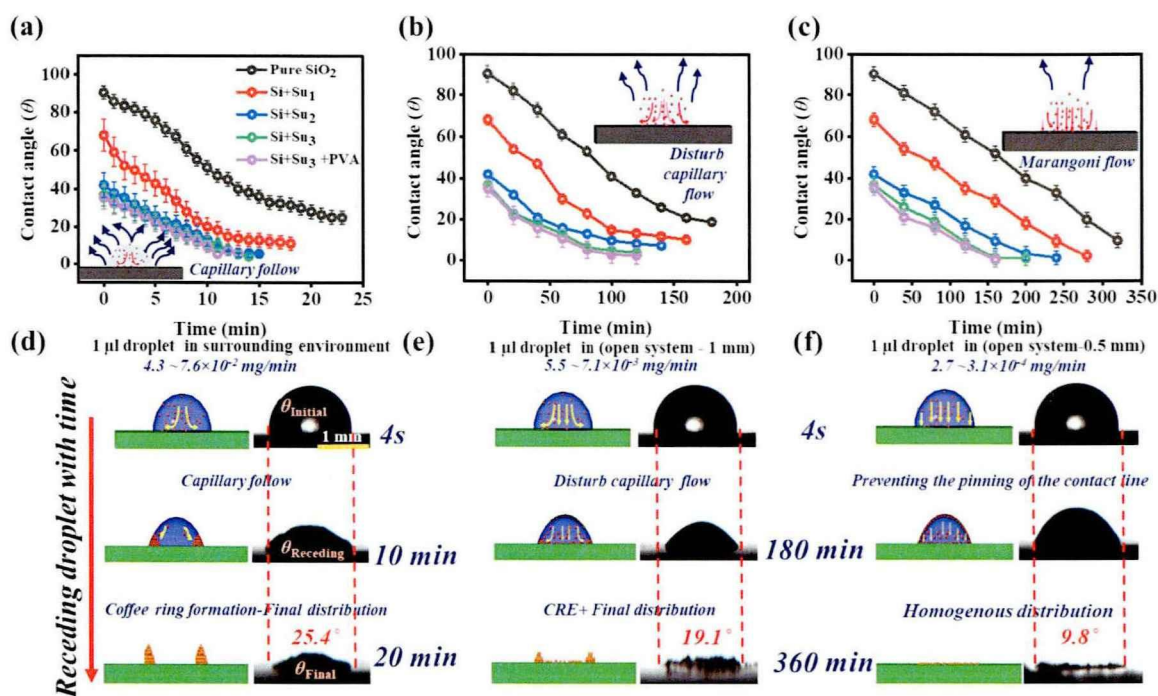


Fig. 3. 5. (a) ring size, (b) existence of a limited distance  $L_p$ , between the original pinning point and the coffee-ring border.

### 3.2.4 Wettability

Contact angle over time was measured for sample droplets with and without additives to investigate the CRE were shown in Fig. 3. 6. The contact angle for colloidal droplets was observed at varying degrees following the final distribution depending on the addition of surfactant concentrations and  $J$ . The final distribution of silica nanoparticles in an ambient environment was detected between 25.4°~ 6.3° (Fig. 3. 6a).

When the evaporation rate ( $J$ ) reduces in the open system from 1mm to 0.5mm, the final contact angle decreased consistently from  $19.1^\circ$  to  $2.5^\circ$  (Fig. 3. 6b), and from  $9.8^\circ$  to  $0.2^\circ$  (Fig. 3. 6c) respectively. For a better understanding of silica particle's motion inside the droplets during evaporation, the contact angle is divided into three essential tenses: initial contact angle, which is detected during the first stage of evaporation  $\theta_{\text{initial}}$ , receding contact angle, which is the most critical time for silica formation on the surface  $\theta_{\text{receding}}$ , and final contact angle, which represents the angle of silica distribution after fully evaporate  $\theta_{\text{final}}$  [110]. Using pure silica droplet as an example, the contact angle during evaporation with different evaporation speeds is shown in Fig. 3. 6(d, e, and f). In the case of rapid evaporation ( $J= 4.3 \sim 7.6 \times 10^{-2} \text{ mg/min}$ ), silica particles begin to take shape toward the edge, induced by capillary flow during the receding stage (less than 15 min), and ending in the final stage in a shape of a coffee ring, as a result of rapid evaporation from the edge with a contact angle more than  $25^\circ$  (Fig. 3. 6d).



**Fig. 3. 6.** Contact angle for varying evaporation rate  $J$  as a function of surfactant concentration and polymer in (a) ambient environment in the  $J= 4.3 \sim 7.6 \times 10^{-2} \text{ mg/min}$ . (b) open system-1mm,  $J= 5.5 \sim 7.1 \times 10^{-3} \text{ mg/min}$ , (c) open system-0.5mm,  $J= 2.7 \sim 3.1 \times 10^{-4} \text{ mg/min}$ . Sketches of particle migration (left) and contact angle images (right) during sessile pure silica drop drying at (d) open system-ambient environment, (e) open system-1mm, (f) open system-0.5mm. All contact angle pictures taken at 1 mm scale.

When  $J$  is reduced to  $5.5 \sim 7.1 \times 10^{-3} \text{ mg/min}$ , the contact angle has a low receding angle speed (more than 70 min). This provided extra time for more silica dispersion, decreasing the accumulation at the edge by enhancing

Marangoni flow, which reflected the final contact angle by less than  $19.1^\circ$  (Fig. 3. 6e). The impact of Marangoni flow increased when  $J$  was lowered to  $2.7 \sim 3.1 \times 10^{-4} \text{ mg/min}$ , allowing the particles to settle more uniformly from the droplet's contact line to the center (receding contact angle more than 100 min), and the contact angle decreased to  $9.8^\circ$  (Fig. 3. 6f).

### 3.2.5 Evolution of three-state water

#### 3.2.5.1 Solution state

Water has a high surface tension due to the strong hydrogen bonding between water molecules [138]. When surfactants are introduced, they will penetrate the air-water contact and disrupt those bindings, reducing the surface tension [139].

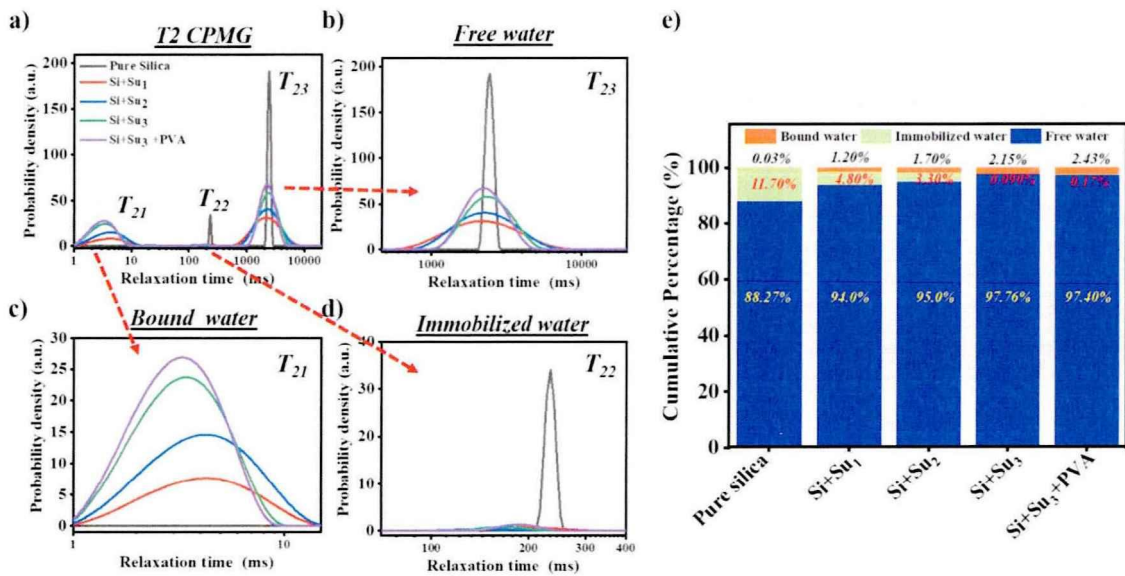


**Fig. 3. 7.** Relaxation time distributions in the presence of other additions. (a)  $T_2$  CPMG after ILT where three different distinct  $T_2$  are observed, together with enlarged pictures for (b) free water, (c) bound water, and (d) trapped water, respectively. (e) the proportion of different water fractions under various additions.

The influence of surfactant, PVA, and silica nanoparticles on the distribution of three different kinds of water is reflected by NMR  $T_2$  relaxometry obtained by CPMG sequence as shown in Fig. 3. 7a, where the ILT is used for a serial of echoes. For pure water, the singlet peak appears in the time range 300-10000 ms, referred to as free water (Fig. 3. 7b) [140]. When silica nanoparticles are added to pure water, an interfacial hydrogen bond is formed between particles [141,134], known as trapped water, between 100-300 ms (Fig. 3. 7d). This intermediate bond helps particles stick to each other and form colonies of silica aggregations, affecting the stability of silica distribution and accelerating deposition. Due to the surfactant activity in breaking the

hydrogen bonds established between particles, the intensity of trapped water begins to diminish as Sodium dodecylsulfate (SDS) is added to the solution (Fig. 3. 7d). And it practically vanishes when the concentration reaches 1%, ranging from 11.7% to 0.09%, signalling for disintegrating silica colonials (Fig. 3. 7e)

The number of surfactant molecules firmly attached to silica particles (bound water) appeared in the time range 1–10 *ms*, increasing gradually with surfactant content, as shown in Fig. 3. 7c. The fraction of bound water rises from 0.03% to 2.15%, implying that it refers to the number of surfactant molecules attached on silica surfaces, enhancing electrostatic repulsion between silica particles and preventing aggregation (Fig. 3. 7e). The proportion of bound water fraction increased to 2.43% after adding PVA (0.25%) to the solution consisting of surfactant and silica nanoparticles. This refers to two reasons: 1) PVA has entire hydrophilic groups, such as -OH hydrogen bonding formation groups [142]; 2) the polymer promoted silica particle attachment and stability in solution by strong binding (bound water) with maintaining silica surfaces covered by surfactant. The free water fraction rose continuously with the surfactant dose, from 88.27% to a high of 97.4%, due to the ability of Sodium dodecylsulfate (SDS) surfactant to dissolve the hydrogen bond (trapped water) between silica particles and convert it to free water.

### 3.2.5.2 *In-situ* NMR tracking

*In-situ* studies have been conducted using NMR CPMG to investigate the change in water fractions in the presence of silica nanoparticles and other substances during evaporation. 1  $\mu\text{L}$  of the various colloidal droplet was placed on the hydrophobic LDPE film separately, and then the on-site NMR follow-up started with time during evaporation. According to the optimum scans 128 and RD 20s, each signal was accumulated by 40 min. Fig. 3. 8(a1 and b1) displayed the original  $^1\text{H}$  FID signal for pure silica and Si+Su<sub>3</sub>+PVA droplet, respectively, which has subsequently been transformed to numerous peaks by ILT (Fig. 3. 8(a2 and b2)). The original data was then utilized in a fitting process to determine the cumulative percentage for each fraction throughout evaporation (Fig. 3. 8(a3 and b3)). Experimentally, found that bound water fractions always occur in the initial stage of evaporation for all colloidal droplets, including the droplet of pure silica in an ambient environment, which may be attributable to the contact line on the LDPE surface being pinned by a strong hydrogen bond. Influential additions and the evaporation rate determine the rise and reduction of this bond and its continuity. To clarify the variations in water fractions in each case during evaporation, a droplet of pure silica was compared to a droplet containing surfactant and polymer (Si+Su<sub>3</sub>+PVA) at the same  $J$  ( $5.5 \sim 7.1 \times 10^{-3} \text{ mg/min}$ ). In the case of pure silica droplets, the free water fraction gradually decreased over time due to their high mobility. This effect is explained because free water populations will evaporate first from droplets [143]. The proportion of trapped water was lower at the beginning and rose to its maximum at the end of drying. (Fig. 3. 8(a2)). This is due to the hydrogen bonds being raised between silica particles, translating as trapped water in



the NMR signals according to the time range (70-300 ms). During drying, the loss of bound water fractions continuously after the first stage, due to edge evaporation (Fig. 3. 8(a3)).

Furthermore, the fractions of trapped water rose continually, suggesting a continuous transfer of silica conglomerates onto the contact line by capillary flow. And replacement of the bound water fraction created for pinning contact lines by trapped water increased considerably owing to the ongoing attraction of silica particles for each other during evaporation. Conversely, the bound and trapped water fractions of colloidal droplet Si+Su<sub>3</sub>+PVA progressively rose till the end of the evaporation process, whereas the free water fractions gradually dropped (Fig. 3. 8(b3)).

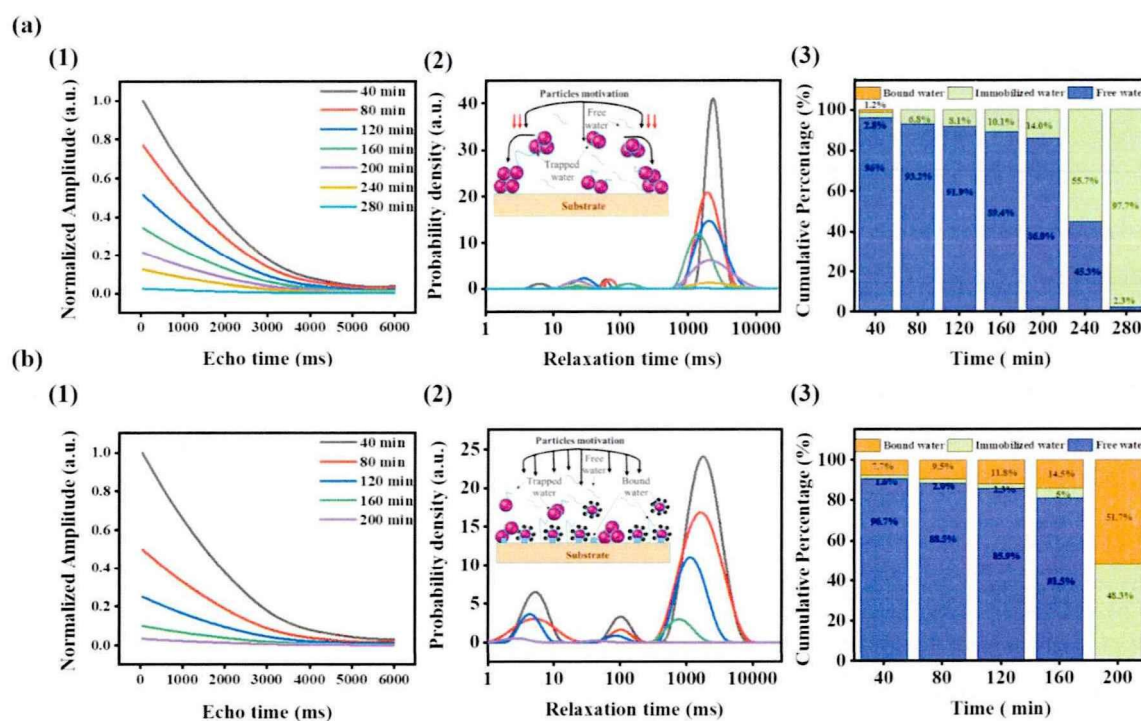


**Fig. 3. 8.** The relaxation time distribution of different water fractions over time in the presence of surfactant and polymer concentrations. (a) & (b)  $T_2$  CPMG for pure silica and (Si+Su<sub>3</sub>+PVA) solution droplet respectively, at the same evaporation speed  $5.5 \sim 7.1 \times 10^{-3}$  mg/min. (a1, b1)  $T_2$  CPMG original signals for amplitude droplets decreasing with time, (a2, b2) ILT and, (a3, b3) proportion of water fractions during evaporation for pure silica droplet and (Si+Su<sub>3</sub>+PVA) solution droplets respectively.

In contrast to the droplet of pure silica, the proportion of trapped water is relatively small in the initial state, indicating decreased attraction between silica particles due to the surfactant effect. Over time, the modest increase in trapped water percentage is attributable to aggregation during evaporation. This is to say, the tiny quantity of accumulation has no effect on the enormous covered area by silica nanoparticles (90%), as seen in Fig. 3. 8(b3). In the Si+Su<sub>3</sub>+PVA droplet, the proportion of bound water fraction began with three essential

variables influencing its intensity: 1. bound water covered silica nanoparticles owing to surfactant effect, 2. bound water attributable to the PVA polymer structure, and 3. bound water anchoring the contact line. Moreover, the bound water percentages increase with time due to the pinning of silica particles on the LDPE surface, suggesting the broad distribution area covered by silica. Decreasing  $J = 2.7 \sim 3.1 \times 10^{-4} \text{ mg/min}$  significantly impacted the droplet fractions, which started with a short relaxation time (bound water) and evolved to a lengthy relaxation period (free water) (Fig. 3. 9). The proportion of bound water required a long time to completely disappear in the case of pure silica droplets (Fig. 3. 9(a2)) (Support Information), indicating a deficit in evaporation at the droplet edge. This keeps the contact line open for a more extended period and prevents capillary flow from the droplet center to the edge, enabling particles to descend through Marangoni flow rather than gather at the border.

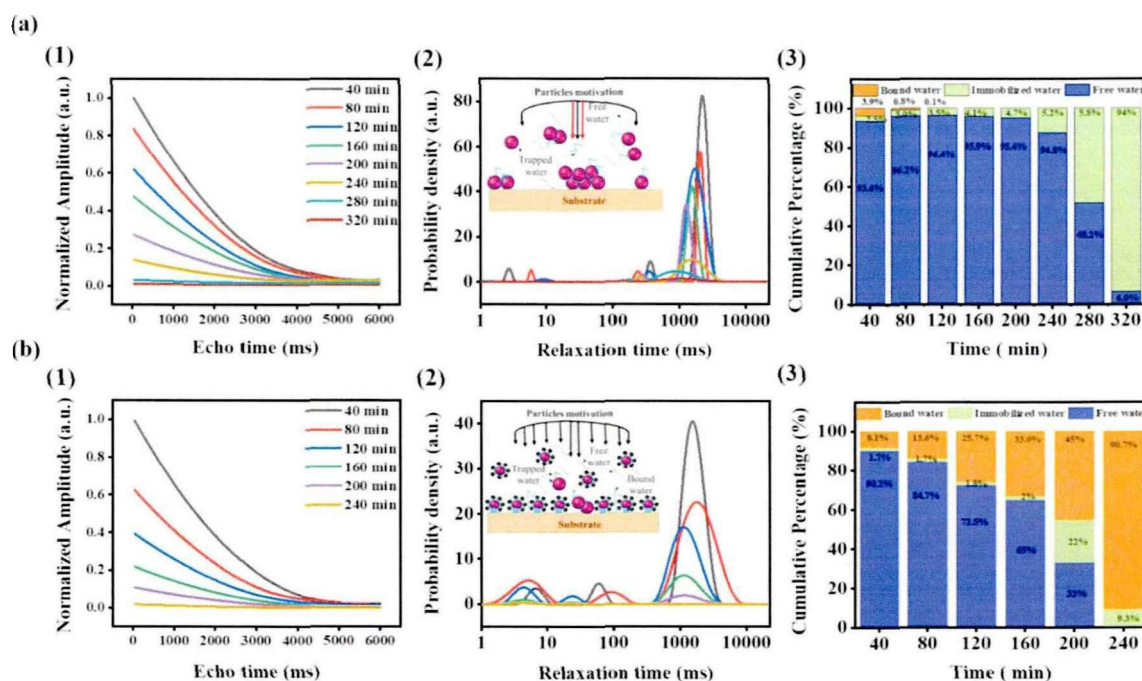


**Fig. 3. 9.** Relaxation time distributions investigated the changes in water fractions over time in the presence of surfactant and polymer concentrations. (a) & (b)  $T_2$  CPMG for pure silica and (Si+Su3+PVA) solution droplet respectively at the same  $J = 2.7 \sim 3.1 \times 10^{-4} \text{ mg/min}$ . (a1, b1)  $T_2$  CPMG original signals for decreasing droplets with time, (a2, b2) the corresponding  $T_2$  distribution after ILT and (a3, b3) proportion of water fractions during evaporation for pure silica droplet and (Si+Su3+PVA) solution droplets, respectively.

A slight increase in the trapped water proportion during evaporation (Fig. 3. 9(a3)) due to the accumulation of silica nanoparticles in the middle of the droplet (Fig. 3. 3(c1)). In Fig. 3. 9 (b2, b3), due to the bound water in the PVA structure, which is generally determined by its polarity and ionic group concentration [144], the bound water effect increased slightly in the first stage comparison with the droplet without additives.

The proportion of bound water fraction increases with time due to the wide-area deposition of modified silica nanoparticles during evaporation pinned to the LDPE surface (Fig. 3. 9(b3)). Several studies on colloidal droplets have been done to determine the optimum conditions to regulate the formation of coffee rings based on the time of particles movement inside the droplets. In addition, Table 3. 1 compares critical characteristics between our study and other previous findings based on the time scale for particle migration during evaporation to determine different CRE suppression methods (support information). As an instance, Min Pack et al. [145] reported that when  $t_P/t_{EI} < 1$ , the coffee-ring will form or be inhibited if the ratio is  $t_P/t_{EI} > 1$  (where  $t_P$  is the time required for particles to reach the contact line and  $t_{EI}$  is the time needed for the residual drop volume to evaporate).

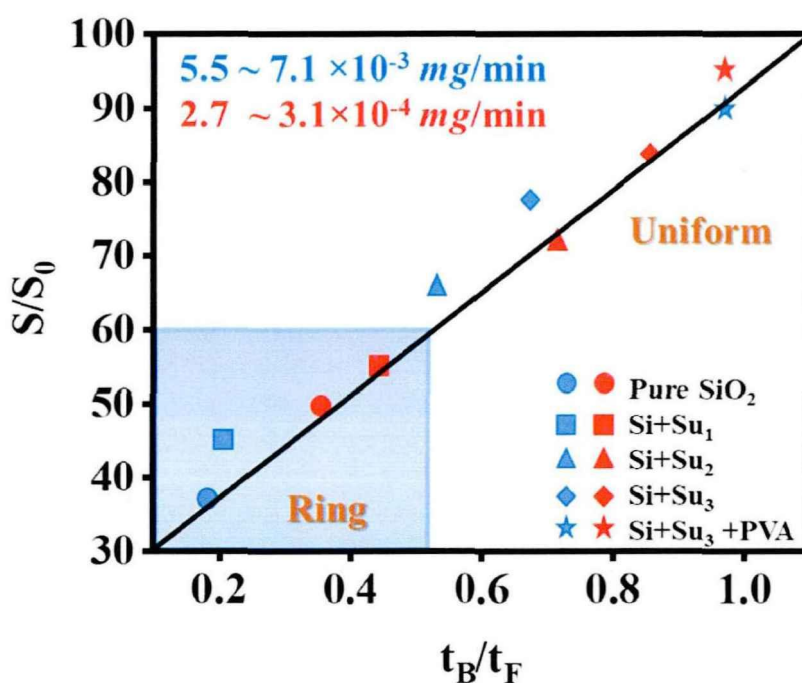


**Fig. 3. 10.** The time spent on bound water fraction during the colloidal droplets' evaporation is normalized by the time of all fractions for fully evaporation  $t_B/t_F$  as a function of the area covered by silica distribution  $S/S_0$ .

The current study shows the duration of the existence of bound water fraction at different evaporation speeds and silica distribution after total evaporation in Fig. 3. 10. Where  $t_B$  is the time scale relevant to the movement and adhesion of the nanoparticles to the surface by particle-surface interaction via bound water fraction. It can also be defined as the total time of the bound water fraction to bind nanoparticles to the surface during evaporation. And this could be a quick indicator for the nanoparticle number that has stuck to the surface without aggregating. In the second time scale,  $t_F$  is governed by the evaporation rate. It is related to the recorded time spent on all water components (bound, trapped, and free water) throughout the droplet volume reduction

until complete evaporation. Such results reveal that the longer the presence of bound water during evaporation, the greater the dispersion of silica nanoparticles will be. This is due to the poor mobility of bound water resulting from significant contact with the LDPE surface, which is critical for defining the final deposition morphology in the conflict between particle motion to the contact line and solvent evaporation. Results show that  $t_B/t_F \geq 0.5$  is the minimum requirement for the bound water fractions during evaporation with covered area  $S/S_0 \geq 60\%$ . There was a halt to gather particles at the edge and prevent

the formation of the coffee ring. It is also worthy to note that the higher the surfactant concentration, the more extended presence of the bound water until it reaches the longest time when the polymer is introduced. For  $t_B/t_F \leq 0.5$ , particle deposition in the contact line is predicted to dominate. Therefore, the coffee-ring deposit is expected.

**Table 3. 1.** The comparison of key parameters between our work and other previous reports.

Time scale	Coffee ring effect	Suppression coffee ring effect	Ref
$\tau_r/\tau_d$	$> 1$	$< 1$	[146]
$\tau_{particle}/\tau_{evap}$	$\leq 1$	$> 1$	[110]
$t_P/t_{EI}$	$< 1$	$> 1$	[145]
$t_{off}/t_{\pi}$	$< 0.6$	$0.5 - 0.8$	[147]
$t_B/t_F$	$\leq 0.5$	$\geq 0.5$	<b>Our work</b>

- $\tau_d$  the characteristic deposition time.
- $\tau_r$  is governed by the drop's evaporation flux and is proportional to the volume change necessary to lower the sessile drop's contact angle from its equilibrium value to the receding contact line.
- $\tau_{evap}$  indicates the time scale for liquid droplet evaporation.
- $\tau_{particle}$  represents the time scale for particles close to the CL to collide.
- $t_P$  the time for particle motion.
- $t_{EI}$  evaporation time of the residual drop volume.



- $t_{\text{fl}}$  is the overall evaporation period after being subjected to the laser.
- $t_{\text{off}}$  a droplet is irradiated by a laser beam for a specific time.
- $t_F$  is time for fully colloidal droplet evaporation.
- $t_B$  is the time spent on bound water during evaporation.

### 3.3 Conclusion

The experimental and analytical data presented above demonstrated that depending on functional additives and evaporation rate ( $J$ ), bound water and other fractions play a critical role in forming coffee rings or homogeneous distribution of colloidal droplets during evaporation. Using time-domain low field  $^1\text{H}$  NMR spectroscopy, the spin-spin relaxation time  $T_2$  sequence approach [50] was used to *in-situ* track colloidal silica nanoparticles droplets to understand the effect of evaporation rate ( $J$ ) and effective additives on the performance of water fractions during evaporation. The result shows that owing to its fast mobility and rapid evaporation, the influence of free water fraction during evaporation is relatively modest [120]. The final distribution of colloidal silica droplets is substantially influenced by trapped water in the solution state. A significant influence on silica behavior during evaporation was observed due to the high bonding for water-water and water-surface interactions; it increased silica particle accumulation with a bit of spread [134][141]. On the other hand, the extended life of bound water during evaporation is critical for inhibiting CRE and the ultimate dispersal of the nanoparticles. Because of the strong water-surface interaction and the poor water-water contact, bound water has a major impact during evaporation, significantly separating silica aggregation and organizing particle mobility in colloidal droplets [148]. Experimentally, the minimum time necessary for existence bound water during evaporation to suppress the CRE is  $t_B/t_F \geq 0.5$  with a minimum distribution area  $S/S_0 \geq 60\%$ . This is similar to what has been documented in previous research with different time scales [147,115,146,149,145,110]. This might be used as a dimensionless indicator to examine particle mobility in solution and during evaporation for enhancing silica dispersion throughout the coating process, allowing researchers to more appropriately and accurately determine the appropriate values for adding additives and the best evaporation conditions

## **Chapter 4 Polyvinyl Alcohol (PVA) Based Super-Hydrophilic Anti-Fogging Layer Assisted by Plasma Spraying for Low-Density Polyethylene (LDPE) Greenhouse Films**

After studying the formation of the coffee ring effect, which affected the coating homogeneity, and finding a possible solution by decreasing the evaporation speed and adding additives such as PVA polymer, the coating process applied for the LDPE to solve the antifogging properties will discuss in this section. Fogging is an issue that occurs in various applications, including food packaging and condensation within greenhouse complexes. Food packaging must exhibit its contents in a sanitary and visually pleasing manner, which decreases the consumer's ability to view the food and gives the impression of inferior quality. Condensation of water within the container may result in a deterioration in quality in particular situations. Unwanted impacts in the agricultural sector include lower total light transmission in greenhouses and water dripping, which can cause plant damage. The focusing action of the water droplets - similar to an array of lenses concentrating solar radiation on plants - may cause additional plant harm. These factors result in a decreased potential yield and worse product quality for food producers. This chapter will concentrate on a solution to the fogging problem in greenhouse applications by employing a super-hydrophilic layer using environmentally friendly components with a long shelf-life.

### **4.1. Introduction**

The greenhouse film plays a vital role in increasing agriculture yield by providing a suitable crop environment. Due to its excellent mechanical and optical properties and low price, polyethylene (PE) has become the primary petroleum-based polymer for producing greenhouses films [150]. In the early 1970s, low-density polyethylene (LDPE) started to replace the paper for mulching vegetables [151], followed by large-scale applications, i.e., greenhouses and tunnels [152][150]. But one serious disadvantage of PE-based greenhouse film is the hydrophobicity due to its low surface free energy ( $\sim 30$  dynes/cm) [153]. This leads to the fogging phenomenon's un-favored effect since the water has a much higher surface free energy of  $\sim 70$  dynes/cm, and the droplets cant spread on the surface [153]. Fogging phenomena would affect the critical properties of the required film, such as reducing transmittance [95] and forming water droplets on the film surface, which act as lenses, resulting in the burning of crops and eventually reducing crop yield [154]. Undoubtedly, methods to solve the antifogging problem of PE agriculture film are required at first glance.

Generally, two strategies have been adopted for antifogging: internal migratory additives and external topical coatings [155]. The internal additive strategy depends on the migration of additives on the film surface

to reduce the surface tension. Commonly used additives are fatty acid esters, i.e., monoglyceride and polyglycerol ester, with a weight concentration of (0.2-3 wt.%) [90]. The polar part of the internal additive leads to incompatibility with PE films, causing micro-phase separation during processing [156]. With the progress of multilayer greenhouse films, controlling the migration and ensuring long shelf life becomes a challenge for the internal additive strategy. The external coating is another efficient strategy to reduce surface tension [153]. The layer is usually achieved through plasma treatment [157], layer by layer (LbL) [158], and roller process [159]. Plasma treatment activates the PE film's surface, enhancing the interaction between PE film and additives [160]. The plasma discharge method has been widely utilized to change the characters of plastic films by creating surfaces rich in carboxyl groups induced by plasma polymerization [161]. The degree of surface oxidation and film surface tension increased with increasing electrode influx of corona-discharge treatment [162]. The main disadvantage of this approach is that the surface free energy of the treated film is still low and does not fulfill antifogging requirements.

On the other hand, after plasma treatment, polar groups on the surface re-arrange themselves with time, reducing surface wettability during storage [163]. A later solution casting process could overcome such drawbacks. For solution casting, some nanoparticles, like  $\text{Al}_2\text{O}_3$  and  $\text{SiO}_2$ , are added to the surface of the films to enhance several properties, i.e., wettability and durability [106,107]. Surfactants are usually added as antifogging agents to increase surface energy and inhibit the aggregation of nanoparticles [108,109]. Since external strategy only deals with the outmost layer, multilayer films show great versatility. However, compared with the internal strategy, where the migration process is relatively slow and controllable, the stability of the external coating layer significantly influences the shelf life of the greenhouse film [167].

A new strategy related to the external coating is required to keep the versatility of the traditional external coating strategy and overcome its weakness in severe fogging conditions. Recently, researchers figured out that adding polyvinyl alcohol (PVA)/ $\text{SiO}_2$  blend as a coating agent gives significant efficiency in decreasing contact angle combined with anti-fogging properties [168]. PVA has been widely used in the biomedical field [169], optical [170], and textile applications [171], etc. As a hydrophilic polymer, PVA could reduce the surface tension. Meanwhile, the high transmittance of PVA ensures a relatively minor influence on lowering the optical properties of greenhouse film. However, its water solubility limits its application in greenhouse film. The addition of silica nanoparticles is necessary, as the outermost silica layer's existence could significantly increase resistance to fogging, soiling, and thermal stability [172]. For instance, Wu et al. [173] prepared a durable anti-fogging coating by forming a Si-O-C chemical bond between PVA and silica nanoparticles to improve water resistance and strength of the coating layer. Considering the antifogging application in the agricultural greenhouse, low cost but highly efficient and with a long shelf-life anti-fogging layer is required.

In this work, based on the traditional external coating strategy, a new anti-fogging coating strategy including PVA polymer network as the basis with silica nanoparticles and surfactant was developed. Three kinds of nonionic surfactants and Tris-buffered saline (TBS) were used to enhance interaction between coating and PE films, which improves the shelf life of greenhouses films. TBS is a biochemical substance commonly employed in several biochemical procedures to keep the pH within a reasonably limited range (7-9.2) and improve surfactant use efficiency [174]. The obtained film shows an excellent anti-fogging effect, with a contact angle  $< 2^\circ$ . The hot fog tests confirm the long shelf life of this kind of functionalized greenhouse film.

## 4.2 Results and discussion

The plasma treatment was performed on LDPE films to generate carbon radicals from the hydrocarbon backbone to generate reactive sites. The unstable hydroperoxides are caused by rapid oxidization. The decomposition of hydroperoxide then produces various oxygen-based functional groups [175]. The influence of plasma power and rolling speed on surface wettability, determined by contact angle measurements, was first checked to determine optimum conditions for high adhesion quality without affecting the LDPE interior structure.

### 4.2.1 Surface wettability

The contact angle is typically regarded as a strong predictor of changes in surface wettability. As shown in Fig. 4. 1a, the higher power and slower rolling rate result in a smaller contact angle. Taking the rolling rate of 15 mm/s as an example, compared with the untreated LDPE with a contact angle of  $\theta = 110^\circ$ , the  $\theta$  of treated LDPE decreases continuously from  $110^\circ$  to  $47^\circ$  with increasing plasma power.

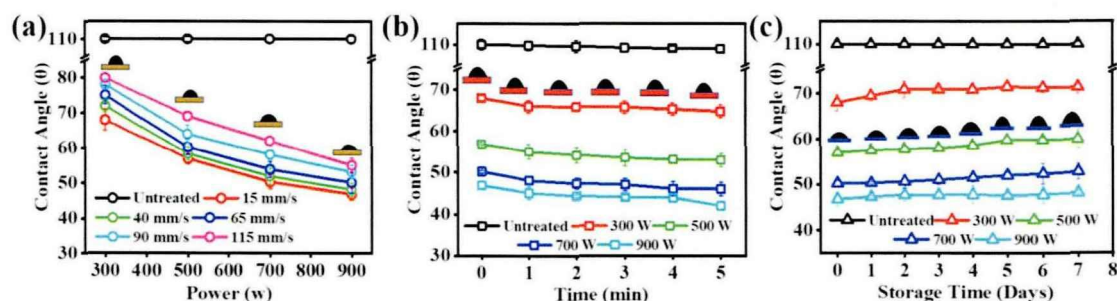


**Fig. 4. 1.** (a) Contact angle of LDPE film after treatment by plasma with different powers. (b) the dynamics of water contact angle for LDPE film modified by plasma at a speed of 15 mm/s selected from (a). (c) shelf-life results of surface tension with storage.

Under the fixed plasma power, taking 300W as an example, the  $\theta$  decreases from  $110^\circ$  to  $68^\circ$ , reducing the polling rate from 115 to 15 mm/s. The lowest  $\theta$  obtained after plasma treatment is  $47^\circ$  under plasma power of 900W and a rolling rate of 15 mm/s. The surface stability of treated LDPE film was shown in Fig. 4.1b & c under the same optimum corona treatment rolling speed of 15 mm/s. The results after corona discharge didn't show any visible change in the SEM results as presented in Fig. 4. 2. The slightly decreasing contact angle reflected water spreading on the modified LDPE surface up to 5 min. Using 300W as an example, the contact angle  $\theta$  reduces from  $68^\circ$  to  $65^\circ$ , increasing measurement time to 5 min.

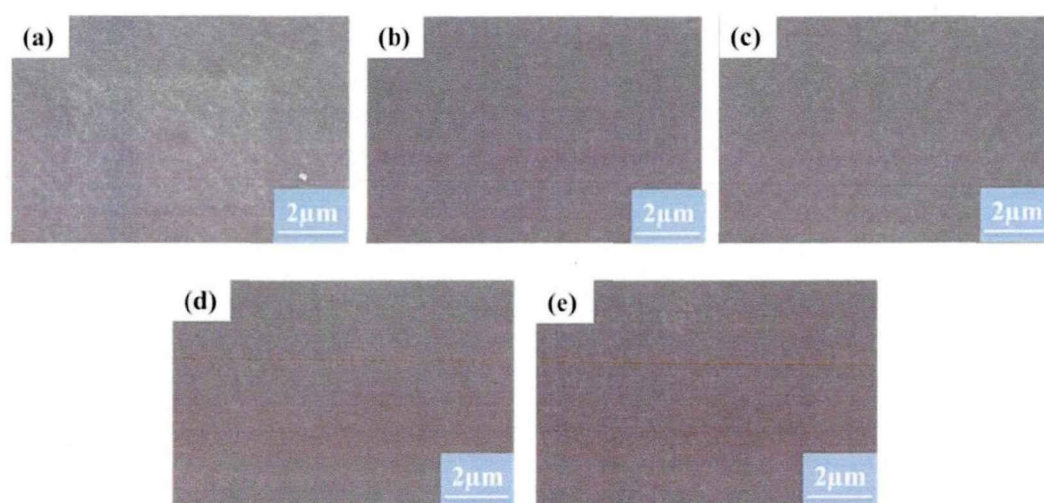


**Fig. 4. 2.** SEM test for samples after corona treatment (a) Untreated, (b) 300W, (c) 500W, (d) 700W, (e) 900W.

#### 4.2.2 Chemical composition

The presence of different functional groups of the anti-fogging layer was directly checked by FT-IR spectroscopy, as shown in Fig. 4. 3. The absorption maxima for the  $\text{CH}_3$  and  $\text{CH}_2$  asymmetric stretching vibrations are  $2920\text{ cm}^{-1}$  and  $2858\text{ cm}^{-1}$ , respectively. C-H bending may be seen in the peaks at  $1460\text{ cm}^{-1}$  and  $720\text{ cm}^{-1}$ . All of these peaks are associated with the LDPE greenhouse film. Some new peaks appear at  $843\text{ cm}^{-1}$ ,  $1085\text{ cm}^{-1}$ ,  $1093\text{ cm}^{-1}$ ,  $1330\text{ cm}^{-1}$ , and  $3300\text{ cm}^{-1}$  after coating by a hydrophilic agent. For L-(P/X), two new peaks appear at  $1093\text{ cm}^{-1}$  and  $3300\text{ cm}^{-1}$  Fig. 4. 3a, which belong to -C-O stretching vibrations and -OH stretching, respectively [176]. After adding TBS to the PVA/X-100 solution, a clear enhancement in intensity is observed for these two peaks. Also, a peak at  $1330\text{ cm}^{-1}$  is related to -C-O stretching [177]. TBS enhances the reaction kinetics by creating a colony of carboxyl groups on the layer surface, as shown by the enhanced intensity of  $1093\text{ cm}^{-1}$  (-C-O) and  $3300\text{ cm}^{-1}$  (-OH). An indication of the high possibility that TBS can dissolve surfactant aggregates Triton X-100 into small parts, making the reaction faster and more robust with PVA

structure, which is reflected by the increase in the intensity of critical two peaks -C-O, -OH [174]. After adding SiO<sub>2</sub>, a new peak at 1085 cm<sup>-1</sup> appears, which belongs to Si-O-C stretching vibrations [178].

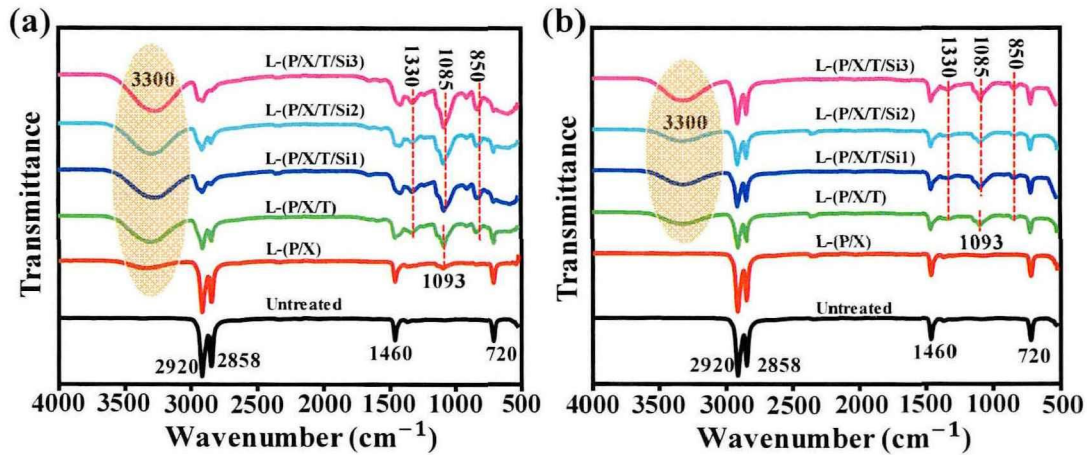


**Fig. 4. 3.** FT-IR spectra of LDPE films with an anti-fogging agent (a) before one month and (b) after one month

The intensity of the characteristic stretching vibration peaks of the Si-O-C and -OH group increases gradually with increasing the mass fraction, which verifies that SiO<sub>2</sub> was linked with PVA structure by a covalent bond [179]. These results reveal that the PVA structure is highly influenced by the content of SiO<sub>2</sub>/Triton X-100 in the presence of TBS. The peak at 850 cm<sup>-1</sup> presented in all samples after adding TBS assigned to C-Cl stretching relative to the TBS saline formation [180]. Fig. 4. 3b presents the FT-IR spectra of the anti-fogging layer after a one-month hot fog test. The sample L-(P/X) shows the poorest hydrophilicity and less stability, and almost no characteristic peak of the carboxyl group was observed after 13 days. This indicates the film had lost the anti-fogging agent. All the other samples L-(P/X/T/Si1), L-(P/X/T/Si2), and L-(P/X/T/Si3), show a slight decrement in the hydrophilic bonds after one month, reflecting good stability against fogging. From all the above results, the addition of TBS plays an essential role in improving the wetting properties.

To further analyze the surface stability of modified LDPE, the measurement was conducted daily for one week, as summarized in Fig. 4. 1c. As the active surface is unstable, a slight contact angle  $\theta$  is observed. Taking 300W as an example, the contact angle increases slightly from an initial 68° to 71° after one week. The above results show a minor influence of storage time on surface wettability. As a confined space, the interaction between water and surface changes with variable surface wettability. In terms of surface interaction, there are three different kinds of water, namely, free water, Immobilized water, and bound water. Free water seldom



reaches the surface, and most interactions occur between water and water. Simultaneously, the immobilized water softly interacts with the character (stronger than free water but weaker than bound water), resulting in water-surface and water-water interactions. Bound water is firmly bound to the surface. The water-surface interactions are very robust, while water-water interactions are feeble. The distribution and fraction of these three kinds of water could significantly influence nanoparticle distribution on the LDPE surface in the later coating process. Therefore, the precise determination of different kinds of water is necessary.

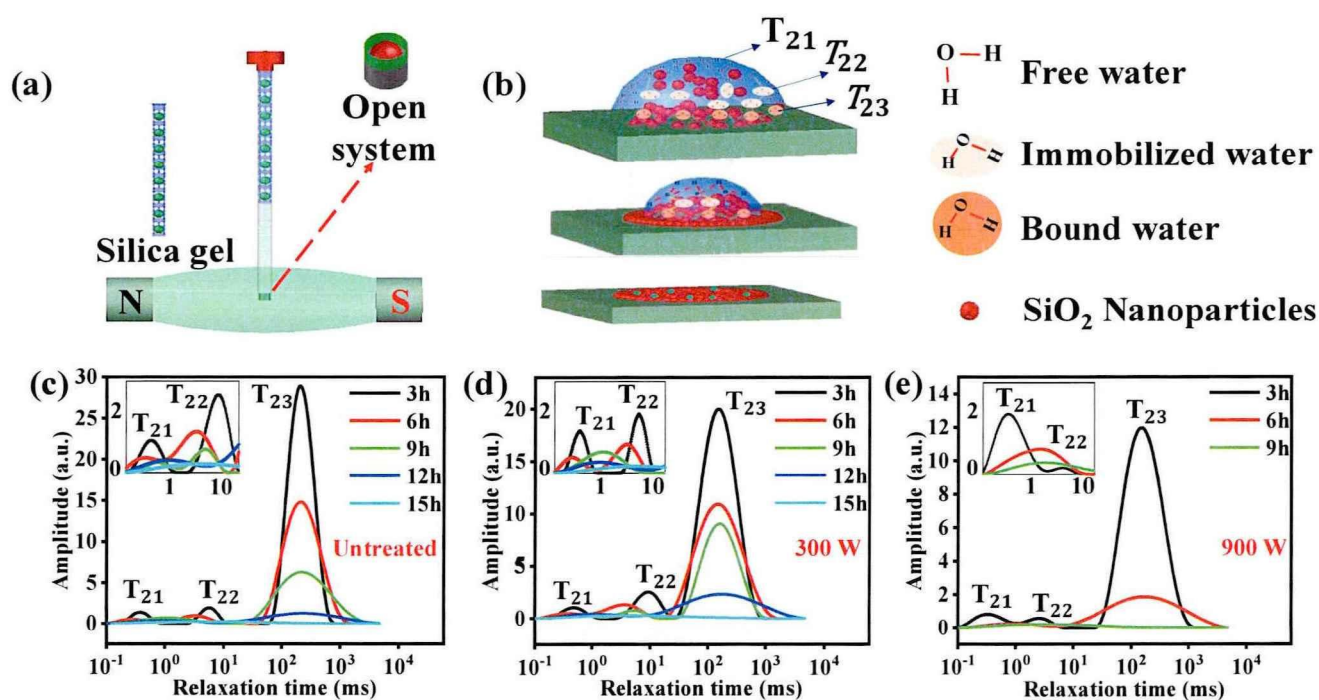


**Fig. 4.** (a) Schematic illustration of the NMR experiment for tracking the evaporation process *in-situ*. (b) different kinds of water on the surfaces of modified LDPE with different surface wettability. (c, d, and e) the evolution of different kinds of water as reflected by the  $T_2$  relaxometry after inverse Laplace transform.

The low field time-domain NMR (TD-NMR) has been frequently used to analyze different water fractions through spin-spin  $T_2$  relaxometry [174] Fig. 4. 4a. The CPMG with a recycling time of 18s and a total number of scans of 128 was used to obtain  $T_2$ . After inverse Laplace transform [181], three distinct peaks are found, which are assigned to bound water  $T_{21}$  (0.1 - 2.5ms), immobilized water  $T_{22}$  (2.5-25ms), and free water  $T_{23}$  (25 - 1120ms) [182], As shown in Fig. 4. 4b. The bound water is firmly bound to the surface, and the water-surface interactions are very robust, while water-water interactions are feeble [120]. The free water is non-constraint, with dynamics similar to that in the bulk state. The untreated LDPE shows the highest amount of free water fraction, which decreases with an increase in power, whereas that treated by plasma of 900W shows the



lowest one, as shown in Fig. 4. 4c, d & e. A minor fraction of the free water observed in treated LDPE film might be due to the high spreading of the droplet on the hydrophilic surface.

Increasing plasma power leads to an increasing fraction of bound water, consistent with the above contact angle measurements. Additionally, *in-situ* measurements of three different kinds of water were obtained by time-resolved  $T_2$  relaxometry. Limited by the total amount of water, the time resolution in the current study is  $\sim 3$  hours. However, the general tendency of the evolution of different water was obtained. The relative fraction of free water decreases dramatically during the evaporation process for the original LDPE film and almost diminishes after 12 h. For treated LDPE film 900W, the evaporation is much faster than the other two under the same condition. Since the final obtained nanoparticle aggregation is closely related to different kinds of water distribution, thus obtained time-resolved water fraction evolution provides kinetic information for the nano-particle layer formation, which will be discussed in the following section. Here, using polyvinyl alcohol (PVA) as the polymer matrix, various surfactants with PVA polymer matrix used as a coating in this research proved their ability to increase surface hydrophilicity of LDPE films. The addition of TBS can further reduce the contact angle. TBS plays a significant role in maintaining the PH at  $\sim 7.5$  and dissolves surfactant aggregates into small parts, improving the interactivity between the PVA and surfactants. The addition of nano-sized  $\text{SiO}_2$  further increases the hydrophilicity of the LDPE film surface, and the contact angle can be reduced as low as  $2^\circ$ .

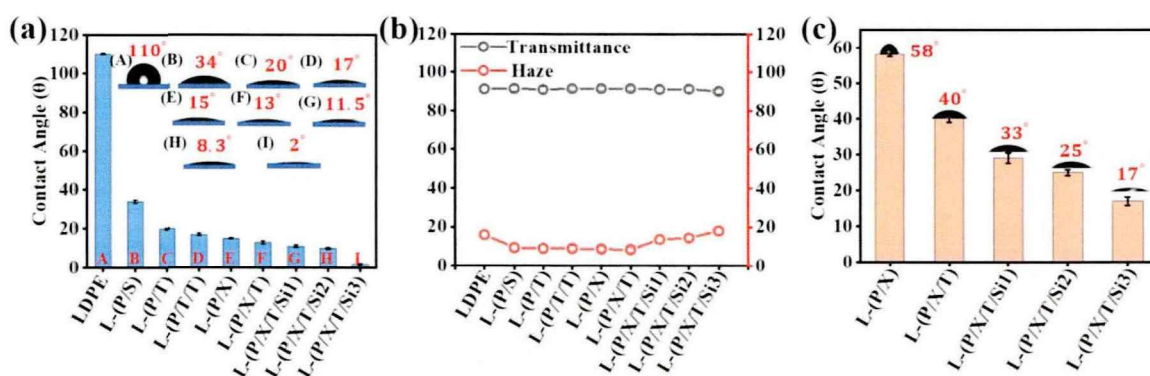


**Fig. 4. 5.** (a) The contact angle of different anti-fogging layers was measured together with (b) transmittance and haze, and (c) the contact angle was measured after one month.

Despite surface wettability, the optical property of LDPE film should not be primarily changed. Fig. 4. 5b shows the influence of different anti-fogging layers on the transmittance and haze of LDPE film. Compared

with the original LDPE film (transmittance of 91% and moisture of 15%), no significant changes are observed in the optical property of all modified films. This suggests currently proposed anti-fogging agents do not significantly influence the optical property of greenhouse film. A hot-fog test further checked the stability of the anti-fogging layer.

Fig. 4. 5c shows the contact angle after being exposed to the hot fog test at 60 °C for one month. The result shows an increasing contact angle from 15° to 58° for the sample L-(P/X), indicating that the coated layer was partially destructed. The addition of SiO<sub>2</sub> nanoparticles significantly increases the stability.

#### 4.2.3 Surface morphology

The surface morphology as captured by the optical microscopy images and SEM is provided in Fig. 4. 6 the untreated LDPE sample images were presented in Fig. 4. 6a, a\*. A smooth surface is The more addition of SiO<sub>2</sub> nanoparticles, and the higher is the stability of the anti-fogging layer. The sample L-(P/X/T/Si3) shows the highest coating stability observed for L-(P/X), as shown in Fig. 4. 6b & b\*. This indicates the homogeneous distribution of the anti-fogging layer on the LDPE film surface. After adding the TBS, the surface keeps smoothed Fig. 4. 6c & c\*. A previous study proved that when the SiO<sub>2</sub> nanoparticles interact in an alkaline intermediate, they are easily aggregated into particles and dispersed on the surface [165], which makes the presence of TBS significant in our experiment to maintain the alkalinity during the reaction.

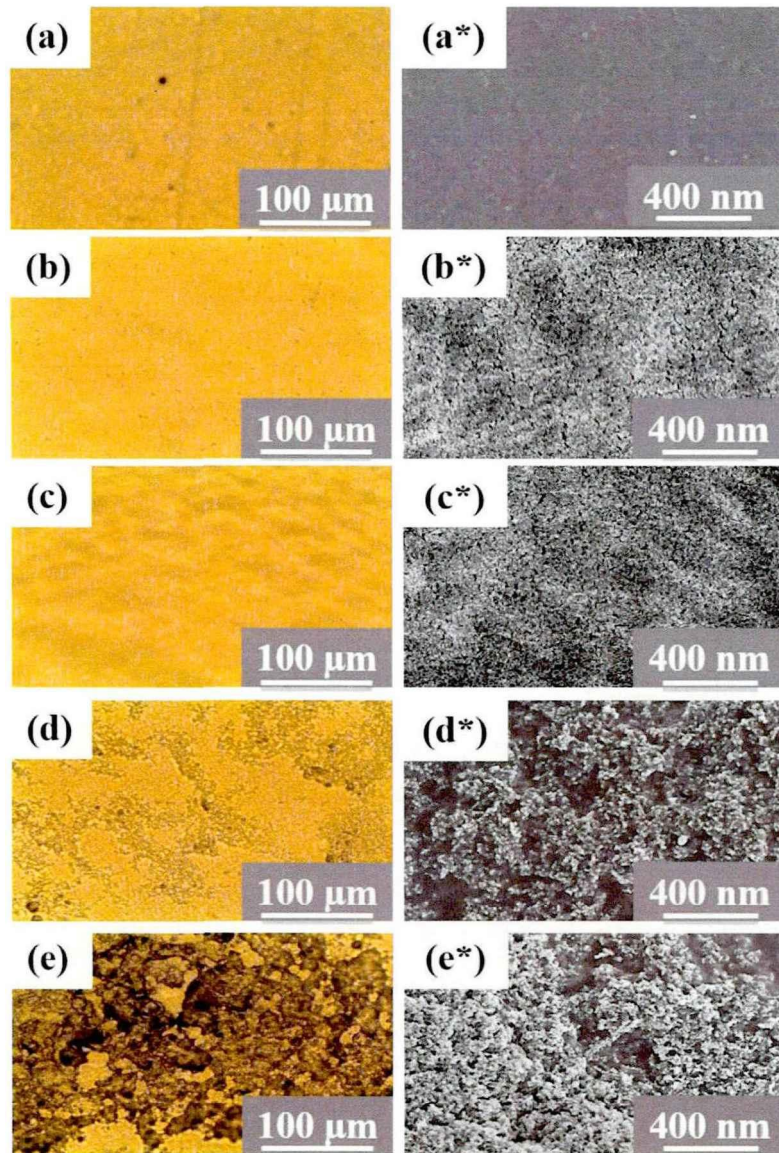


**Fig. 4. 6.** Optical microscopy images on the left side (a, b, c, d, e) and SEM on the right side (a\*, b\*, c\*, d\*, e\*) for the anti-fogging films (a, a\*) untreated LDPE (b, b\*) L-(P/X), (c, c\*) L-(P/X/T), (d, d\*) L-(P/X/T/Si1), and (e, e\*) L-(P/X/T/Si3).

The addition of silica nanoparticles with a diameter of  $12 \pm 5$  nm shows slight aggregations Fig. 4. 6d & d\*. When the SiO<sub>2</sub> concentration increases from 0.05 to 0.15 wt.%, the coating layer becomes thicker Fig. 4. 6e & e\*. The morphology test for samples after washing by the hot anti-fogging test is presented in Fig. 4. 7. For the first sample (Fig. 4. 7e, e\*) L-(P/X), it is obvious to find that the sample loses most of the coating layer



compared with that before one month. Other samples show no significant decrease in coating layers, and samples maintain their antifogging properties Fig. 4. 7( f, f\* ~ h,h\* ).

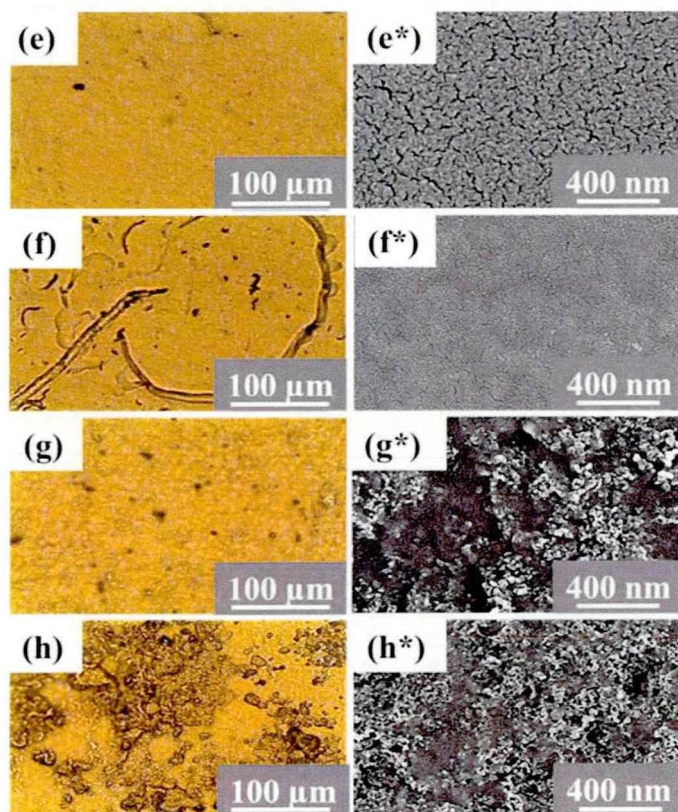


**Fig. 4. 7.** Optical microscopy images (e, f, g, and h) and SEM images (e\*, f\*, g\* and h\*) for the anti-fogging films after one month (e, e\*) L-(P/X), (f, f\*) L-(P/X/T), (g, g\*) L-(P/X/T/Si1), and (h, h\*) L-(P/X/T/Si3).

#### 4.2.4 Anti-fogging agent

When the contact angle is less than  $40^\circ$ , the water will condense into a continuous film on the hydrophilic surface [98] and other coatings on the LDPE in addition to plasma treatment.

##### 4.2.4.1 Accelerated dripping test

Two main techniques were applied for the shelf-life test to evaluate the anti-fogging properties; the first/ten drops and the extended shelf-life test.

###### 4.2.4.1.1 First and ten drops time

Uncoated LDPE fogged within a short time, while antifogging films remain clear. Fig. 4. 8a shows the schematic illustration for measuring the formation time of the first and ten drops of water. As shown in Fig. 4. 9b, the addition of different anti-fogging layers results in various anti-fogging performances. The addition of X-

100 results in the first and ten drop times of 13 and 10 min, respectively. TBS significantly reduces such time to 9 minutes for 1<sup>st</sup> and 7 min for 10<sup>th</sup> drops. The addition of SiO<sub>2</sub> further reduces such time. The more the added SiO<sub>2</sub>, the shorter the time for the formation of the water droplet will be until reaching a minimum time of 4 and 1.5 min for the first and ten drops, respectively. However, as shown in Fig. 4 .5b, adding more nanoparticles will significantly increase the haze of the whole greenhouse film. The balance between surface wettability and optical property should be maintained.

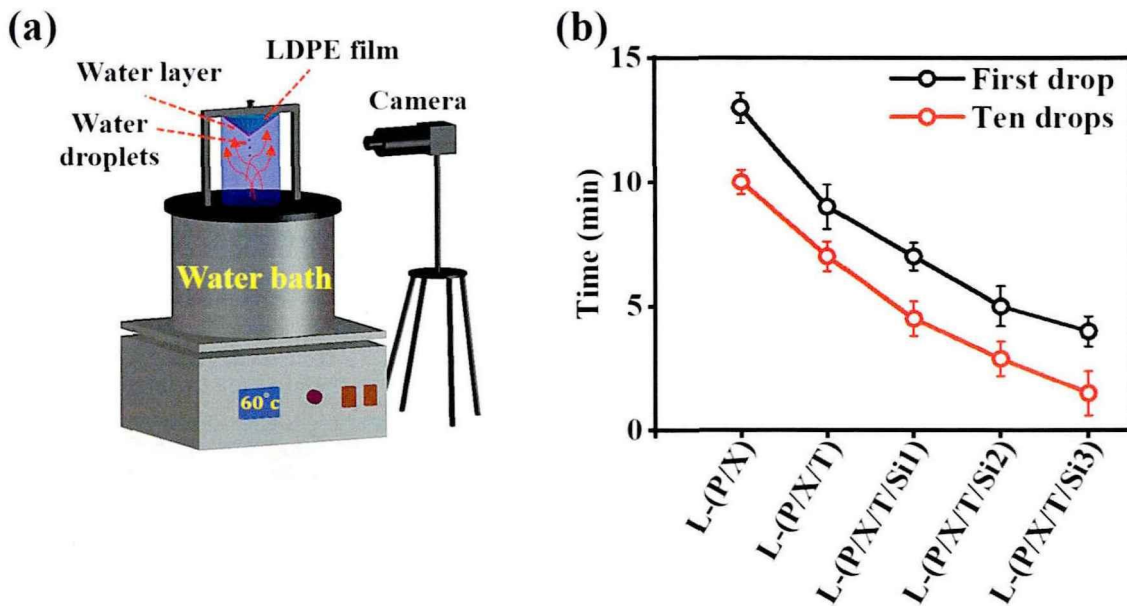


**Fig. 4. 8.** (a) Diagram shows the method for detecting the time for the formation of the first and ten drops, (b) experimental results of different anti-fogging layers.

#### 4.2.4.1.2 Shelf-life test

The anti-fogging film is reported to lose its efficacy when 33% of the film surface's testing area is covered by water droplets [46][91][154]. The principle of the long-life test is presented in (Fig. 2. 6). As long as one month of the above anti-fogging layer, long-life tests are summarized in Fig. 4. 8. Three preliminary experiments have been done for untreated samples, the sample treated with plasma, and the sample coated with pure PVA to investigate the effectiveness of modified samples against fogging. Fig. 4. 9a1, a2 & a3. The original LDPE film and the film treated by a high power (900W) and the film-coated by pure PVA were fogged in less than 5 s. Fig. 4. 9b1, b2 & b3. For samples coated by anti-fogging agents, all exhibit good resistance to fog in 30 min and above. Fig. 4. 9c & d. After 168 h, the L-(P/X) gradually lost its hydrophilicity, and a full loss of about 99% of the anti-fogging agent was observed after 13 days.

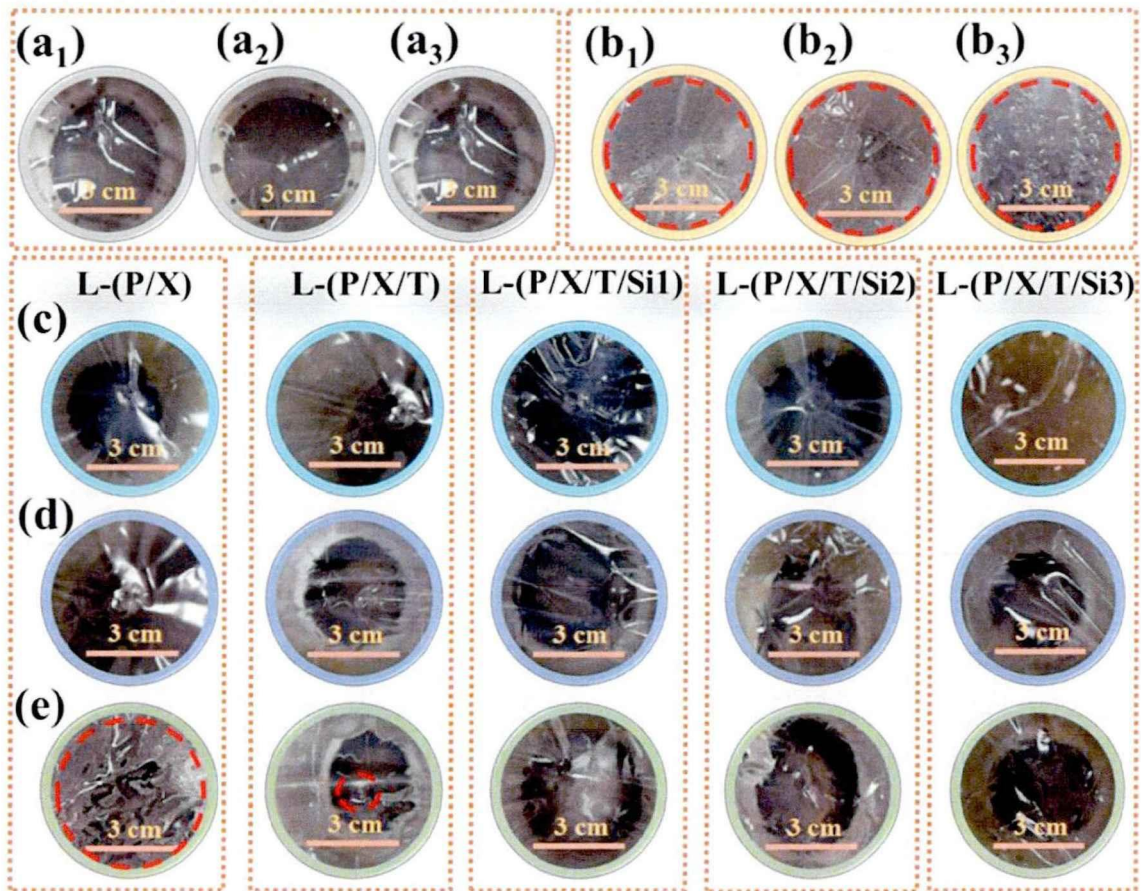


**Fig. 4. 9.** Original samples images before hot fog rest (a1) untreated, (a2) plasma treatment (900W), and (a3) coated by pure PVA. Hot fogging test images on LDPE film surface in less than 5 seconds (b1) untreated, (b2) plasma treatment (900W), (b3) coated by pure PVA. Long-time fogging test for different antifogging films after (c) 30 minutes, (d) 7 days, and (e) 30 days.

That means the anti-fogging agent continuously faded away by exposition to the hot evaporation of water. This is a severe problem for anti-fogging agents, resulting from small coating cohesion and the weak link between the anti-fogging and surface substrate. After adding TBS to (P/X) solution, the dripping duration is increased to 720 h with 5.6% droplets covering the area. As mentioned above, TBS dissolves surfactant aggregates into small portions, which helps create a strong bond between the PVA and surfactant molecules. All samples containing silica L-(P/X/T/Si1), L-(P/X/T/Si2), and L-(P/X/T/Si3) show excellent anti-fogging properties in more than 720 h Fig. 4. 9e and without any loss in the efficiency was observed in table 4. 1. The results demonstrate that increasing the concentration of SiO<sub>2</sub> is crucial for improving the duration of migration of anti-fogging agents in films with excellent fogging resistance. For further investigation, the cross-sections of



modified films presented in (Fig. 4. 10) were obtained to check the coating thickness before and after the hot fog test. (Fig. 4. 10a) the sample L-(P/X) coating thickness is about  $2.53 \mu\text{m}$  before exposure for one month to the hot fog test. During the hot fog test, it lost its thickness until it disappeared in 13 days (Fig.4. 10b). While the coating contained silica nanoparticles and TBS buffer solution, the coating thickness decreased slightly. For example, the L-(P/X/T/Si3) sample recorded the lowest loss in thickness from  $2.77 \mu\text{m}$  to  $1.9 \mu\text{m}$  after exposure to the heat fog test for a month, presented in Fig. 4. 10c & d.

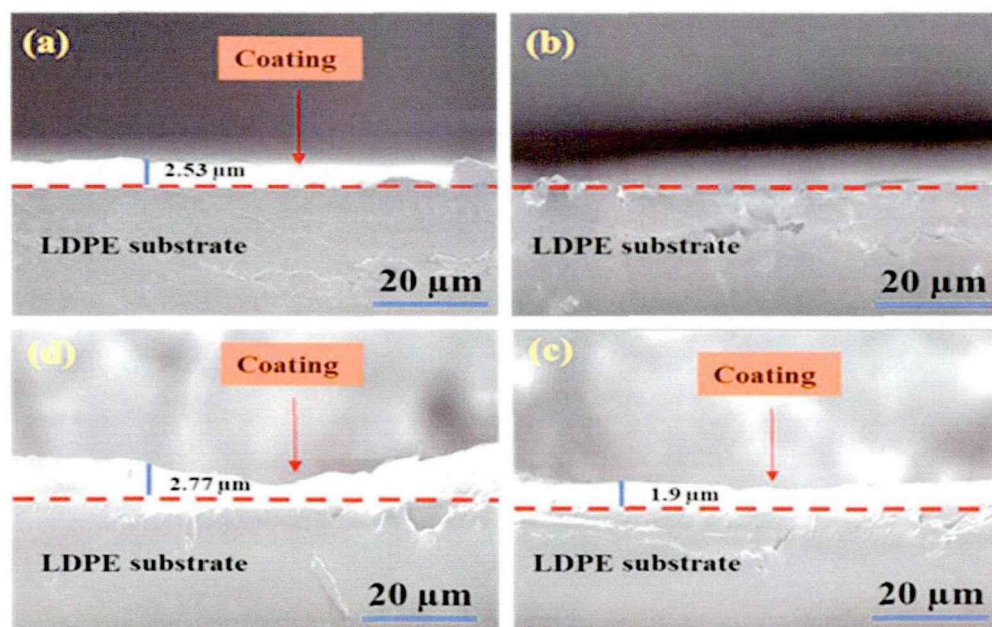


**Fig. 4. 10.** SEM images of modified LDPE cross-sections. (a) L-(P/X) before one month, (b) L-(P/X) 13 days, (d) L-(P/X/T/Si3) before one month, (c) L-(P/X/T/Si3) after one month.

**Table 4. 1.** Accelerated dripping properties of antifogging coating films

Film Sample	Dripping Temperature ( $^{\circ}\text{C}$ )	Dripping Time (Days)	Droplets covering area
L-(P/X)	60	13	99%
L-(P/X/T)	60	>30	5.6%
L-(P/X/T/Si1)	60	>30	0%
L-(P/X/T/Si2)	60	>30	0%
L-(P/X/T/Si3)	60	>30	0%



#### 4.2.5 Coatings mechanical properties

After one day of exposure to the hot fog test, a sandpaper test was applied for unmodified and modified films. Then optical microscopy was taken directly after the test (Fig. 4. 11). The entire film showed significant damage (Fig. 4. 11a). However, the results of the modified films showed varying results.

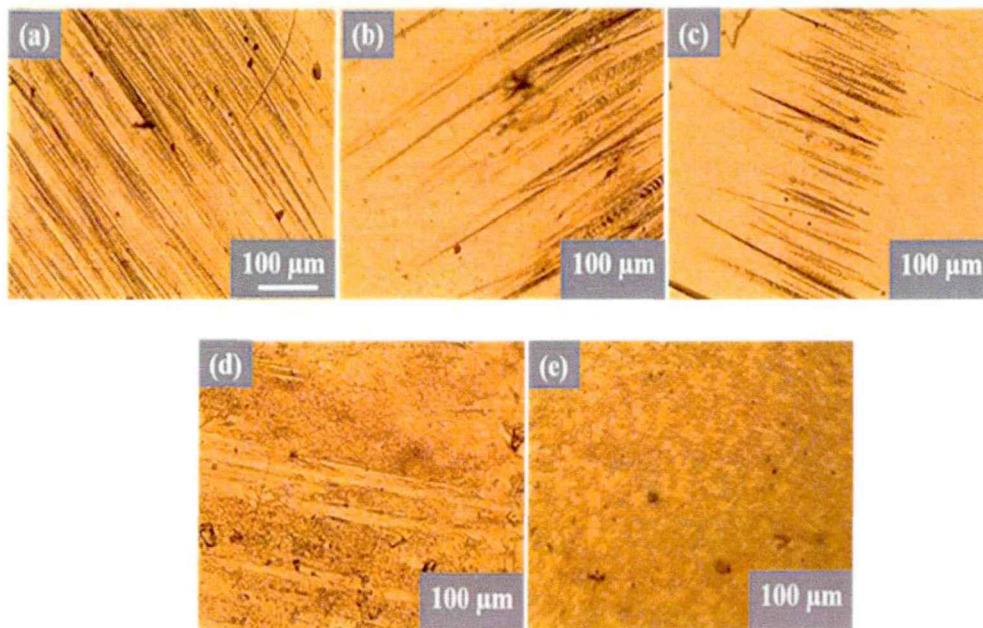


**Fig. 4. 11.** Optical microscope images after sandpaper abrasion test a) unmodified, (b) L-(P/X), (c) L-(P/X/T), (d) L-(P/X/T/Si1), (e) L-(P/X/T/Si3).

The sample L-(P/X) showed a close result to the whole film in terms of damage (Fig. 4. 11b), and then this damage gradually decreased after the addition of TBS and silica L-(P/X/T) (Fig. 4. 11c), and L-(P/X/T/Si1) (Fig. 4. 11d) respectively. The sample with the most resistance against scratch is L-(P/X/T/Si3), which does not show any damage on the surface after the mechanical test (Fig. 4. 11e).

#### 4.3 Conclusion

In this work, a low-cost super-hydrophilic anti-fogging layer was prepared to increase the anti-fogging performance of LDPE greenhouse films yet maintain an excellent optical property with long shelf life. After plasma treatment, the hydrophilic polyvinyl alcohol (PVA) was used as the polymer matrix, interacting with the hydrophobic LDPE substrate. The TBS serves as the buffer solution, which results in well-dissolved surfactant, i.e., Tween 20, SDS, and Triton X-100, in the solution. The wettability and shelf-life tests show the performance of the coating layer with the addition of Triton X-100 is much better than that with Tween 20 and

SDS. As seen by the SEM data, the use of Triton X-100 may result in a more homogenous dispersion of silica throughout the coating process. Under the optimized condition, the modified LDPE films with PVA-based hydrophilic anti-fogging layer show the best wettability with a contact angle of  $2^\circ$ , with long-shelf-life over 30 days without fogging during the hot fogging test, and high transmission of 91% (the same as pure LDPE film), while the entire film shows a contact angle of  $110^\circ$  and fully fogs in less than 5 seconds. Therefore, the results of the current work show the addition of buffer solutions to an-ionic or non-ionic surfactants, and the application of hydrophilic PVA can synergistically enhance the homogeneous distribution of silica. To make a high-quality anti-fogging film, the following factors must be considered: 1) the solution's viscosity, which is strongly connected to the interaction between silica and the film substrate; 2) the distribution of silica, the distribution of which controls the coated film's final wettability and shelf-life. Combining different surfactants is sometimes necessary to fully satisfy the above goal. The results of the current work provide a new pathway to creating a long shelf-life anti-fogging film.

## **Chapter 5 Dual-Functional Antifogging/Antimicrobial Based Natural Polymer Coating for Glass Applications as Investigated by Low Field NMR**

Due to the obvious proliferation of COVID-19, developing an antifogging/antimicrobial layer is critical for many applications. This chapter emphasized the development of a novel biopolymer and ecologically friendly layer with antifogging and antibacterial qualities. A dip-coating procedure on glass substrates was used to create the dual-functional coating, which comprised a layer of chitosan (Ch) and modified silica nanoparticles. The dual-functional coating created in this study can be widely employed in various applications that require anti-fog and antibacterial layer properties.

### **5.1 Introduction**

Fogging may dramatically degrade the clarity of optical substrates, causing discomfort and posing a risk in everyday life. As a result, there is a significant need for effective antifogging surfaces that are employed in a variety of applications such as; eyeglasses [183], camera lenses [184], mirrors [185], goggles [186], display devices in analytical instruments, and other similar applications. Lenses fogging is common in medical apparatuses such as laparoscopic and endoscopic [187]. It can cause a quick loss of vision for the operator and stoppage in treatment, leading to difficulties. Super-hydrophilic coatings allow water droplets to spread and agglomerate quickly, leading to the development of a pseudo-film and the eradication of fog from surfaces. [187]. Aside from the fogging issue, microbial adhesion on the lens surface may threaten the safety of medical tools. However, medical instrument-related infections have emerged as one of the most significant medical dangers due to microbial growth [188].

Furthermore, many studies have shown the significance of wearing goggles when in touch with patients to protect against hazardous disorders such as severe acute respiratory syndrome to the eyes infection with a coronavirus [189]. When caring for COVID-19 patients, fogging goggles is a severe issue because the fogging affects eyesight, reducing productivity. On the other hand, washing and reusing goggles increases the risk of infection. Therefore, manufacturing and antifogging/antimicrobial layer are crucial.

Chitosan is nature's second most common polysaccharide after cellulose. It is a cationic biopolymer derived from deacetylated chitin, comprised of a glucosidic residue with one amino group and two hydroxyl groups [190]. Chitosan is one of the most often utilized polymers in biomedical applications because of its several positive features, including biocompatibility, biodegradability, antibacterial activity, and hemostatic capabilities [191], which opened the field for many applications such as food industry anti-cholesterol and fat

binding [192], agriculture (coating of seeds and fertilizer) [193], regulated agrochemical release [194], excipients for drug delivery [195], and gene delivery [196]. Chitosan is quickly processed into gels [197], membranes [198], nanofibers [199], microparticles [200], nanoparticles [201]. Despite its numerous advantages and distinguishing characteristics, chitosan films have significant drawbacks, such as a weak barrier to water vapor vapors and poor mechanical and thermal properties, limiting its usage in various applications [191]. As a result, a plasticizer such as glycerol should be used to improve the flexibility of the chitosan films [202].

On the other hand, plasticizer decreases intermolecular interactions, increase free volume, stimulate molecular motions, and lower polymer films' barrier properties [203]. Furthermore, adding a plasticizer to chitosan reduces its mechanical and thermal stability [204]. However, one way to increase the mechanical strength is by reinforcing the matrix using mineral fillers such as nanoparticles [205]. Because of their excellent biocompatibility, low toxicity, thermal stability, simple synthetic approach, and large-scale synthetic availability, silica nanoparticles are commonly employed in a variety of applications such as electronics [206], optics [207], medicine [208], etc. These applications need nanoparticles interaction with macromolecules such as proteins, polymers, and surfactants [208].

Recently, silica nanoparticles have been introduced into polymers to increase mechanical and interfacial characteristics for various applications, including absorbent [209] and reinforced polymeric materials [210]. I.A. Wonnie Ma et al, [191] used ionotropic gelation to create a chitosan/silica composite using sodium tripolyphosphate. After 60 days, the presence of a hybrid chitosan/silica composite up to 0.8 wt.% resulted in a considerable active reinforcing agent for corrosion protection applications with the maximum coating resilience,  $(1.97 \pm 0.01) \times 10^{11} \Omega$  and lowest breakpoint frequency,  $51 \times 10^{-3} \text{ Hz}$ , according to the experimental results. Furthermore, new research on anti-biofouling surface coatings has revealed that neutrally charged and explicit hydrophilic coatings can minimize both hydrophobic and electrostatic interactions with biomolecules [211], [212], [213]. Because they have strong interactions with water molecules, they can create a firm layer in the coating, and they have been widely explored as anti-biofouling coatings [45]. This layer acts as a barrier against protein cell and bacterium adsorption, allowing it to resist or eradicate biofouling effectively [214]. Hence the antifogging/antimicrobial layer require a low-cost and high-efficiency layer with an extended shelf life. Therefore, understanding nanoparticles' underlying process of polymer structure modification is critical for enhancing antifogging/antimicrobial coating applications.

Recently time-domain (TD) NMR has gained popularity due to its numerous applications, including monitoring changes in water status and fraction mobility throughout processing [120]. It might also be used for other materials like muscle tissue [120] and food like fruits [122], grains, and vegetables [123]. It's a non-

destructive, non-invasive approach for determining water mobility with minimal pretreatments. Depending on its mobility under atmospheric conditions, water is categorized into three groups using NMR: bound, immobilized, and free [124][92].

In this study, the impact of *MSN* in chitosan structure was explored to inhibit the development of fogging and microbiological activity based on water fractions mobility, allowing for a better understanding of the significance of these fractions in avoiding such undesirable events.

## 5.2 Results and discussions

### 5.2.1 Chemical composition

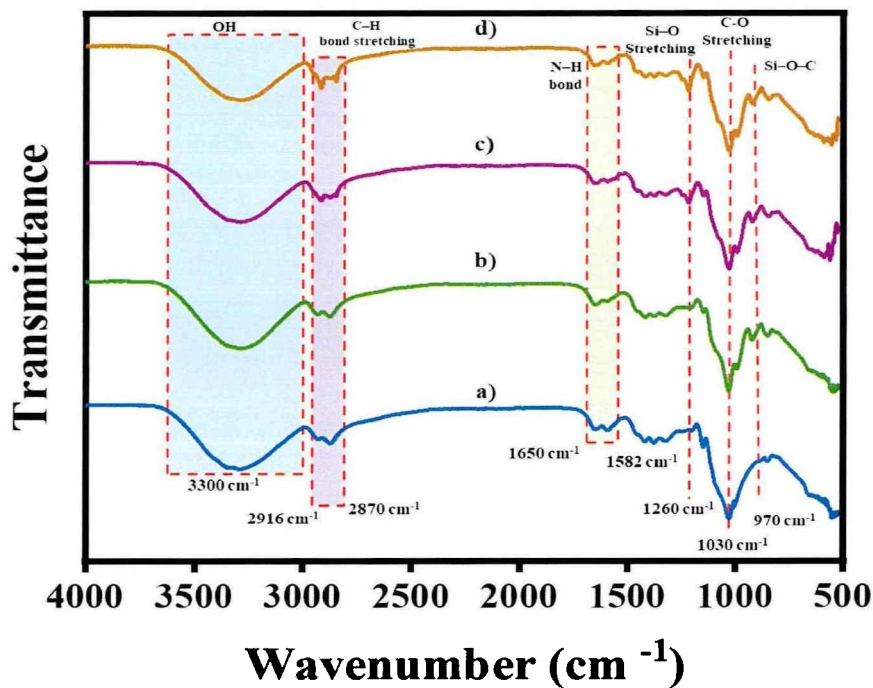


**Fig. 5. 1.** FT-IR spectra of composite chitosan coating layers a) Ch, b) Ch/SiO<sub>2</sub> (1), c) Ch/SiO<sub>2</sub> (2), d) Ch/SiO<sub>2</sub> (3).

Different functional groups in the antifogging layer were examined using ATR-FTIR spectroscopy, as shown in Fig. 5. 1. Chitosan has a distinct peak at around 3300 cm<sup>-1</sup> due to its multiple -OH group [101]. In all spectra, the reflection peak at 2876 cm<sup>-1</sup>, 2941 cm<sup>-1</sup> is caused by -CH stretching and flexural liberation vibrations, respectively [215]. The FTIR spectra of the layers revealed significant absorption peaks at 1640 cm<sup>-1</sup> and 1550 cm<sup>-1</sup>. (Fig. 5. 1a), which have been attributed to carbonyl stretching (amide I) and NH bending, respectively [216].

After adding silica nanoparticles, the intensity of Si-O bonds rises as the concentration of silica increases, as seen by absorption at  $1260\text{ cm}^{-1}$  (Fig. 5. 1(b, c, d)), where Si-O bond modes from silica, silane/silica interface, and silane-silane polymer overlap [217]. The C-O stretching is liable for another notable peak at  $1030\text{ cm}^{-1}$  [173]. The -OH groups on the  $\text{SiO}_2$  surface may react with the -OH groups of chitosan, resulting in a peak stretching vibration of Si-O-C at around  $970\text{ cm}^{-1}$  [218]. When *MSN* was added, the hydroxyl group peak shifted to the low wavenumber region with diminishing intensity as the silica concentration grew. The enhanced C-H bond stretching at the bond at  $2916\text{ cm}^{-1}$  and  $2870\text{ cm}^{-1}$  suggests that  $\text{SiO}_2$  might induce hydrogen bond/ionic interactions with the hydroxyl group in the chitosan structure (Fig. 5. 1(c, d)). Therefore hydroxyl groups of *MSN* successfully formed intermolecular hydrogen bonds with the amino and hydroxyl groups of chitosan [219], which improved the mechanical characteristics of the Ch/ $\text{SiO}_2$  layer and enhanced the fogging/microbial resistance.

### 5.2.2 Surface wettability

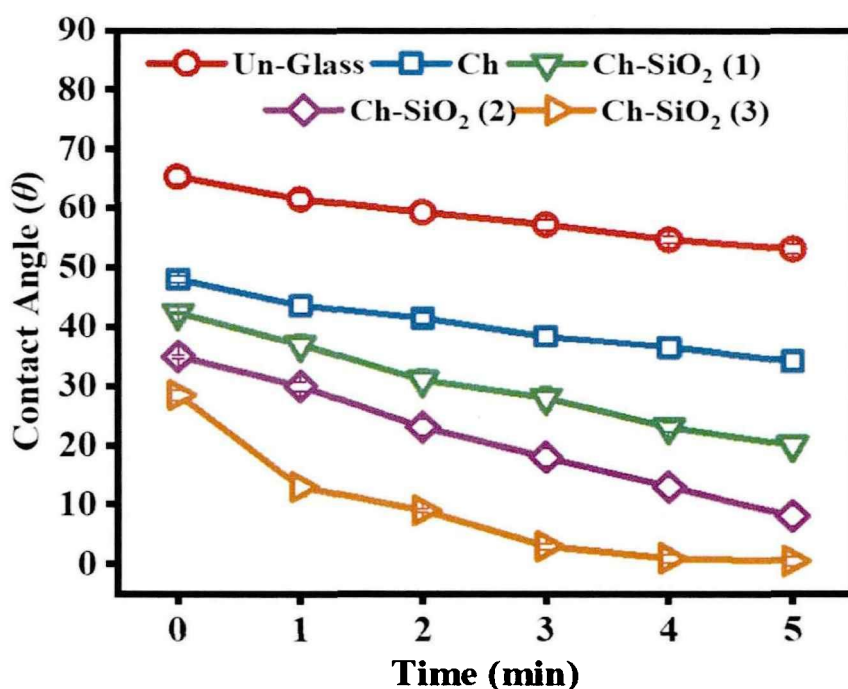


Fig. 5. 2. The contact angle ( $\theta$ ) for different antifogging coatings layers is based on silica concentration.

The contact angle ( $\theta$ ) is frequently described as a good predictor of surface wettability changes [90]. Therefore when the  $\theta$  is less than  $40^\circ$ , the water will condense into a continuous layer on the hydrophilic surface



[173]. Glass substrate is usually characterized by low surface energy, which has  $\theta$  of more than  $65^\circ$  in the surrounding environment, with difficulties droplet spreading from  $65^\circ$  to  $53^\circ$  in 5 min Fig. 5. 2.

The chitosan layer increased the surface roughness by reducing the  $\theta$  to  $48^\circ$  and steadily decreasing as the nanoparticle dose rose. When the maximum amount ( $12.5 \times 10^{-3} \%$ ) of *MSN* was added, the  $\theta$  was reduced to  $28^\circ$  with a fast-spreading during the time, which reached  $0.5^\circ$  in 5 min, indicating a high level of surface wettability.

### 5.2.3 Transmittance and haze

Various optical tests were applied for modified glass to quantify the antifogging properties, such as; the test after coating and after hot and cold fogging tests to assess coating durability under diverse climate conditions (Fig. 5. 3). A thorough assessment of the data revealed that the sample coated by the chitosan layer was more transparent and had a lower haze value than untreated glass. Even if it's a little, this change is often evident to the naked eye due to the chitosan coating smoothing the original glass surface.

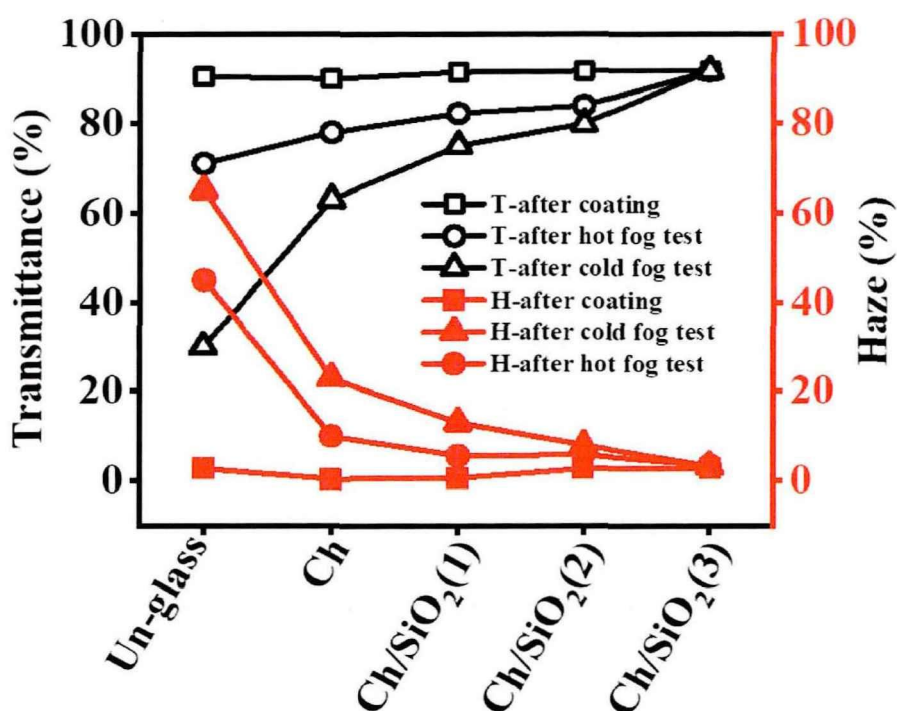
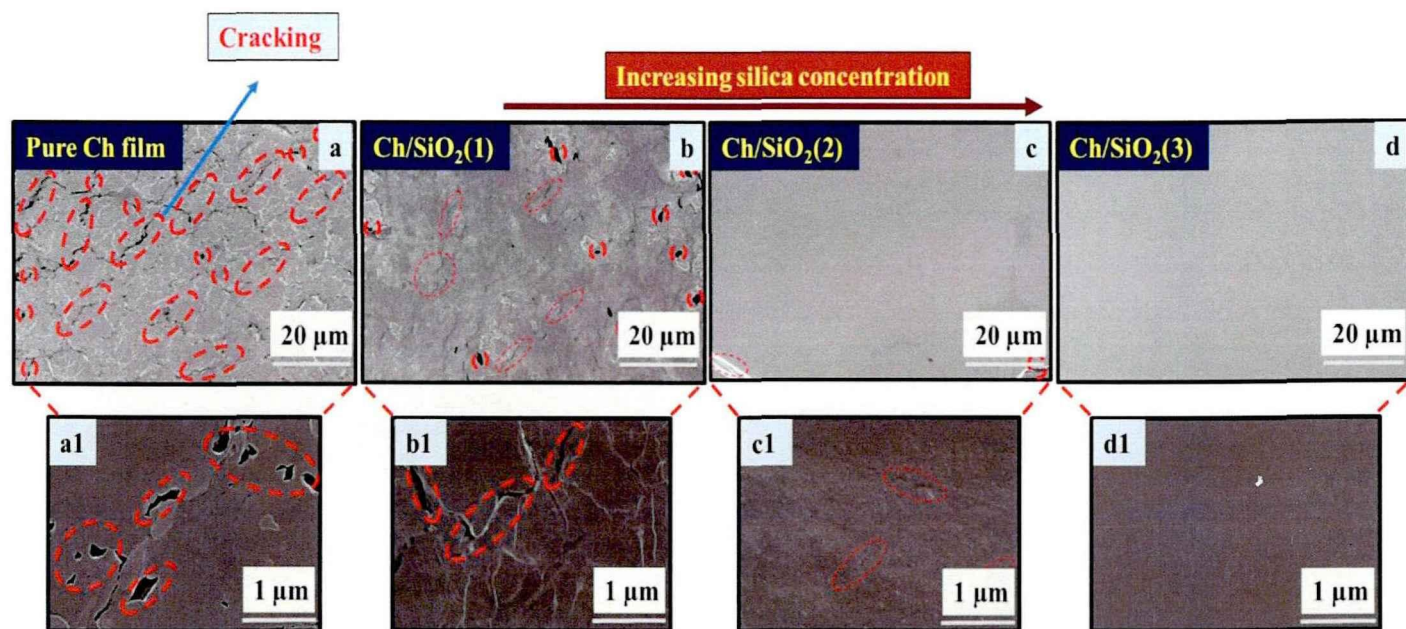


Fig. 5. 3. Transmittance and haze after-coated glass, -cold-warm test, and -hot-vapor test.

The addition of *MSN* at varied dosages resulted in virtually a slight increase in transmittance properties, revealing the homogenous dispersion of silica nanoparticles in the chitosan structure. On the other hand, the maximum amount of *MSN* attribution resulted in a bit of rising in haze characterization, showing that those

rising roughness levels enhanced the overall haze component associated with surface scattering [220]. Despite its improved initial optical properties, uncoated glass performed poorly in hot and cold fogging tests because of its low surface wettability. However, even after cold and hot-vapor testing, the chitosan layer demonstrates its capacity to improve optical characteristics. Furthermore, the stability of optical properties increased steadily with increasing *MSN* concentration. It is worth mentioning that the optical properties of the Ch/SiO<sub>2</sub> (3) sample were impressively consistent throughout all sorts of fogging tests.

### 5.2.4 Surface morphology



**Fig. 5. 4.** Scanning electron microscopy of composite chitosan coating layers, a) Ch, b) Ch/SiO<sub>2</sub> (1), c) Ch/SiO<sub>2</sub> (2), d) Ch/SiO<sub>2</sub> (3). (a1, b1, c1, d1) zoom in.

The surface morphology of the composite coatings is shown in Fig. 5. 4. Generally, cross-linkers employed to generate cross-linked polymer gels can be metallic or organic. Metallic cross-linkers form ionic bonds with polymers, whereas organic cross-linkers create covalent bonds [221]. As a consequence of shrinkage tensions developing during the drying process, the layer of chitosan, which was cross-linked by organic cross-linkers (glycerol) with a 30 μm thickness (Fig. 5. 5(e, e1)), revealed so much cracking after drying Fig. 5. 4(a, a1) [222]. This is because microspores and fractures with poor cross-linking density caused instability and provided corrosion during drying [223]. On the other hand, cracks and porosity are reduced when nanoparticles are added to the chitosan structure. *MSN* improved the polymeric coatings' resilience to defects and fractures due to their compatibility with the chitosan structure Fig. 5. 5(f, f1). Therefore, due to nanoparticle-matrix solid

interaction, the more addition of *MSN*, the better cracking resistance [224], which led to an increase in corrosion resistance Fig. 5. 4(b, b1) and Fig. 5. 4(c, c1), until no cracking was recognized when the *MSN* concentration reached ( $12.5 \times 10^{-3} \%$ ), Fig. 5. 4(d, d1).

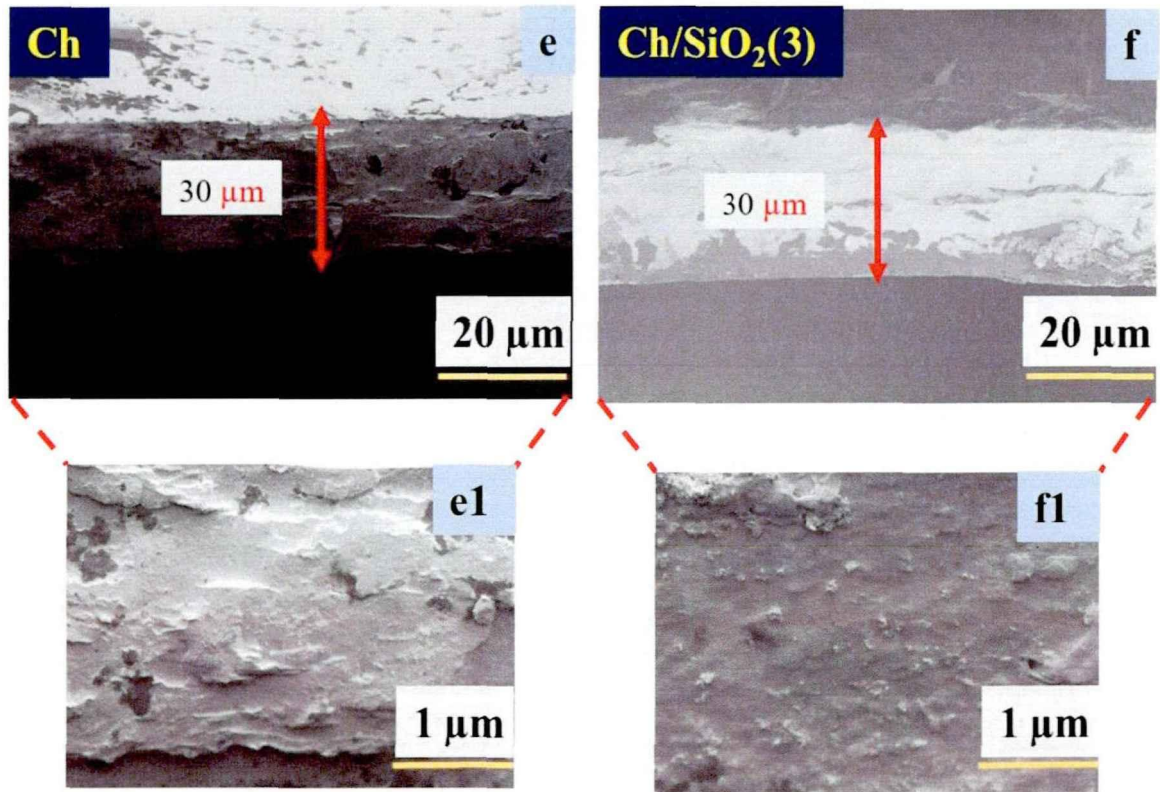
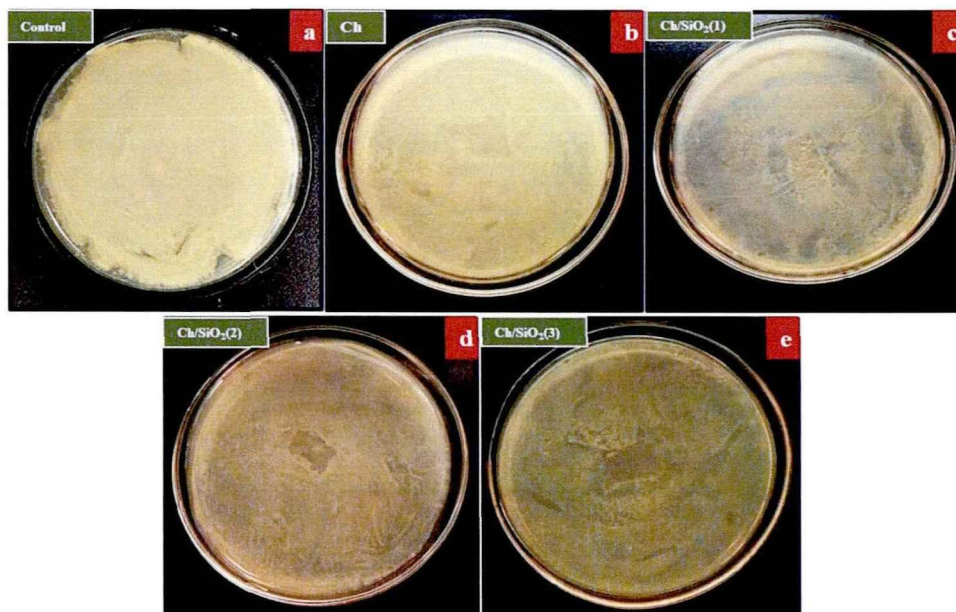


Fig. 5. 5. SEM cross-section for antifogging coating layer, e) chitosan film, f) Ch/SiO<sub>2</sub> (3). Ch/SiO<sub>2</sub> (3) film.

### 5.2.5 Antimicrobial activity

The antimicrobial properties of the coating layers were tested using *E. coli*. Large numbers of microbial colonies were found on the unmodified sample, as shown in Fig. 5. 6a, demonstrating a significant sensitivity to microbial growth. In comparison, resistance to microbial colonies began with the chitosan layer, revealing their natural antimicrobial capabilities (Fig. 5. 6b). This resistance to microorganisms improved progressively as silica concentrations rose (Fig. 5. 6(c, d, e)), which acted as a barrier against microbial growth.





**Fig. 5. 6.** Antimicrobial adhesion tests using *E. coli*. Colonial morphologies are revealed by images corresponding to (a) uncoated glass, b) Ch, c) Ch/SiO<sub>2</sub> (1), d) Ch/SiO<sub>2</sub> (2), e) Ch/SiO<sub>2</sub> (3).

## 5.2.6 Antifogging properties

### 5.2.6.1 Cold-warm fogging test

In Fig. 5. 7, the modified glasses' antifogging properties were obtained. The morphology and optical properties for coated and uncoated glass in Fig. 5. 7(a, b, c, d, e) were employed as a controller for the cold fogging experiments. After storing the samples in the refrigerator (-20 °C) for 30 min, optical images were taken immediately after transporting the pieces to the laboratory environment (25 °C and 75% humidity).



**Fig. 5. 7.** Optical microscopy and photograph pictures of composite chitosan coating layers (a, b, c, d, e) after coating (f, g, h, I, j) after the antifogging cold test. The photographic pictures in the optical images were taken after each test.

The untreated glass showed high condensation for water droplets, indicating low surface energy and antifogging performance (Fig. 5. 7f). In contrast, due to the broad spreading caused by the hydrophilicity, the condensation of water droplets diminishes with the emergence of big droplets on the chitosan layer (Fig 5. 7g).

The droplet's sizes increased dramatically with adding *MSN* to the chitosan structure (Fig. 5. 7(h, i)). The  $\text{Ch/SiO}_2$  (3), as shown in Fig. 5. 7j, has the greatest antifogging performance due to the high wettability leading to the fast-spreading and forming a continuous layer of water.

### 5.2.6.2 Hot-vapor fogging test

In addition, fogging hot test over a water bath was done at 60 °C. Then the pictures were taken by the installed camera after 30 min (Fig. 5. 8a). The results revealed that untreated glass has poor antifogging due to its restricted wettability Fig. 5. 8b1. The chitosan layer has a little improvement in fogging resistance Fig. 5. 8b2. As silica concentration increased, antifogging effectiveness improved due to enhanced surface hydrophilicity, resulting in fogging resistance (Fig. 5. 8(b3, b4, b5)). None of the previously observed discrete water forms (droplets or stains) was identified on the  $\text{Ch/SiO}_2$  (3), showing that *MSN* can be compatible with polysaccharide structure and function as an effective wetting enhancer forcing condensed water molecules to form a continuous thin film of water.

### 5.2.7 Mechanical properties

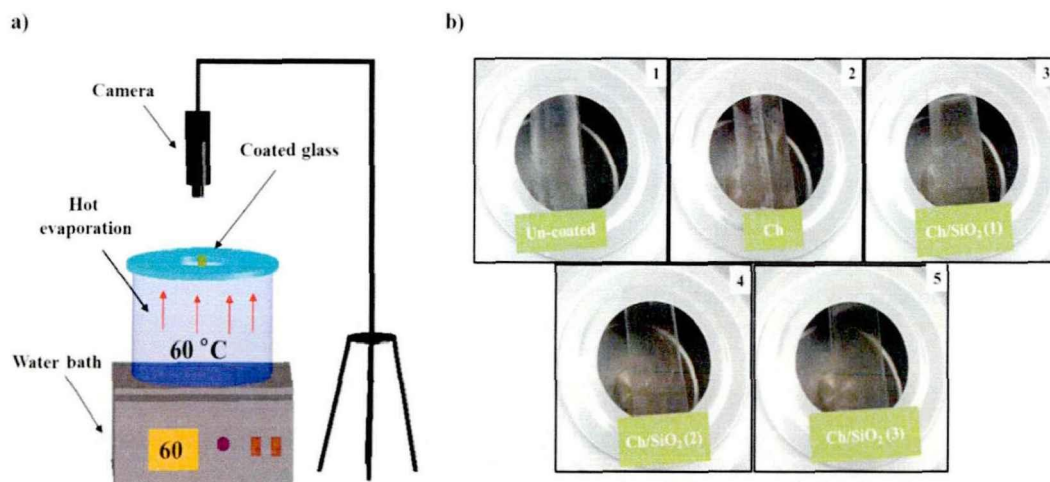


**Fig. 5. 8.** a) Diagram shows the antifogging test principle for untreated and four modified glass, b) Optical pictures after 1h antifogging hot test.

After one day of exposure to the hot-vapor test, a sandpaper test was applied for unmodified and modified glass (The sandpaper test principle is obtained in Support Information Fig. 5. 8a). Then optical microscopy was taken directly after the test (Fig. 5. 8b). The unmodified glass and the sample modified by

chitosan showed significant damage when tested (Fig. 5. 8b1) and (Fig. 5. 8b2), respectively, and gradually decreased with silica concentrations (Fig. 5. 8b(3,4)). The sample with the highest scratch resistance is Ch/SiO<sub>2</sub> (3), which showed no surface damage following the mechanical test (Fig. 5. 8b5).

### 5.2.8 NMR investigations

In Fig. (5. 9), two experiments have been done clarifying the water fractions for coating layers before and after drying, using the Inverse Laplace Transform  $T_2$  CPMG technique to understand the initial state of water components when *MSN* is introduced to chitosan structure (Fig. 5. 9a), and studying the water fractions mobility in the final stage after drying (Fig. 5. 9b). The findings showed that the fluid component has a varying effect on water fractions in the solution state (Fig. 5. 9a). Therefore, as the silica dosage rose, the intensity of bound water increased gradually, and the free and immobilized water reduced continuously. In contrast, after drying, the intensity of the free water component vanished for all samples, which may be attributed to its exclusive water-water interaction, which is responsible for its rapid mobility and evaporation Fig. 5. 9b. It is worth noticing that after drying, the bound and immobilized water peaks changed towards lower relaxation time (less than 0.5 *ms* for bound water and approximately 100 *ms* for immobilized water), which is attributable to a decrease in the humidity in the final layer. Following our prior work [88], the fitting process was performed to estimate the water fractions proportion in different relaxation regions Fig. 5. 9(c, d). The addition of *MSN* had a considerable effect on water fractions proportion in the solution state. However, the bound water proportion rose progressively as the nanoparticle dosage increased, which enhanced from 74.37% to 97.70% for Ch/SiO<sub>2</sub> (1) and Ch/SiO<sub>2</sub> (3), respectively, with reducing the other fractions due to strongly water-surface interaction and weakly water-water contact, which is well known attributed to the free and immobilized water (Fig. 5. 9c). Therefore, the fractions proportion in the solution state is a critical indicator of the final layer quality after drying.



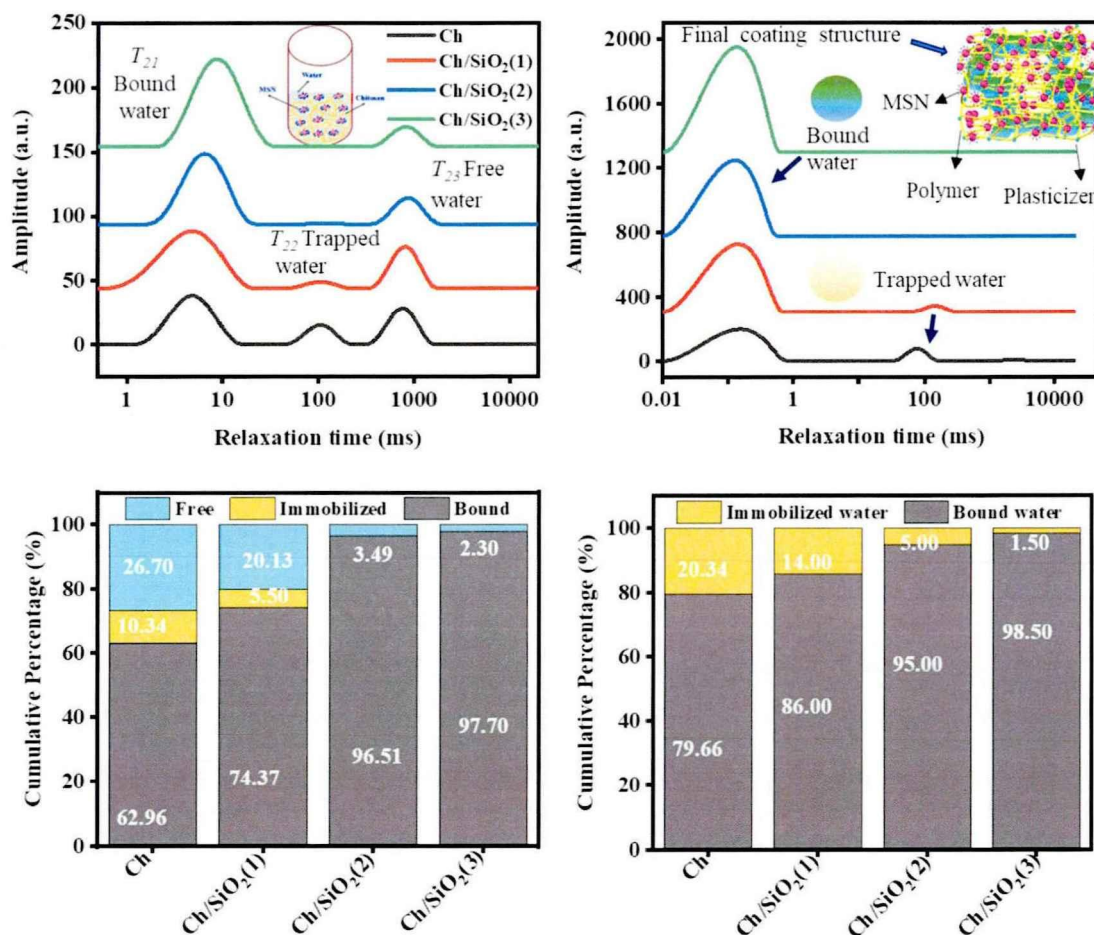


**Fig. 5. 9.** Water fraction in (a) solution state, (b) solid state, (c) the proportion of water fraction in the solution state, (d) the proportion of water fraction after drying.

As a result, *MSN* plays a vital role in enhancing the bound water layer, lowering immobilized water, reducing humidity levels, and forming a solid coating layer (Fig. 5. 9d). However, the relation between bound water fraction and antifogging/antimicrobial properties was examined in Fig. 5. 11. As previously described, the bound water fraction was estimated after fitting the original data supplied by the NMR signal. Since the condensation of water droplets on substrate surfaces is the primary cause of fogging phenomena; thus, using ImageJ software, the size and area covered by droplets have been calculated (repeated five times in the different regions, then the average was obtained) on the substrate with and without coating layer. Using uncoated glass as an example (Fig. 5. 10a), the average droplet size after the cold-warm test is 21.4  $\mu\text{m}$ , as seen in Fig. 5. 10b, with a covered area of more than 77%. However, when the bound water proportion increased (Fig. 5. 7(g, h)), the condensation area decreased progressively until a uniform layer of water was formed, as seen in the Ch/SiO<sub>2</sub>

(2) and Ch/SiO<sub>2</sub> (3) samples (Fig. 5. 7(i, j)). In this case, bound water is crucial in reducing the freezing point of water and successfully avoiding frost formation. In the case of free water, the water molecules are far from the polymer's –OH sites which behave like bulk water, whereas the intermediate water molecules are closer to the attached water molecules but do not interact directly with the polymer's –OH sites. Therefore, free and immobilized water in the coating layer rendered the frost-resistance function worthless. In addition, the area covered by microbial colonies on each plate has also been measured. Previous studies have shown that if there are too many colonies on the plate (i.e., more than 1000 colonies), they might run together and become indistinguishable from individual colonies, therefore would be difficult to count. In this situation, the dish is known as confluent, which means "too numerous to count" (TNTC) [56]. So to overcome the issue, the area covered by colonies was calculated (five times in the different regions and then averaged).

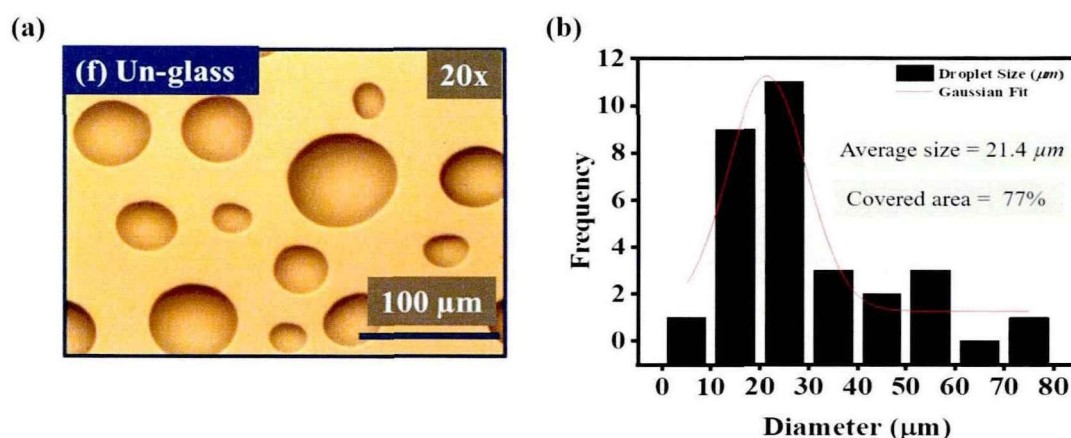


**Fig. 5. 10.** a) Optical picture for un-coated glass, b) the size and amount of condensation droplets.

As seen in Fig. 5. 11, bound water fraction also plays a critical role in preventing undesirable properties such as microbial activities. One possible explanation is that the presence of bound water molecules in nano-fluids limits the amount of free and immobilized water molecules [233], preventing hydrate formation in the final coating layer after drying. Therefore, when the proportion of bound water increased in the final layer, the suppression of microbial growth increased gradually until no microbial activity was observed in the Ch/SiO<sub>2</sub> (3) layer, indicating its high efficiency against microbial activities (Fig. 5. 6e). This is attributed to the hydroxyl groups, which produced hydrogen bonding and electrostatic attractions between MSN and water molecules ions in chitosan structure, increasing its mechanical properties since water molecules are firmly bound when they interact with the –OH groups of the polymer via hydrogen bonding [225][226]. A more MSN concentration leading to a more bound water ratio than immobilized water in chitosan structure implies that the coating layer

is more hydrophilic, with superior microbial resistance. The tightly bound water layer produces a physical and free energy barrier that inhibits the interactions between bacteria and coated layer, resulting in a significant antimicrobial effect.

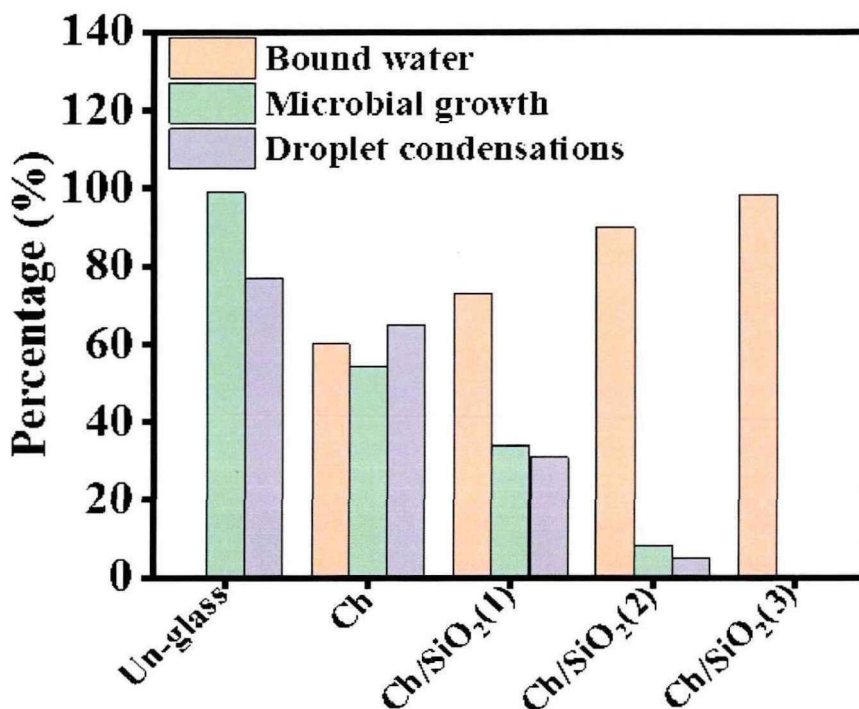


Fig. 5. 11. The effect of bound water for preventing the fogging and microbial problems

### 5.3 Conclusion

The experimental and analytical data presented above demonstrated that depending on the addition of modified silica nanoparticles (*MSN*) to chitosan structure, the increasing of bound water fraction plays a critical role in forming a robust layer against fogging/microbial activities. Using time-domain low field <sup>1</sup>H NMR spectroscopy, the spin-spin relaxation time *T*<sub>2</sub> sequence approach was used to study the influence of water fractions when the *MSN* was added to the chitosan structure in the solution state and after drying. The results show that the bound water fraction has a significant role in preventing undesirable properties such as fogging and microbial activities due to the high water-surface interaction, essential in the final layer. On the other hand, the extended life of the coating layer and the mechanical properties have also been enhanced. Experimentally, the minimal quantity of bound water necessary to prevent microbiological and fogging issues is 95% compared to the remainder of the other water fractions in the chitosan structure. This might be used as a rapid dimensionless indicator to examine

the coating composite in solution state and the quality of the final layers after drying for antifogging/antimicrobial properties, allowing researchers to determine the appropriate values for adding additives more appropriately and accurately.

## Chapter 6 Summary and Outlook

This thesis has covered surfaces modification for optical products such as polymer and glasses and their application in agriculture and other applications. In chapter 1, the idea introduces the background on polymer, and its verity uses in many applications; however, also characterized by undesirable properties such as fogging formation. In brief, fogging is always a significant problem for agricultural films due to hydrophobicity, where fog may reduce light transmission resulting in an adverse effect on the yield and quality of crops. Up to date, many reports have been disclosed in the field of antifogging on the surfaces of plastic films. Nevertheless, these methods have drawbacks, such as the cumbersome preparation process, high-cost experimental components, and toxic reagents after analyzing the existing problems related to the fogging problem of hydrophobic polymers and the limitations of commercially available LDPE-based greenhouse applications during service to achieve the objectives, adequate experimental methods, and proper materials are essential. These aspects are covered in chapter 2.

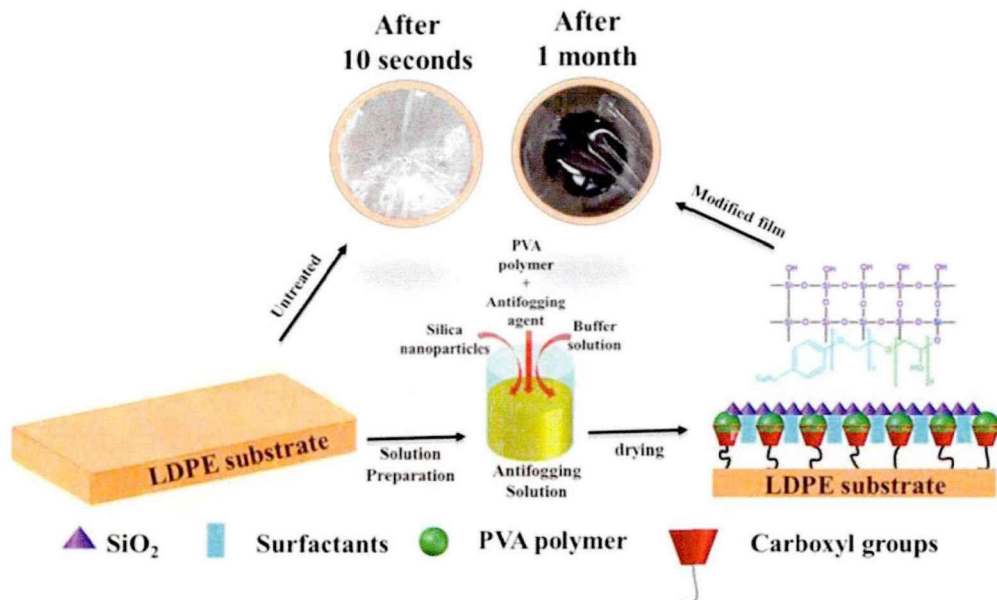


**Fig. 6. 1.** Show the super-hydrophilic layers based on PVA and surfactant on the LDPE for greenhouses applications.

In the present work, a simple and effective technique is adopted to develop a low-cost super-hydrophilic layer based on PVA for coating LDPE films with excellent fogging resistance properties and extraordinary light transmittance Fig. 5. 1. Corona discharge treatment is applied to play a pivotal role in the stability of the coating



layer by creating a fertile environment for solid chemical bonding on the surface of the LDPE film. By adding TBS buffer solution with the surfactant, the overall hydrophilicity performance of the film becomes enhanced. Further, adding silica nanoparticles by different concentrations to the mixture solution increases the wetting and coating stability. The time-domain NMR is employed to clarify the influence of surface free energy on the formation of silica aggregations. The results show that the increase in the bound water fraction promotes the formation of homogeneously distributed silica aggregates into particles dispersed on the surface. The described technique results in the homogeneous deposition of the antifogging coating layer on the surface of LDPE film, which becomes super-hydrophilic. Therefore, this chapter gave a key in overcoming the fogging problem for agriculture greenhouses, which is critical for the agricultural sector and is one essential direction for preserving humanity.

The inhomogeneous coffee ring effect phenomenon is among the most significant and dangerous issues encountered during the coating process. This concept is described in Chapter 3. A ring-shaped structure forms around the circumference of a droplet of liquid containing suspended particles as it dries on a solid surface.

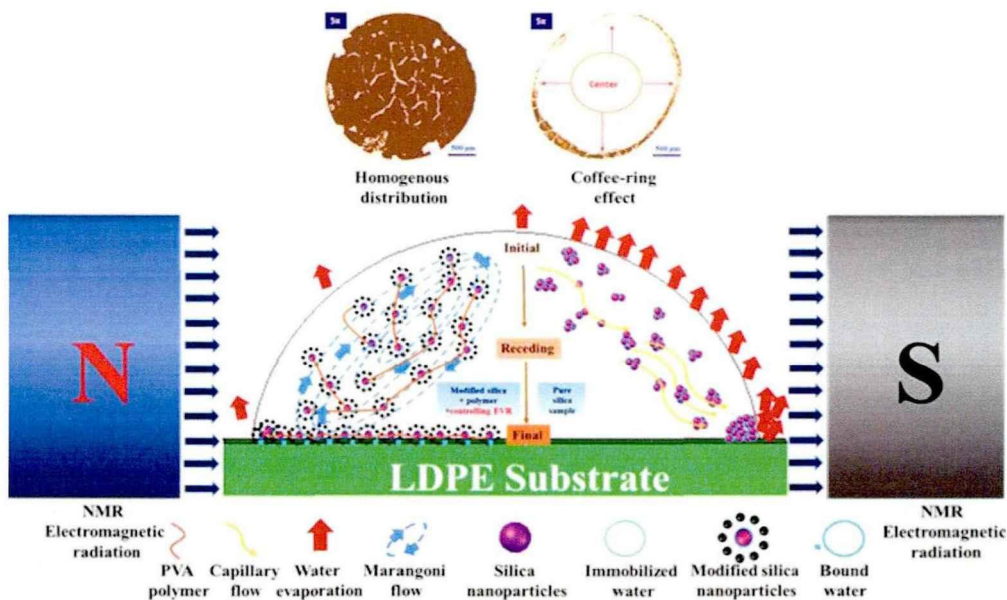


**Fig. 6. 2.** Show the differences between capillary and Marangoni flow and its effect on the silica nanoparticles distribution during evaporation.

In everyday life, this phenomenon may be seen when liquid droplets carrying suspended particles evaporate, such as ring stains left by dropped coffee drips. However, it is unsuitable for applications that need



homogeneous particle deposition on surfaces, such as agricultural films and optical applications. In the work, two times scale ( $t_F$ ,  $t_B$ ) was adopted, using the low field (LF)-NMR to demonstrate that slowing down the evaporation rate  $J$ , enhances the Marangoni flow and disturbing the capillary flow, which aids in decreasing the coffee-ring effect (CRE) generation from evaporated colloidal droplets, even in the absence of additives (surfactant or polymer) Fig. 5. 2. In addition, the *in-situ*  $T_2$  Carr-Purcell-Meiboom-Gill sequence (CPMG) approach studied the effect of water fractions (free, trapped, and bound water) on the formation of the CRE on the hydrophobic low-density polyethylene (LDPE) surface to understand the mechanism of the CRE formation and uniform distribution phenomena of silica nanoparticles, based on changes in water fractions during evaporation. Our findings demonstrated that the critical role of bound water and other fractions determines coffee rings formation's performance or homogenous distribution for colloidal droplets during evaporation, relying on the effective additives and managing the  $J$ . This could be used as a dimensionless indicator to investigate particle mobility in solution and during evaporation to improve silica dispersion throughout the coating process, allowing researchers to more accurately and appropriately determine the appropriate values for adding additives and the best evaporation conditions.

Due to the apparent pandemic caused by (COVID-19), it is necessary to wear goggles when in touch with patients to protect the eyes from potentially dangerous illnesses such as severe acute respiratory syndrome coronavirus infection. This is the problem and its solution discussed in chapter 4. Fogging/microbial goggles are crucial in inpatient care because they impede vision and diminish productivity. As a result, it is necessary to provide an antifogging/antimicrobial layer Fig. 5. 3. This study used a simple one-pot technique to create an antifogging and antibacterial composite coatings layer of chitosan/silica (Ch/SiO<sub>2</sub>). The effect of adding modified silica nanoparticles (*MSN*) to the chitosan structure was examined using solid-state low field nuclear magnetic resonance (LF-NMR). The  $T_2$  Carr-Purcell-Meiboom-Gill (CPMG) sequence approach was used to assess the antifogging/antimicrobial capabilities of the coating layers based on the mobility of the principal water fractions in two states (solution-state and solid-state). The solution's hydrogen bonds and electrostatic attractions formed by *MSN* (water molecules/hydronium ions) result in a more excellent bound water ratio in the final layers after drying, increasing antifogging and antibacterial characteristics while maintaining mechanical performance. The study in this chapter could be used as a rapid dimensionless indicator to examine the coating composite in solution and the quality of the final layers after drying for antifogging/antimicrobial properties, allowing researchers to more accurately and appropriately determine the appropriate values for adding additives. This dual functional coating will be widely employed in optical devices for medical diagnostics, healthcare monitoring, and other applications.

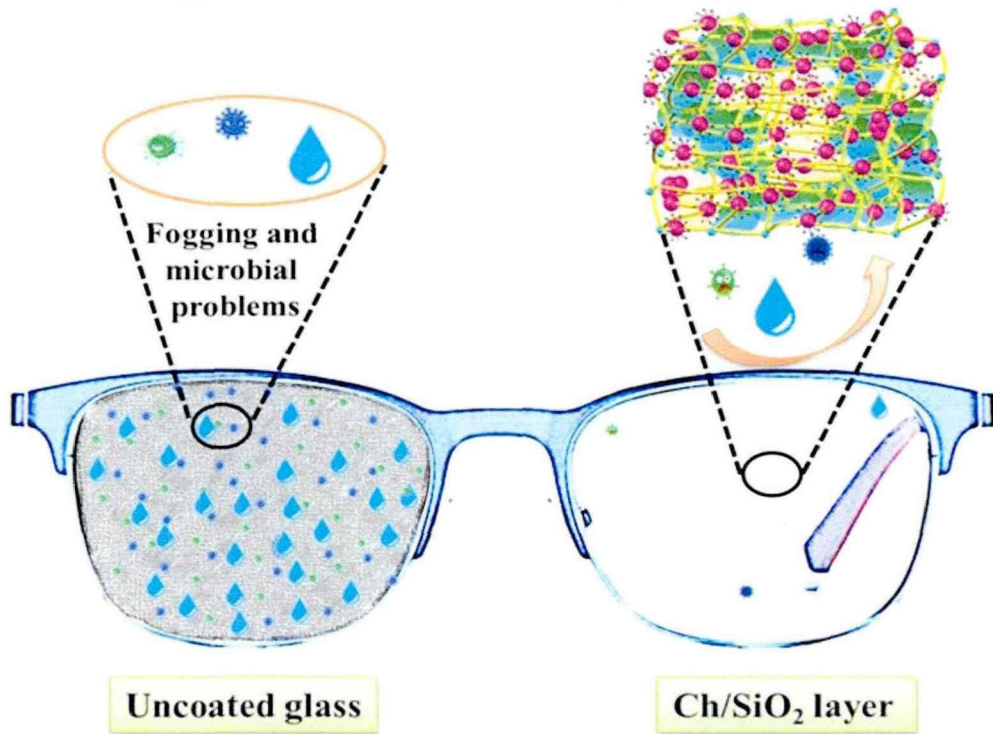


Fig. 6. 3. Show the effect of chitosan/silica nanoparticles coating on preventing microbial and fogging problems.

## **Acknowledgements**

The thesis is the outcome of the work which continued for four years in **Prof. Liangbin Li's** research group. Undescribed thanks to professor Li for selecting me for this chance and being one of his group members. It was a great honor to be my supervisor for four years without boring and gaining more professional and academic research skills. The thanks cannot describe in words for Ass. **Prof. Wei Chen** always carries about us day by day and point by point to build a strong bridge of knowledge. Many thanks to him for being our **Supervisor, Friend, and Brother** for forming an excellent environment for science. Also, many thanks to the **Softmatter Group Members**, including all teachers, college students, and supporting staff, for having provided a conducive research environment during my whole study period. I owe too much to my family, my fiancé **Rayyan** for the care, patience, sacrifice, assistance, and motivation that brought about this success. I cannot also forget to thank all my **Parents** sincerely, my sister **Saher**, and my **family members**.

Without their endless efforts and support, I should not have become who I am today. I am grateful to all my other friends, countrymates, and others of different nationalities. We shared social life in China through various sports activities, cultural events, etc. I also thank any other individual who contributed in one or another to realize this thesis. I sincerely acknowledge the **University of Science and Technology of China** for admitting me to its excellent research environment through the National Synchrotron Radiation Laboratory. This work would not have been possible without financial support. I thank the Chinese Scholarship Council (**CSC**) for funding my studies by awarding me a scholarship. I would also like to thank the Republic of Sudan through the Ministry of Public Service and Labor for allowing me a study leave to carry out the completed doctoral program.

## List of Publications

- **B. Mansoor**, et al. Nanoparticle deposition pattern during colloidal droplet evaporation as in-situ investigated by Low-Field NMR: The critical role of bound water. *Journal of Colloid and Interface Science*, 2022, 613, 709-719. (IF: 8.1).
- **B. Mansoor**, et al. Polyvinyl alcohol (PVA) based super-hydrophilic anti-fogging layer assisted by plasma spraying for low-density polyethylene (LDPE) greenhouse films. *Progress in organic coatings*, 2021, 159, 106412. (IF: 5.2).
- D.M.D. Babiker, C. Wan, **B. Mansoor**, et al. Superior lithium battery separator with extraordinary electrochemical performance and thermal stability based on hybrid UHMWPE/SiO<sub>2</sub> nanocomposites via the scalable biaxial stretching process. *Composites Part B: Engineering*, 2021, 211,108658. (IF: 9.078).
- **B.Mansoor** and W. Chen, Dual-functional highly efficient antifogging/antimicrobial biopolymer coating for glass applications. *Carbohydrate Polymers*, 2022. (Under revision). (IF: 9.381).
- **B.Mansoor** Improvement on food shelf-life based on modified gum arabic layer coating 2022. (Under processing).

---

## References

- [1] Nabi Saheb D, Jog J P. Natural fiber polymer composites: A review[J/OL]. *Advances in Polymer Technology*, 1999, 18(4): 351-363.
- [2] Fleming R J. An introduction to polymer physics[J/OL]. *Physicist*, 2003, 40(1): 26.
- [3] Bolgar, M., Groeger, J., Hubball, J., & Meronek, S. *Handbook for the Chemical Analysis of Plastic and Polymer Additives*[J]. CRC Press, 2007, 504: 9780429140204.
- [4] Sanchez I C, Lacombe R H. Statistical thermodynamics of polymer solutions[ J/OL]. *Macromolecules*, 1978, 11(6): 1145-1156.
- [5] Koller M, Braunegg G. Advanced approaches to produce polyhydroxyalkanoate (PHA) biopolyesters in a sustainable and economic fashion[J/OL]. *The EuroBiotech Journal*, 2018, 2(2): 89-103.
- [6] Ebbing D, Gammon SD . *General Chemistry*[J]. Cengage Learning. 2016, 978-1-305-88729-9..
- [7] A.DemaidV.SpeddingJ.Zucker. Classification of plastics[J]. *Artificial Intelligence in Engineering*. 1996, 9-20, 10.
- [8] Kent R. *Polymers and the Periodic Table: Recent Developments in Inorganic Polymer Science*[J]. *Plastics Consultancy Network*. 2008-07-03
- [9] Online resource 1: [www.plasticseurope.org](http://www.plasticseurope.org). last access [J], April 6th, 2018.
- [10] Annual-per-capita-production-of-plastic-by-region [J]. 2021.
- [11] Shent H, Pugh R J, Forssberg E. A review of plastics waste recycling and the flotation of plastics[J/OL]. *Resources, Conservation and Recycling*, 1999, 25(2): 85-109.
- [12] Sauter D W, Taoufik M, Boisson C. Polyolefins, a success story[J/OL]. *Polymers*, 2017, 9(6): 1-13.
- [13] A.LustigerR.L.Markham. Importance of tie molecules in preventing polyethylene fracture under long-term loading conditions[J]. *Polymer*, 1983, 1647-1654, 24.
- [14] Yan Changrong<sup>1</sup>, Dr. He Wenqing<sup>1</sup>. Plastic-film mulch in chinese agriculture: importance and problems[J]. *World Agriculture*, 2014, Vol. 4 (2), 32-36.
- [15] Briassoulis D, Schettini E. Analysis and design of low-density polyethylene greenhouse films[J/OL]. *Biosystems Engineering*, 2003, 84(3): 303-314.
- [16] Espi E, Salmerón A, Fontecha A, et al. Plastic films for agricultural applications[J/OL]. *Journal of Plastic Film and Sheeting*, 2006, 22(2): 85-102.
- [17] Espi E, Salmerón A, Fontecha A, et al. The effect of different variables on the accelerated and natural weathering of agricultural films[J/OL]. *Polymer Degradation and Stability*, 2007, 92(12): 2150-2154.
- [18] Martín-Closas L, Costa J, Pelacho A M. Soil degradable bioplastics for a sustainable modern agriculture

## References

- [M]. Soil Degradable Bioplastics for a Sustainable Modern Agriculture.2017, 978-3-662-54128-9.
- [19] Gugumus, F.L. Greenhouse film stabilization: Handbook of polymer degradation[J]. IEEE Electrical Insulation Magazine, 2001, 10016.
- [20] Garnaud, J.C. Agricultural and horticultural applications of polymers[J]. Rapra Technology Ltd., Pergamon Press, Oxford, Shawbury, UK. 1988, 489-503.
- [21] Brown, R.P. Polymers in agriculture and horticulture[J]. Rapra Technology Ltd., Shawbury, UK. 2004, 31-44.
- [22] Jouet, J.P. Plastics in the world, plasticulture[J]. 2004, 120: 108–126.
- [23] Jouet, J.P. The situation of plasticulture in the world, plasticulture J]. 2004, 123: 48–57.
- [24] Jiang, W., Qu, D., Mu, D. and Wang, L.R. China's energy-saving greenhouses[J], *Chronica Horticulturae*. 2019, 44(1): 15–17.
- [25] Katan, J. and DeVay, J.E. Soil solarization, CRC Press, Boca Raton, Florida, USA[J]. 1991, 42-903.
- [26] Castilla, N. Invernaderos de Pla'stico. Tecnología y manejo, Mundi-Prensa, Madrid[J]. 2004, 35-762.
- [27] Di'az, T., Espi', E., Fontecha, A. Los filmes pla'sticos en ia produccio'n agri'cola, Repsol YPF, Mundi-Prensa, Madrid [J]. 2001, 33-607.
- [28] Kyrikou I, Briassoulis D. Biodegradation of agricultural plastic films: A critical review[J/OL]. *Journal of Polymers and the Environment*, 2007, 15(2): 125-150.
- [29] Dilara P A, Briassoulis D. Standard testing methods for mechanical properties and degradation of low density polyethylene (LDPE) films used as greenhouse covering materials: A critical evaluation[J/OL]. *Polymer Testing*, 1998, 17(8): 549-585.
- [30] Babaghayou M I, Mourad A H I, Lorenzo V, et al. Anisotropy evolution of low density polyethylene greenhouse covering films during their service life[J/OL]. *Polymer Testing*, 2018, 66: 146-154.
- [31] Briassoulis D, Aristopoulou A, Bonora M, et al. Degradation characterisation of agricultural low-density polyethylene films [J/OL]. *Biosystems Engineering*, 2004, 88(2): 131-143.
- [32] Briassoulis D. Mechanical behaviour of biodegradable agricultural films under real field conditions [J/OL]. *Polymer Degradation and Stability*, 2006, 91(6): 1256-1272.
- [33] Briassoulis D. Analysis of the mechanical and degradation performances of optimised agricultural biodegradable films[J/OL]. *Polymer Degradation and Stability*, 2007, 92(6): 1115-1132.
- [34] Accorsi R, Cascini A, Cholette S, et al. Economic and environmental assessment of reusable plastic containers: A food catering supply chain case study[J/OL]. *International Journal of Production Economics*, 2014, 152: 88-101.
- [35] Pack M, Mehta K. Design of affordable greenhouses for East Africa[J/OL]. *Global Humanitarian*



## References

---

- Technology Conference, 2012: 104-110.
- [36] Briassoulis D, Babou E, Hiskakis M, et al. Review, mapping and analysis of the agricultural plastic waste generation and consolidation in Europe[J/OL]. *Waste Management and Research*, 2013, 31(12): 1262-1278.
- [37] Briassoulis D. The effects of tensile stress and the agrochemical vapam on the ageing of low density polyethylene (LDPE) agricultural films. Part I. Mechanical behaviour[J/OL]. *Polymer Degradation and Stability*, 2005, 88(3): 489-503.
- [38] Office of the Federal Coordinator for Meteorology, Present Weather, in: *Federal Meteorological Handbook No. 1*, chap. 8, sections[J]. *Space Weather*, 2015, 8.1–8.2.
- [39] Wylin, F. Antifogging additives, in: *Plastics additives handbook*, Zweifel, H. (Ed.), 5th ed., Hanser Publications: Munich [J]. EW Flick, 2001, 108-130.
- [40] Wagner, P., Anti-Fog additives give clear advantage, anti-fog additives give clear advantage[J]. *Plastics Additives and Compounding*. 3(11), 18, 2001.
- [41] Young, T. An essay on the cohesion of fluids[J]. *Philos. Trans. R. Soc. Lond.*, 95, 65, 1805.
- [42] Martin S, Brown P S, Bhushan B. Fabrication techniques for bioinspired, mechanically-durable, superliquiphobic surfaces for water, oil, and surfactant repellency[J/OL]. *Advances in Colloid and Interface Science*, 2017, 241: 1-23.
- [43] Teitel M, Vitoshkin H, Geola F, et al. Greenhouse and screenhouse cover materials: Literature review and industry perspective[J/OL]. *Acta Horticulturae*, 2018, 1227: 31-44.
- [44] De Abreu D A P, Cruz J M, Losada P P. Active and intelligent packaging for the food industry[J/OL]. *Food Reviews International*, 2012, 28(2): 146-187.
- [45] Yang Z, Peng H, Wang W, Et Al. Crystallization behavior of poly( $\epsilon$ -caprolactone)/layered double hydroxide nanocomposites[J/OL]. *Journal of Applied Polymer Science*, 2010, 116(5): 2658-2667.
- [46] Ge X, Chu M, Qu L, Et Al. Long-lasting intrinsic polyethylene antifogging films generated by incorporating SiO<sub>2</sub> nanoparticles into covalently grafted antifog agents[J/OL]. *Journal of Macromolecular Science, Part A: Pure and Applied Chemistry*, 2020, 57(12): 826-836.
- [47] LI Y, FANG X, WANG Y, et al. Highly transparent and water-enabled healable antifogging and frost-resisting films based on poly(vinyl alcohol)-Nafion complexes[J/OL]. *Chemistry of Materials*, 2016, 28(19): 6975-6984.
- [48] Krog, N., Food emulsifiers – chemical structure and physico-chemical properties[J]. *Danisco Technical Paper TP 18-Ie*, Danisco A/S, 2007.
- [49] Mansoor B, Iqbal O, Claude J, et al. Polyvinyl alcohol ( PVA ) based super-hydrophilic anti-fogging

## References

- layer assisted by plasma spraying for low density polyethylene ( LDPE ) greenhouse films[J/OL]. *Progress in Organic Coatings*, 2021, 159(May): 1064-12.
- [50] Liewchirakorn P, Suthisamphat P, Chinsirikul W, et al. Low haze and antifog performance of 2-layer poly(lactic acid) based films[J/OL]. *Key Engineering Materials*, 2017, 751 KEM: 326-331.
- [51] S. Oglesby, Jr. and G. B. Nichols, *Electrostatic precipitation*[J]. New York: Marcel Dekker. 1978.
- [52] Howarth, G A; Manock, H L. 'Water-borne polyurethane dispersions and their use in functional coatings' [J]. *Surface Coatings International*, 80 (7): 324–328.
- [53] Howarth G.A. Synthesis of a legislation compliant corrosion protection coating system based on urethane, oxazolidine and waterborne epoxy technology[J]. Imperial College London, 1997.
- [54] Yin Z, Tian B, Zhu Q, et al. Characterization and application of PVDF and its copolymer films prepared by spin-coating and langmuir-blodgett method[J/OL]. *Polymers*, 2019, 11(12).
- [55] Sahu N, Parija B, Panigrahi S. Fundamental understanding and modeling of spin coating process: A review[J/OL]. *Indian Journal of Physics*, 2009, 83(4): 493-502.
- [56] Schneller T, Waser R, Kosec M, et al. Theodor Schneller rainer waser marija kosec · David Payne[M]. 2013.
- [57] Cao, G.; Wang, Y. *Nanostructures and nanomaterials: synthesis: properties and applications*[J]. World Scientific: Singapore, 2011.
- [58] Schmid, G. *Nanoparticles: From Theory to Application*[J]. WileyVCH: Weinheim, Germany. 2010.
- [59] Suh, W. H.; Suh, Y. H.; Stucky, G. D. Multifunctional nanosystems at the interface of physical and life sciences[J]. 2009, 4, 27–36.
- [60] Leszczynski, J. Nano Meets Bio at the Interface[J]. *Nat. Nanotechnol.* 2010, 5, 633–634.
- [61] Lynch, I.; Cedervall, T.; Lundqvist, M .; Lago, C. C.; Linse, S.; Dawson, K. A. The nanoparticle-protein complex as a biological entity; a complex fluids and surface science challenge for the 21st century[J]. *Adv. Colloid Interface Sci.* 2007, 134–135, 167–17.
- [62] Kumar, S.; Aswal, V. K. Tuning of nanoparticle-surfactant interactions in aqueous system[J]. *J. Phys.: Condens Matter*, 2011, 23, 035101.
- [63] Zhang, R.; Somasundaran, P. Advances in adsorption of surfactants and their mixtures at solid/solution interfaces [J]. *Adv. Colloid Interface Sci.* 2006, 123–126, 213–229.
- [64] Lundqvist, M.; Stigler, J.; Elia, G.; Lynch, I.; Cedervall, T.; Dawson, K. A. Nanoparticle size and surface properties determine the protein corona with possible implications for biological impacts[J]. *Proc. Natl. Acad. Sci. U.S.A.* 2008, 105, 14265–14270.
- [65] Qi, L.; Fresnais, J.; Berret, J.-F.; Castaing, J.-C.; Destremaut, F.; Salmon, J.-B.; Cousin, F.; Chapel, J.-P.

## References

- Influence of the formulation process in electrostatic assembly of nanoparticles and macromolecules in aqueous solution: the interaction pathway[J]. *The Journal of Physical Chemistry*, 2010, 114, 39, 16373–16381.
- [66] Lugo, D.; Oberdisse, J.; Karg, M.; Schweins, R.; Findenegg, G. H. Surface aggregate structure of nonionic surfactants on silica nanoparticles[J]. *Soft Matter* 2009, 5, 2928–2936.
- [67] Paria, S.; Khilar, K. C. A review on experimental studies of surfactant adsorption at the hydrophilic solid – water interface[J]. *Adv. Colloid Interface Sci.* 2004, 110, 75–95.
- [68] James K.FerriKathleen J.Stebe. Which surfactants reduce surface tension faster? A scaling argument for diffusion-controlled adsorption[J]. *Adv. Colloid Interface Sci.* 2000, 61-97, 85.
- [69] El-Sherif, H. M.; Nasser, A. M.; Hussin, A. I.; Abd El-Wahab, H.; Ghazy, M. B. M.; Elsayed, A. E.. Nano emulsion binders for paper coating synthesis and application[J]. *J. Macromolecul. Sci. Part A.*, 2017, 54(5), 271–287.
- [70] Farzad, H.; Najafi, F.; Bengisu, M.; Yilmaz, E.; Hadavand, B. S. Synthesis and characterization of aliphatic tri-functional oligomeric urethane methacrylate used for UV-curable aluminum pigmented coatings[J]. *J. Macromolecul. Sci. Part A.*, 2013, 50(5), 504.
- [71] Wang, B.; Wilkes, G. L. Novel hybrid inorganic-organic abrasionresistant coatings prepared by a sol-gel process[J]. *J. Macromolecul. Sci. Part A.*, 1994, 31(2), 249–260.
- [72] Yabuki, A.; Tanabe, S.; Fathona, I. W. Self-healing polymer coating with the microfibers of superabsorbent polymers provides corrosion inhibition in carbon steel. *Surf. Coat[J]. Technol.*, 2017, 40(5), 304.
- [73] Gruber, P. R.; Kolstad, J. J.; Ryan, C. M.; Hall, E. S.; Conn, R. S. E.; Cargill, Incorporated. Paper having a melt-stable lactide polymer coating and process for manufacture thereof[J]. U.S. Patent. 1995 5,475,080.
- [74] Kinlen, P. J.; Ding, Y.; Silverman, D. C. Corrosion protection of mild steel using sulfonic and phosphonic acid-doped polyanilines[J]. *Corrosion*, 2002, 58(6), 490–497.
- [75] Martins, J. T.; Cerqueira, M. A.; Vicente, A. A.. Influence of a-tocopherol on physicochemical properties of chitosan-based films[ J]. *Food Hydrocolloids*, 2012, 27(1), 220–227.
- [76] Larson, C.; Smith, J. R.; Armstrong, G. J. Current research on surface finishing and coatings for aerospace bodies and structures—a review[J]. *Transactions of the IMF*, 2013, 91(3), 120–132.
- [77] Pritchett, J. W. One-component revision of failed hip resurfacing from adverse reaction to metal wear debris [J]. *The Journal of arthroplasty*, 2014, 29(1), 219–224.
- [78] Whitbourne, R. J.; Zhang, X.; Sts Biopolymers, Inc. Adherent, flexible hydrogel and medicated coatings

## References

- [J]. U.S. Patent 6,110,483 2000.
- [79] Chang, W. H.; Dowbenko, R.; Hartman, M. E.; Porter Jr, S., PPG Industries, Inc. Coating compositions composed of hydroxyfunctional polymers or copolymers and alkoxy silanes[J]. U.S. Patent. 1978, 4,093,673.
- [80] Meng, Y.; Gu, D.; Zhang, F.; Shi, Y.; Cheng, L.; Feng, D.; Wu, Z.; Chen, Z.; Wan, Y.; Stein, A.; Zhao, D.. A family of highly ordered mesoporous polymer resin and carbon structures from organic; organic self-assembly[J]. Chem. Mater., 2006, 18(18), 4447–4464.
- [81] Zhang, C.; Hankett, J.; Chen, Z.. Molecular level understanding of adhesion mechanisms at the epoxy/polymer interfaces[J]. ACS Appl. Mater. Interfac., 2012, 4(7), 3730–3737.
- [82] Sathyanarayana, M. N.; Yaseen, M.. Role of promoters in improving adhesions of organic coatings to a substrate[J]. Prog. Org. Coat., 1995, 26(2-4), 275–313.
- [83] Shabani-Nooshabadi, M.; Ghoreishi, S. M.; Behpour, M. Direct electrosynthesis of polyaniline-montmorillonite nanocomposite coatings on aluminum alloy 3004 and their corrosion protection performance[J]. Corros. Sci., 2011, 53(9), 3035–3042.
- [84] Piromruean, P.; Kongparakul, S.; Prasassarakich, P. Synthesis of polyaniline/montmorillonite nanocomposites with an enhanced anticorrosive performance[J]. Prog. Org. Coat., 2014, 77(3), 691–700.
- [85] Caruso, R. A.; Antonietti, M.; Giersig, M.; Hentze, H. P.; Jia, J.. Modification of TiO<sub>2</sub> network structures using a polymer gel coating technique[J]. Chem. Mater., 2001, 13(3), 1114–1123.
- [86] Zhao H, Zhang Q, Xia Z, et al. Elucidation of the relationships of structure-process-property for different ethylene/ $\alpha$ -olefin copolymers during film blowing: An in-situ synchrotron radiation X-ray scattering study[J/OL]. Polymer Testing, 2020, 85-2019.
- [87] Zhang Q, Li L, Su F, et al. From molecular entanglement network to crystal-cross-linked network and crystal scaffold during film blowing of polyethylene: an in situ synchrotron radiation small- and wide-angle x-ray scattering study[J/OL]. Macromolecules, 2018, 51(11): 4350-4362.
- [88] Mansoor B, Chen W. Nanoparticle deposition pattern during colloidal droplet evaporation as in-situ investigated by Low-Field NMR: The critical role of bound water[J/OL]. Journal of Colloid and Interface Science, 2022, 613: 709-719.
- [89] Cai M J, Li Q Q, Chen X M. Synthesis, surface Activity, and Antifogging Property of Triethanolamine Monolaurate Ester[J/OL]. Chinese Journal of Chemical Physics, 2015, 28(2): 223-229.
- [90] Durán I R, Laroche G. Current trends, challenges, and perspectives of anti-fogging technology: Surface and material design, fabrication strategies, and beyond[J/OL]. Progress in Materials Science, 2019, 99: 106-186.

## References

- [91] Sason E, Kolitz-Domb M, Chill J H, et al. Engineering of durable antifog thin coatings on plastic films by uv-curing of proteinoid prepolymers with peg-diacrylate monomers[J/OL]. ACS Omega, 2019, 4(5): 9352-9360.
- [92] Li C, Li X, Tao C, Et al. Amphiphilic antifogging/anti-icing coatings containing poss-pdmaema-b-psbma [J/OL]. ACS Applied Materials and Interfaces, 2017, 9(27): 22959-22969.
- [93] Marcondes W, Henrique R, Martins D, et al. Fast-forward approach of time-domain NMR relaxometry for solid-state chemistry of chitosan[J/OL]. 2021, 256.
- [94] Chen F, Chen C, Zhao D, et al. On-line monitoring of the sol-gel transition temperature of thermosensitive chitosan /  $\beta$ -glycerophosphate hydrogels by low field NMR[J/OL]. Carbohydrate Polymers, 2020, 116196.
- [95] Characterization of moisture migration of beef during refrigeration storage by low-field NMR and its relationship to beef quality[M]. 2020, 1940-1948.
- [96] Chen Y, Dong H, Li J, Et Al. Evaluation of a nondestructive nmr and mri method for monitoring the drying process of gastrodia elata blume[J/OL]. Molecules. 2019, 24(2).
- [97] Wang H, Wang R, Song Y, et al. A fast and non-destructive LF-NMR and MRI method to discriminate adulterated shrimp [J/OL]. Journal of Food Measurement and Characterization, 2018, 12(2): 1340-1349.
- [98] Yang S, Liu X, Jin Y, et al. Water Dynamics in Egg White Peptide, Asp-His-Thr-Lys-Glu, Powder Monitored by Dynamic Vapor Sorption and LF-NMR[J/OL]. Journal of Agricultural and Food Chemistry. 2016, 64(10): 2153-2161.
- [99] Li T, Tu C, Rui X, Et Al. Study of water dynamics in the soaking, steaming, and solid-state fermentation of glutinous rice by LF-NMR: A novel monitoring approach[J/OL]. Journal of Agricultural and Food Chemistry. 2015, 63(12): 3261-3270.
- [100] Hansen C L, Thybo A K, Bertram H C, et al. Determination of dry matter content in potato tubers by low-field nuclear magnetic resonance (LF-NMR)[J/OL]. Journal of Agricultural and Food Chemistry. 2010, 58(19): 10300-10304.
- [101] Tian B, Xu D, Cheng J, Et Al. Chitosan-silica with hops  $\beta$ -acids added films as prospective food packaging materials: Preparation, characterization, and properties[J/OL]. Carbohydrate Polymers. 2021, 118457.
- [102] Prevo B G, Kuncicky D M, Velez O D. Engineered deposition of coatings from nano- and micro-particles: A brief review of convective assembly at high volume fraction[J/OL]. Colloids and Surfaces A: Physicochemical and Engineering Aspects. 2007, 311(1-3): 2-10.
- [103] Still T, Yunker P J, Yodh A G. Surfactant-induced Marangoni eddies alter the coffee-rings of evaporating

## References

---

- colloidal drops[J/OL]. *Langmuir*. 2012, 4984-4988.
- [104] Riau A K, Mondal D, Setiawan M, et al. Functionalization of the polymeric surface with bioceramic nanoparticles via a novel, nonthermal dip coating method[J/OL]. *ACS Applied Materials and Interfaces*. 2016, 8(51): 35565-35577.
- [105] Jamison J A, Krueger K M, Yavuz C T, et al. Size-dependent sedimentation properties of nanocrystals [J/OL]. *ACS Nano*. 2008, 2(2): 311-319.
- [106] Makamba H, Hsieh Y Y, Sung W C, et al. Stable permanently hydrophilic protein-resistant thin-film coatings on poly(dimethylsiloxane) substrates by electrostatic self-assembly and chemical cross-linking [J/OL]. *Analytical Chemistry*. 2005, 77(13): 3971-3978.
- [107] Chen K, Stoianov S V., Bangerter J, Et Al. Restricted meniscus convective self-assembly[J/OL]. *Journal of Colloid and Interface Science*. 2010, 344(2): 315-320.
- [108] Yunker P J, Still T, Lohr M A, et al. Suppression of the coffee-ring effect by shape-dependent capillary interactions[J/OL]. *Nature*, 2011, 476(7360): 308-311.
- [109] Tan H, Wooh S, Butt H J, et al. Porous supraparticle assembly through self-lubricating evaporating colloidal ouzo drops[J/OL]. *Nature Communications*, 2019, 10(1).
- [110] Shen X, Ho C M, Wong T S. Minimal size of coffee ring structure[J/OL]. *Journal of Physical Chemistry B*, 2010, 114(16): 5269-5274.
- [111] Sangani A S, Lu C, Su K, et al. Capillary force on particles near a drop edge resting on a substrate and a criterion for contact line pinning[J/OL]. *Physical Review E - Statistical, Nonlinear, and Soft Matter Physics*, 2009, 80(1): 1-15.
- [112] Seo C, Jang D, Chae J, et al. Altering the coffee-ring effect by adding a surfactant-like viscous polymer solution[J/OL]. *Scientific Reports*, 2017, 7(1): 1-9.
- [113] DU F, ZHANG L, SHEN W. Controllable dried patterns of colloidal drops [J/OL]. *Journal of Colloid and Interface Science*, 2021, 606: 758-767.
- [114] Deegan R D, Bakajin O, Dupont T F, et al. Capillary flow as the cause of ring stains from dried liquid drops[J/OL]. *Nature*. 1997, 389(6653): 827-829.
- [115] Mampallil D, Eral H B. A review on suppression and utilization of the coffee-ring effect [J/OL]. *Advances in Colloid and Interface Science*, 2018, 252: 38-54.
- [116] Parsa M, Harmand S, Sefiane K, et al. Effect of substrate temperature on pattern formation of nanoparticles from volatile drops[J/OL]. *Langmuir*. 2015, 31(11): 3354-3367.
- [117] Li Y F, Sheng Y J, Tsao H K. Evaporation stains: Suppressing the coffee-ring effect by contact angle hysteresis[J/OL]. *Langmuir*. 2013, 29(25): 7802-7811.



## References

---

- [118] Man X, Doi M. Ring to mountain transition in deposition pattern of drying droplets[J/OL]. *Physical Review Letters*. 2016, 116(6): 1-5.
- [119] Man X, Doi M. Vapor-induced motion of liquid droplets on an inert substrate[J/OL]. *Physical Review Letters*. 2017, 119(4): 1-5.
- [120] Bag M A, Valenzuela L M. Impact of the hydration states of polymers on their hemocompatibility for medical applications: A review[J/OL]. *International Journal of Molecular Sciences*. 2017, 18(8).
- [121] Fung B M, Mcgaughy T W. The state of water in muscle as studied by pulsed NMR[J/OL]. *BBA - General Subjects*. 1974, 343(3): 663-673.
- [122] Tylewicz U, Aganovic K, Vannini M, et al. Effect of pulsed electric field treatment on water distribution of freeze-dried apple tissue evaluated with DSC and TD-NMR techniques[J/OL]. *Innovative Food Science and Emerging Technologies*. 2016, 37: 352-358.
- [123] Xu C, Li Y, Yu H. Effect of far-infrared drying on the water state and glass transition temperature in carrots [J/OL]. *Journal of Food Engineering*. 2014, 136: 42-47.
- [124] Wu J, Chen S. Investigation of the hydration of nonfouling material poly(ethylene glycol) by low-field nuclear magnetic resonance[J/OL]. *Langmuir*. 2012, 28(4): 2137-2144.
- [125] Horiuchi S, Horie S, Ichimura K. Core-shell structures of silica-organic pigment nanohybrids visualized by electron spectroscopic imaging[J/OL]. *ACS Applied Materials and Interfaces*. 2009, 1(5): 977-981.
- [126] Ma X Kun, Lee N H, Oh H J, et al. Surface modification and characterization of highly dispersed silica nanoparticles by a cationic surfactant[J/OL]. *Colloids and Surfaces A: Physicochemical and Engineering Aspects*. 2010, 358(1-3): 172-176.
- [127] Anyfantakis M, Baigl D. Manipulating the coffee-ring effect: interactions at work[J/OL]. *ChemPhysChem*. 2015, 16(13): 2726-2734.
- [128] Khazieva A, Kholin K, Nizameev I, et al. Surface modification of silica nanoparticles by hexarhenium anionic cluster complexes for pH-sensing and staining of cell nuclei[J/OL]. *Journal of Colloid and Interface Science*. 2021, 594: 759-769.
- [129] Bagwe R P, Hilliard L R, Tan W. Surface modification of silica nanoparticles to reduce aggregation and nonspecific binding[J/OL]. *Langmuir*. 2006, 22(9): 4357-4362.
- [130] Da C, Chen X, Zhu J, et al. Elastic gas / water interface for highly stable foams with modified anionic silica nanoparticles and a like-charged surfactant[J/OL]. *Journal of Colloid and Interface Science*. 2021, 1401-1413, 608.
- [131] Vatanparast H, Shahabi F, Bahramian A, et al. The role of electrostatic repulsion on increasing surface activity of anionic surfactants in the presence of hydrophilic silica nanoparticles[J/OL]. *Scientific*

## References

---

- Reports, 2018, 8(1): 1-11.
- [132] Weiss L J K, Music E, Rinklin P, et al. Engineering electrostatic repulsion of metal nanoparticles for reduced adsorption in single-impact electrochemical recordings[J/OL]. ACS Applied Nano Materials, 2021, 4(8): 8314-8320.
- [133] Kumar S, Aswal V K, Kohlbrecher J. Size-dependent interaction of silica nanoparticles with different surfactants in aqueous solution[J/OL]. Langmuir, 2012, 28(25): 9288-9297.
- [134] Whitby C P, Krebsz M, Booty S J. Understanding the role of hydrogen bonding in the aggregation of fumed silica particles in triglyceride solvents[J/OL]. Journal of Colloid and Interface Science, 2018, 527: 1-9.
- [135] Trzaskus K W, Lee S L, De Vos W M, et al. Fouling behavior of silica nanoparticle-surfactant mixtures during constant flux dead-end ultrafiltration[ J/OL]. Journal of Colloid and Interface Science, 2017, 506: 308-318.
- [136] Vatanparast H, Eftekhari M, Javadi A, et al. Influence of hydrophilic silica nanoparticles on the adsorption layer properties of non-ionic surfactants at water/heptane interface[J/OL]. Journal of Colloid and Interface Science, 2019, 545: 242-250.
- [137] Weon B M, Je J H. Capillary force repels coffee-ring effect[J/OL]. Physical Review E - Statistical, Nonlinear, and Soft Matter Physics, 2010, 82(1).
- [138] Hauner I M, Deblais A, Beattie J K, et al. The dynamic surface tension of water[J/OL]. Journal of Physical Chemistry Letters, 2017, 8(7): 1599-1603.
- [139] Bzdek B R, Reid J P, Malila J, et al. The surface tension of surfactant-containing, finite volume droplets [J/OL]. Proceedings of the National Academy of Sciences of the United States of America, 2020, 117(15): 8335-8343.
- [140] ZHANG R, HUO J Hua, PENG Z Gang, et al. Research on oil-based drilling fluids emulsion droplet by low-field NMR [J/OL]. Applied Magnetic Resonance, 2016, 47(12): 1339-1352.
- [141] Jenkins S, Kirk S R, Persson M, et al. The role of hydrogen bonding in nanocolloidal amorphous silica particles in electrolyte solutions[J/OL]. Journal of Colloid and Interface Science, 2009, 339(2): 351-361.
- [142] Wang T, Gunasekaran S. State of water in chitosan-PVA hydrogel[J/OL]. Journal of Applied Polymer Science, 2006, 101(5): 3227-3232.
- [143] Cao X, Zhang M, Mujumdar A S, et al. Measurement of water mobility and distribution in vacuum microwave-dried barley grass using Low-Field-NMR[J/OL]. Drying Technology, 2018, 36(15): 1892-1899.
- [144] Kim D S, Park H B, Rhim J W, et al. Preparation and characterization of crosslinked PVA/SiO<sub>2</sub> hybrid

## References

- membranes containing sulfonic acid groups for direct methanol fuel cell applications[J/OL]. *Journal of Membrane Science*, 2004, 240(1-2): 37-48.
- [145] Pack M, Hu H, Kim D O, et al. Colloidal drop deposition on porous substrates: competition among particle motion, evaporation, and infiltration [J/OL]. *Langmuir*, 2015, 31(29): 7953-7961.
- [146] He P, Derby B. Controlling coffee ring formation during drying of inkjet printed 2d inks[J/OL]. *Advanced Materials Interfaces*, 2017, 4(22): 2-7.
- [147] Ta V D, Carter R M, Esenturk E, et al. Dynamically controlled deposition of colloidal nanoparticle suspension in evaporating drops using laser radiation[J/OL]. *Soft Matter*, 2016, 12(20): 4530-4536.
- [148] Rehl B, Gibbs J M. Role of ions on the surface-bound water structure at the silica/water interface: identifying the spectral signature of stability[J/OL]. *Journal of Physical Chemistry Letters*, 2021, 12(11): 2854-2864.
- [149] Shimobayashi S F, Tsudome M, Kurimura T. Suppression of the coffee-ring effect by sugar-assisted depinning of contact line[J/OL]. *Scientific Reports*, 2018, 8(1): 1-9.
- [150] Dilara P A, Briassoulis D. Degradation and stabilization of low-density polyethylene films used as greenhouse covering materials[J/OL]. *Journal of Agricultural and Engineering Research*, 2000, 76(4): 309-321.
- [151] Kasirajan S, Ngouajio M. Polyethylene and biodegradable mulches for agricultural applications: A review[J/OL]. *Agronomy for Sustainable Development*, 2012, 32(2): 501-529.
- [152] Al-Helal I M, Alhamdan A M. Effect of arid environment on radiative properties of greenhouse polyethylene cover[J/OL]. *Solar Energy*, 2009, 83(6): 790-798.
- [153] Potenza M, Nielsen B. Antifogging agents for polyethylene films[J/OL]. *Handbook of Industrial Polyethylene Technology*, 2016: 865-875.
- [154] Ren S, Wang L, Yu H, et al. Recent progress in synthesis of antifogging agents and their application to agricultural films: a review[J/OL]. *Journal of Coatings Technology and Research*, 2018, 15(3): 445-455.
- [155] Stevens M P. Polymer additives III. Surface property and processing modifiers[J/OL]. *Journal of Chemical Education*, 1993, 70(9): 713-718.
- [156] Shlosman K, Suckeveriene R Y, Rosen-Kligvasser J, et al. Controlled migration of antifog additives from LLDPE compatibilized with LLDPE grafted maleic anhydride[J/OL]. *Polymers for Advanced Technologies*, 2014, 25(12): 1484-1491.
- [157] Ataefard M, Moradian S, Mirabedini M, Et Al. Investigating the effect of power/time in the wettability of Ar and O<sub>2</sub> gas plasma-treated low-density polyethylene[J/OL]. *Progress in Organic Coatings*, 2009, 64(4): 482-488.

## References

- [158] Chen L, Tseng C M, Qiu Y, et al. A layer-by-layer assembled coating for improved stress corrosion cracking on biomedical magnesium alloy in cell culture medium[J/OL]. *Surface and Coatings Technology*, 2020, 403(August): 126427.
- [159] Gezgin Z, Lee T C, Huang Q. Engineering functional nanothin multilayers on food packaging: Ice-nucleating polyethylene films[J/OL]. *Journal of Agricultural and Food Chemistry*, 2013, 61(21): 5130-5138.
- [160] Moridi Z, Shekarriz S, Afshar F, et al. Obtention of polyester / cellulose fabric blend with super-hydrophobic and super-hydrophilic properties by air corona discharge treatment and their characterization[J/OL]. *Carbohydrate Polymers*, 2018, 198(February): 17-25.
- [161] Marais S, Hirata Y, Cabot C, et al. Effect of a low-pressure plasma treatment on water vapor diffusivity and permeability of poly(ethylene-co-vinyl alcohol) and polyethylene films[J/OL]. *Surface and Coatings Technology*, 2006, 201(3-4): 868-879.
- [162] Földes E, Tóth A, Kálmán E, et al. Surface changes of corona-discharge-treated polyethylene films [J/OL]. *Journal of Applied Polymer Science*, 2000, 76(10): 1529-1541.
- [163] Gupta B, Hilborn J, Hollenstein C, et al. Surface modification of polyester films by RF plasma[J/OL]. *Journal of Applied Polymer Science*, 2000, 78(5): 1083-1091.
- [164] Baba E M, Cansoy C E, Zayim E O. Investigation of wettability and optical properties of superhydrophobic polystyrene-SiO<sub>2</sub> composite surface[J/OL]. *Progress in Organic Coatings*, 2016, 99: 378-385.
- [165] Tang S, Zou P, Xiong H, et al. Effect of nano-SiO<sub>2</sub> on the performance of starch/polyvinyl alcohol blend films [J/OL]. *Carbohydrate Polymers*, 2008, 72(3): 521-526.
- [166] Harikrishnan A R, Dhar P, Agnihotri P K, et al. Wettability of complex fluids and surfactant capped nanoparticle-induced quasi-universal wetting behavior[J/OL]. *Journal of Physical Chemistry B*, 2017, 121(24): 6081-6095.
- [167] Zhang J, Jiang L, Zhao W, et al. Large-area and transparent antifogging polymeric coatings via highly efficient and facile layer-by-layer assembly[J/OL]. *Polymer Testing*, 2019, 77(February): 105907.
- [168] Gu Y, Liu H, Yang J, et al. Surface-engraved nanocomposite coatings featuring interlocked reflection-reducing, anti-fogging, and contamination-reducing performances[J/OL]. *Progress in Organic Coatings*, 2019, 127(October 2018): 366-374.
- [169] Bryaskova R, Georgieva N, Andreeva T, et al. Cell adhesive behavior of PVA-based hybrid materials with silver nanoparticles[J/OL]. *Surface and Coatings Technology*, 2013, 235: 186-191.
- [170] Chahal R P, Mahendia S, Tomar A K, et al.  $\gamma$ -Irradiated PVA/Ag nanocomposite films: Materials for

## References

- optical application s[J/OL]. *Journal of Alloys and Compounds*, 2012, 538: 212-219.
- [171] Zhu G, Zhang F, Jiang P, et al. The experimental study of polyvinyl alcohol (PVA) textile material degradation by ozone oxidation process[J/OL]. *Journal of the Textile Institute*, 2021, 112(1): 117-122.
- [172] Wang Y, Wang C, Zhang Z, et al. Effect of nanoparticles on the morphology, thermal, and electrical properties of low-density polyethylene after thermal aging[J/OL]. *Nanomaterials*, 2017, 7(10).
- [173] Wu G, Yang Y, Lei Y, et al. Hydrophilic nano-SiO<sub>2</sub>/PVA-based coating with durable antifogging properties [J/OL]. *Journal of Coatings Technology and Research*, 2020, 17(5): 1145-1155.
- [174] Wosnick J H, Mello C M, Swager T M. Synthesis and application of poly(phenylene ethynylene)s for bioconjugation: A conjugated polymer-based fluorogenic probe for proteases[J/OL]. *Journal of the American Chemical Society*, 2005, 127(10): 3400-3405.
- [175] Lee J H, Kim H G, Khang G S, et al. Characterization of wettability gradient surfaces prepared by corona discharge treatment[J/OL]. *Journal of Colloid And Interface Science*, 1992, 151(2): 563-570.
- [176] Chang S H, Tung K W, Liao B S, et al. Surface and protein adsorption properties of 316L stainless steel modified by polyvinyl alcohol and plasma-treated polyvinyl alcohol films[J/OL]. *Surface and Coatings Technology*, 2019, 362(August 2018): 208-212.
- [177] Liao W, Huang X, Ye L, et al. Synthesis of composite latexes of polyhedral oligomeric silsesquioxane and fluorine containing poly(styrene-acrylate) by emulsion copolymerization[J/OL]. *Journal of Applied Polymer Science*, 2016, 133(21): 6-11.
- [178] Ma H, Shi T, Song Q. Synthesis and characterization of novel PVA/SiO<sub>2</sub>-TiO<sub>2</sub> hybrid fibers [J/OL]. *Fibers*, 2014, 2(4): 275-284.
- [179] Li J, Suo J, Deng R. Structure, mechanical, and swelling behaviors of poly(vinyl alcohol)/SiO<sub>2</sub> hybrid membranes[J/OL]. *Journal of Reinforced Plastics and Composites*, 2010, 29(4): 618-629.
- [180] Soroush A, Ma W, Silvino Y, et al. Surface modification of thin film composite forward osmosis membrane by silver-decorated graphene-oxide nanosheets[J/OL]. *Environmental Science: Nano*, 2015, 2(4): 395-405.
- [181] Toledo P V O, Bernardinelli O D, Sabadini E, et al. The states of water in tryptophan grafted hydroxypropyl methylcellulose hydrogels and their effect on the adsorption of methylene blue and rhodamine B[J/OL]. *Carbohydrate Polymers*, 2020, 248, 116765.
- [182] Li X, Ma L, Tao Y, et al. Low field-NMR in measuring water mobility and distribution in beef granules during drying process[J/OL]. *Advanced Materials Research*, 2012, 550-553: 3406-3410.
- [183] Durán I R, Laroche G. Water drop-surface interactions as the basis for the design of anti-fogging surfaces: Theory, practice, and applications trends[J/OL]. *Advances in Colloid and Interface Science*,

## References

---

- 2019, 263: 68-94.
- [184] Wang Y, Yao L, Ren T, et al. Robust yet self-healing antifogging/antibacterial dual-functional composite films by a simple one-pot strategy[J/OL]. *Journal of Colloid and Interface Science*, 2019, 540: 107-114.
- [185] Han Z, Feng X, Guo Z, et al. Flourishing bioinspired antifogging materials with superwettability: progresses and challenges[J/OL]. *Advanced Materials*, 2018, 30(13): 1-32.
- [186] Zhang X, He J. Antifogging antireflective thin films: Does the antifogging layer have to be the outmost layer?[J/OL]. *Chemical Communications*, 2015, 51(63): 12661-12664.
- [187] Zhao J, Ma L, Millians W, et al. Dual-functional antifogging/antimicrobial polymer coating[J/OL]. *ACS Applied Materials and Interfaces*, 2016, 8(13): 8737-8742.
- [188] Manning T G, Perera M, Christidis D, et al. Visual occlusion during minimally invasive surgery: A contemporary review of methods to reduce laparoscopic and robotic lens fogging and other sources of optical loss[J/OL]. *Journal of Endourology*, 2017, 31(4): 327-333.
- [189] Elkholy A A, Grant R, Assiri A, et al. MERS-CoV infection among healthcare workers and risk factors for death: Retrospective analysis of all laboratory-confirmed cases reported to WHO from 2012 to 2 June 2018 [J/OL]. *Journal of Infection and Public Health*, 2020, 13(3): 418-422.
- [190] Zargar V, Asghari M, Dashti A. A Review on chitin and chitosan polymers: structure, chemistry, solubility, derivatives, and applications[J/OL]. *ChemBioEng Reviews*, 2015, 2(3): 204-226.
- [191] Kishore Kumar Gadghey G S S. Investigation of mechanical properties of chitosan based films: a review [J]. *International Journal of Advanced Research in Engineering and Technology*, 2017, 8(6): 93-102.
- [192] Zhang W, Zhang J, Jiang Q, et al. The hypolipidemic activity of chitosan nanopowder prepared by ultrafine milling [J/OL]. *Carbohydrate Polymers*, 2013, 95(1): 487-491.
- [193] Minet E P, O'carroll C, Rooney D, et al. Slow delivery of a nitrification inhibitor (dicyandiamide) to soil using a biodegradable hydrogel of chitosan[J/OL]. *Chemosphere*, 2013, 93(11): 2854-2858.
- [194] Quiñones J P, Gothelf K V, Kjems J, et al. N,O6-partially acetylated chitosan nanoparticles hydrophobically-modified for controlled release of steroids and vitamins[J/OL]. *Carbohydrate Polymers*, 2013, 91(1): 143-151.
- [195] Ghorbani F M, Kaffashi B, Shokrollahi P, et al. PCL/chitosan/Zn-doped nHA electrospun nanocomposite scaffold promotes adipose derived stem cells adhesion and proliferation[J/OL]. *Carbohydrate Polymers*, 2015, 118: 133-142.
- [196] Vicente T, Mota J P B, Peixoto C, et al. Rational design and optimization of downstream processes of virus particles for biopharmaceutical applications: Current advances[J/OL]. *Biotechnology Advances*, 2011, 29(6): 869-878.



## References

---

- [197] Nagahama H, Nwe N, Jayakumar R, et al. Novel biodegradable chitin membranes for tissue engineering applications[J/OL]. *Carbohydrate Polymers*, 2008, 73(2): 295-302.
- [198] Jayakumar R, Rajkumar M, Freitas H, et al. Preparation, characterization, bioactive and metal uptake studies of alginate/phosphorylated chitin blend films[J/OL]. *International Journal of Biological Macromolecules*, 2009, 44(1): 107-111.
- [199] Jayakumar R, Chennazhi K P, Muzzarelli R A A, et al. Chitosan conjugated DNA nanoparticles in gene therapy[J/OL]. *Carbohydrate Polymers*, 2010, 79(1): 1-8.
- [200] Prabakaran M, Mano J F. Chitosan-based particles as controlled drug delivery systems[J/OL]. *Drug Delivery: Journal of Delivery and Targeting of Therapeutic Agents*, 2005, 12(1): 41-57.
- [201] Higazy A, Hashem M, Elshafei A, et al. Development of antimicrobial jute packaging using chitosan and chitosan-metal complex[J/OL]. *Carbohydrate Polymers*, 2010, 79(4): 867-874.
- [202] Epure V, Griffon M, Pollet E, et al. Structure and properties of glycerol-plasticized chitosan obtained by mechanical kneading[J/OL]. *Carbohydrate Polymers*, 2011, 83(2): 947-952.
- [203] Shojaee Kang Sofla M, Mortazavi S, Seyfi J. Preparation and characterization of polyvinyl alcohol/chitosan blends plasticized and compatibilized by glycerol/polyethylene glycol[J/OL]. *Carbohydrate Polymers*, 2020, 232.
- [204] Suyatma N E, Tighzert L, Copinet A, et al. Effects of hydrophilic plasticizers on mechanical, thermal, and surface properties of chitosan films[J/OL]. *Journal of Agricultural and Food Chemistry*, 2005, 53(10): 3950-3957.
- [205] Cano L, Pollet E, Avérous L, et al. Effect of TiO<sub>2</sub> nanoparticles on the properties of thermoplastic chitosan-based nano-biocomposites obtained by mechanical kneading[J/OL]. *Composites Part A: Applied Science and Manufacturing*, 2017, 93: 33-40.
- [206] Alshehri A H, Jakubowska M, Młoziniak A, et al. Enhanced electrical conductivity of silver nanoparticles for high frequency electronic applications[J/OL]. *ACS Applied Materials and Interfaces*, 2012, 4(12): 7007-7010.
- [207] Pugazhendhi S, Kirubha E, Palanisamy P K, et al. Synthesis and characterization of silver nanoparticles from *Alpinia calcarata* by Green approach and its applications in bactericidal and nonlinear optics [J/OL]. *Applied Surface Science*, 2015, 357: 1801-1808.
- [208] Chen X, Zhao X, Wang G. Review on marine carbohydrate-based gold nanoparticles represented by alginate and chitosan for biomedical application[J/OL]. *Carbohydrate Polymers*, 2020, 244: 116311.
- [209] Kwon D J, Shin P S, Kim J H, et al. Interfacial properties and thermal aging of glass fiber/epoxy composites reinforced with SiC and SiO<sub>2</sub> nanoparticles[J/OL]. *Composites Part B: Engineering*, 2017,

## References

---

130: 46-53.

- [210] Wang Q, Hou R, Cheng Y, et al. Super-tough double-network hydrogels reinforced by covalently compositing with silica-nanoparticles[J/OL]. *Soft Matter*, 2012, 8(22): 6048-6056.
- [211] Yeh S B, Chen C S, Chen W Y, et al. Modification of silicone elastomer with zwitterionic silane for durable antifouling properties[J/OL]. *Langmuir*, 2014, 30(38): 11386-11393.
- [212] Venault A, Yang H S, Chiang Y C, et al. Bacterial resistance control on mineral surfaces of hydroxyapatite and human teeth via surface charge-driven antifouling coatings [J/OL]. *ACS Applied Materials and Interfaces*, 2014, 6(5): 3201-3210.
- [213] Jiang S, Cao Z. Ultralow-fouling, functionalizable, and hydrolyzable zwitterionic materials and their derivatives for biological applications[J/OL]. *Advanced Materials*, 2010, 22(9): 920-932.
- [214] Guo H, Xu T, Zhang J, et al. A multifunctional anti-fog, antibacterial, and self-cleaning surface coating based on poly(NVP-co-MA)[J/OL]. *Chemical Engineering Journal*, 2018, 351, 409-417.
- [215] Liu H, Adhikari R, Guo Q, et al. Preparation and characterization of glycerol plasticized (high-amylose) starch-chitosan films[J/OL]. *Journal of Food Engineering*, 2013, 116(2): 588-597.
- [216] Haghghi H, Leugoue S K, Pfeifer F, et al. Development of antimicrobial films based on chitosan-polyvinyl alcohol blend enriched with ethyl lauroyl arginate (LAE) for food packaging applications[J/OL]. *Food Hydrocolloids*, 2020, 100, 105419.
- [217] Tian R, Seitz O, Li M, et al. Infrared characterization of interfacial Si-O bond formation on silanized flat SiO<sub>2</sub>/Si Surfaces[J/OL]. *Langmuir*, 2010, 26(7): 4563-4566.
- [218] Zhu L J, Wang J J, Guo L, et al. Study on the preparation and properties of the PVA/SiO<sub>2</sub> hybrid coating on BOPP film via sol-gel process[J/OL]. *Advanced Materials Research*, 2011, 239-242: 1956-1959.
- [219] Wonnie Ma I A, Ammar S, Bashir S, et al. Preparation of hybrid chitosan/silica composites via ionotropic gelation and its electrochemical impedance studies[J/OL]. *Progress in Organic Coatings*, 2020, 145(April): 105679.
- [220] Introzzi L, Fuentes-Alventosa J M, Cozzolino C A, et al. 'Wetting enhancer' pullulan coating for antifog packaging applications[J/OL]. *ACS Applied Materials and Interfaces*, 2012, 4(7): 3692-3700.
- [221] Liu Y, Dai C, Wang K, et al. Study on a novel cross-linked polymer gel strengthened with silica nanoparticles[J/OL]. *Energy and Fuels*, 2017, 31(9): 9152-9161.
- [222] Tomar B S, Shahin A, Tirumkudulu M S. Cracking in drying films of polymer solutions[J/OL]. *Soft Matter*, 2020, 16(14): 3476-3484.
- [223] Xavier J R. Improvement of mechanical and anticorrosion coating properties in conducting polymer poly(propyl methacrylate) embedded with silane functionalized silica nanoparticles[J/OL]. *Silicon*, 2021,

## References

---

13(10): 3291-3305.

- [224] Vivar Mora L, Taylor A, Paul S, et al. Impact of silica nanoparticles on the morphology and mechanical properties of sol-gel derived coatings[J/OL]. *Surface and Coatings Technology*, 2018, 342, 48-56.
- [225] Silletta E V., Velasco M I, Gomez C G, et al. Enhanced surface interaction of water confined in hierarchical porous polymers induced by hydrogen bonding [J/OL]. *Langmuir*, 2016, 32(29): 7427-7434.
- [226] Mehra N, Mu L, Ji T, et al. Moisture driven thermal conduction in polymer and polymer blends[J/OL]. *Composites Science and Technology*, 2017, 151: 115-123.